The Effects of Orientation Angle, Subcooling, Heat Flux, Mass Flux, and Pressure on Bubble Growth and Detachment in Subcooled Flow Boiling

Rosemary M. Sugrue

SUBMITTED TO THE DEPARTMENT OF NUCLEAR SCIENCE AND ENGINEERING
IN PARTIAL FULFILLMENT OF THE REQUIREMENTS FOR THE DEGREES OF

MASTER OF SCIENCE IN NUCLEAR SCIENCE AND ENGINEERING
AND
BACHELOR OF SCIENCE IN NUCLEAR SCIENCE AND ENGINEERING
AT THE
MASSACHUSETTS INSTITUTE OF TECHNOLOGY

JUNE 2012

Signature of Author: _____
Rosemary Sugrue

Certified by: _____
Jacopo Buongiorno, Ph.D.
Associate Professor of Nuclear Science and Engineering
Thesis Supervisor

Certified by: _____
Thomas McKrell, Ph.D.
Research Scientist, Nuclear Science and Engineering
Thesis Co-Supervisor

Accepted by: _____
Mujid Kazimi, Ph.D.
TEPCO Professor of Nuclear Science and Engineering
Chair, Department Committee on Graduate Students

The Effects of Orientation Angle, Subcooling, Heat Flux, Mass Flux, and Pressure on Bubble Growth and Detachment in Subcooled Flow Boiling

Rosemary Sugrue

Submitted to the Department of Nuclear Science and Engineering on May 11, 2012 in partial fulfillment of the requirements for the degrees of Bachelor of Science and Master of Science in Nuclear Science and Engineering

ABSTRACT

The effects of orientation angle, subcooling, heat flux, mass flux, and pressure on bubble growth and detachment in subcooled flow boiling were studied using a high-speed video camera in conjunction with a two-phase flow loop that can accommodate a wide range of flow conditions. Specifically, orientation angles of 0° (downward-facing horizontal), 30°, 45°, 60°, and 90° (vertical); mass flux values of 250, 300, 350, and 400 kg/m^{2}s, with corresponding Froude numbers in the range of 0.42 to 1.06; pressures of 101 (atmospheric), 202, and 505 kPa; two values of subcooling (10°C to 20°C); and two heat fluxes (0.05 to 0.10 MW/m^2) were explored. The combination of the test section design, high-speed video camera, and LED lighting results in high accuracy (order of 20 microns) in the determination of bubble departure diameter. The data indicate that bubble departure diameter increases with increasing heat flux, decreasing mass flux, decreasing levels of subcooling, and decreasing pressure. Also, bubble departure diameter increases with decreasing orientation angle, i.e. the largest bubbles are found to detach from a downward-facing horizontal surface. The mechanistic bubble departure model of Klausner et al. and its recent modification by Yun et al. were found to correctly predict all the observed parametric trends, but with large average errors and standard deviation: 35.7±24.3% for Klausner's and 16.6±11.6% for Yun's. Since the cube of the bubble departure diameter is used in subcooled flow boiling heat transfer models, such large errors are clearly unacceptable, and underscore the need for more accurate bubble departure diameter models to be used in CFD.

Thesis Supervisor: Jacopo Buongiorno
Title: Associate Professor of Nuclear Science and Engineering

Thesis Co-Supervisor: Thomas McKrell
Title: Research Scientist, Nuclear Science and Engineering

ACKNOWLEDGEMENTS

There are numerous individuals who have guided, developed, inspired, and supported me during the past five years of my undergraduate and graduate experience at MIT. I was truly blessed to interact with some of the world's most exemplary scholars in the field of Nuclear Science and Engineering.

First and foremost, I am extraordinarily grateful to Professor Jacopo Buongiorno who was my advisor throughout my time in Course 22 and who gave me the opportunity to discover the world of experimental research through MIT's UROP program three years ago. His dedication to excellence in all that he does - as a brilliant researcher and educator - inspires me every day and led to my decision to pursue a doctoral degree in the field of thermal hydraulics. The work described in this thesis would not have been possible without his thoughtful feedback, suggestions, and willingness to spend countless hours guiding my efforts.

My sincere appreciation also goes to Dr. Thomas McKrell for always being there to help whenever I encountered the inevitable hurdles and challenges associated with experimental research. I would not have been able to complete my experiments without his guidance and support.

Special thanks to Dr. Greg DeWitt for introducing me to the excitement and rewarding nature of laboratory research as well as the need for resilience in an environment where Murphy's Law continually holds true. I am also so appreciative to Greg for passing on his experimental loop which I used in the studies described in this work.

There are a number of other colleagues from the Green Lab and our Nanogroup team whose assistance was invaluable. In particular, I wish to thank Eric Forrest for going above and beyond by teaching me how to use the High-Speed Video Camera, finding LED lights for our experiments, helping me model bubble departure dynamics, and most importantly, for always being there when I needed an extra set of hands running experiments. A special thanks also goes to Bren Phillips for his assistance with the High-Speed Video Camera and for his expertise with Matlab modeling. I would not have been able to complete the numerous experimental runs and data analyses without the help of these incredible individuals.

My coursework in the master's program and this thesis would not have been possible without the financial support from a number of sources. My heartfelt thanks goes to: the National Academy for Nuclear Training for the fellowship which funded my graduate year; to CASL for supporting our work in the Green Lab; to Mr. Doug Spreng who donated the resources needed for the experimental loop constructed by Dr. Greg DeWitt; and to Lowel Lighting LLC for donating the LED lights which were essential in taking the high resolution images needed for this thesis.

My research and coursework throughout the past five years went smoothly due to the efforts of our wonderful NSE staff members. I am extremely grateful to: Clare Egan, Heather Barry, Peter Brenton, Dorian Cohen, and Rachel Morton, among others. Clare Egan, especially, always had the right answer for any question or problem I encountered. Peter Brenton was also a remarkable source of support, especially this past year in working with and assisting those of us who served on the ANS Executive Board.

There are several colleagues within the department who have really helped to make the past five

years and in particular, my fifth year, some of the best times of my life. I am especially thankful to Brittany Guyer, for being an amazing friend, role model, and office neighbor. She has been there for me whenever I needed a reprieve from a particularly stressful day and for continual advice. She has made my long days in the office so much more enjoyable and I would not have survived without her.

I am also so thankful to Sara Ferry who has been at my side for the roller coaster ride that characterized our last five years at MIT. She can always be counted on to find humor in even the most stressful of times, and I am so happy that we will both be spending the next few years together in the doctoral program.

Special thanks and gratitude goes to my officemate, Bryan Herman, who selflessly made himself available to not only me, but to countless other students in the department whenever help was needed. He has tremendous patience when it comes to teaching and helping others, and his modeling expertise was invaluable throughout the past year. Thanks also to Mark Reed, my other office neighbor, for his encouragement and friendship over the last several months and for being such a great teaching assistant in 22.101.

I also thank my fellow ANS Executive Board members - Brittany Guyer, Koroush Shirvan, Lindsey Gilman, Bren Phillips, and Jake DeWitt - for bringing balance to what would have otherwise been a life of 24 hour work days. I loved spending time with all of them, and our executive meetings gave me something to look forward to throughout this year.

Finally, there really are no words to express how unbelievably grateful I am for the consistent love and support of my parents. I feel so privileged every day to have parents who can simultaneously serve as my closest friends and my most inspirational role models. I absolutely would not be where I am today without them.

Contents

List of Figures

List of Tables

NOMENCLATURE

Symbol	Definition	Units
A_f	flow area	$[m^2]$
c_p	specific heat	$[J/kg - K]$
C_s	constant in growth force	$[dimensionless]$
d_b	bubble departure diameter	$[m]$
d_w	bubble contact diameter	$[m]$
D	inner width of flow channel	$[m]$
f	friction factor	$[dimensionless]$
F_b	buoyancy force	$[N]$
F_{cp}	contact pressure force	$[N]$
F_{du}	growth force	$[N]$
F_h	hydrodynamic pressure force	$[N]$
F_{qs}	quasi-steady drag force	$[N]$
F_s	surface tension force	$[N]$
F_{sL}	shear lift force	$[N]$
G	mass flux	$[kg/m^2s]$
G_s	liquid shear gradient	$[dimensionless]$
h_{fg}	latent heat of evaporation	$[J/kg]$
Ja	Jakob number	$[dimensionless]$
k	thermal conductivity	$[W/m\text{-}K]$
R	bubble radius	$[m]$
Re	Reynolds number	$[dimensionless]$
t	time	$[s]$
T	temperature	[°C]
ΔT_{sat}	wall superheat	[°C]
ΔT_{sub}	bulk subcooling	[°C]
u	time averaged velocity used in Reichardt's turbulent relation	$[m/s]$
v	velocity	$[m/s]$
V_b	bubble volume	$[m^3]$
X	vapor quality	$[dimensionless]$
y	distance from wall used in Reichardt's turbulent relation	$[m]$
	Greek Letters	
α	advancing contact angle	[°]
β	receding contact angle	[°]
δ	liquid film thickness	$[m]$
η	thermal diffusivity	$[m^2/s]$
μ	dynamic viscosity	$[N * s/m^2]$
ν	kinematic viscosity	$[m^2/s]$
ρ	density	$[kg/m^3]$
σ	surface tension	$[N/m]$
τ	wall shear stress	$[Pa]$
ϑ	orientation angle	[°]
ϕ	angle of bubble growth	$[radians]$

Symbol	Definition
	Subscripts
l	liquid
v	vapor
x	x-direction
y	y-direction
	Acronyms
CFD	computational fluid dynamics
CHF	critical heat flux
DC	direct current
DI	de-ionized
DNB	departure from nucleate boiling
FDB	fully-developed boiling
FM	flow meter
HSV	high-speed video
LWR	light water reactor
ONB	onset of nucleate boiling
OSB	onset of saturated boiling
PT	pressure transducer
PWR	pressurized water reactor
RTD	resistance temperature detector

1 Introduction and Background

Understanding and predicting the complex processes involved in boiling heat transfer is necessary for the efficient operation, safety, and development of nuclear reactors. Subcooled flow boiling, an occurrence in the fuel channel of a PWR, plays an essential role in fostering high heat transfer efficiencies as well as in cooling the reactor core [1]. Thus, assessing the efficiency of mechanistic models dealing with subcooled flow dynamics is increasingly important in order to create and validate simulations of multi-dimensional flow boiling such as those used in computational fluid dynamics (CFD) codes.

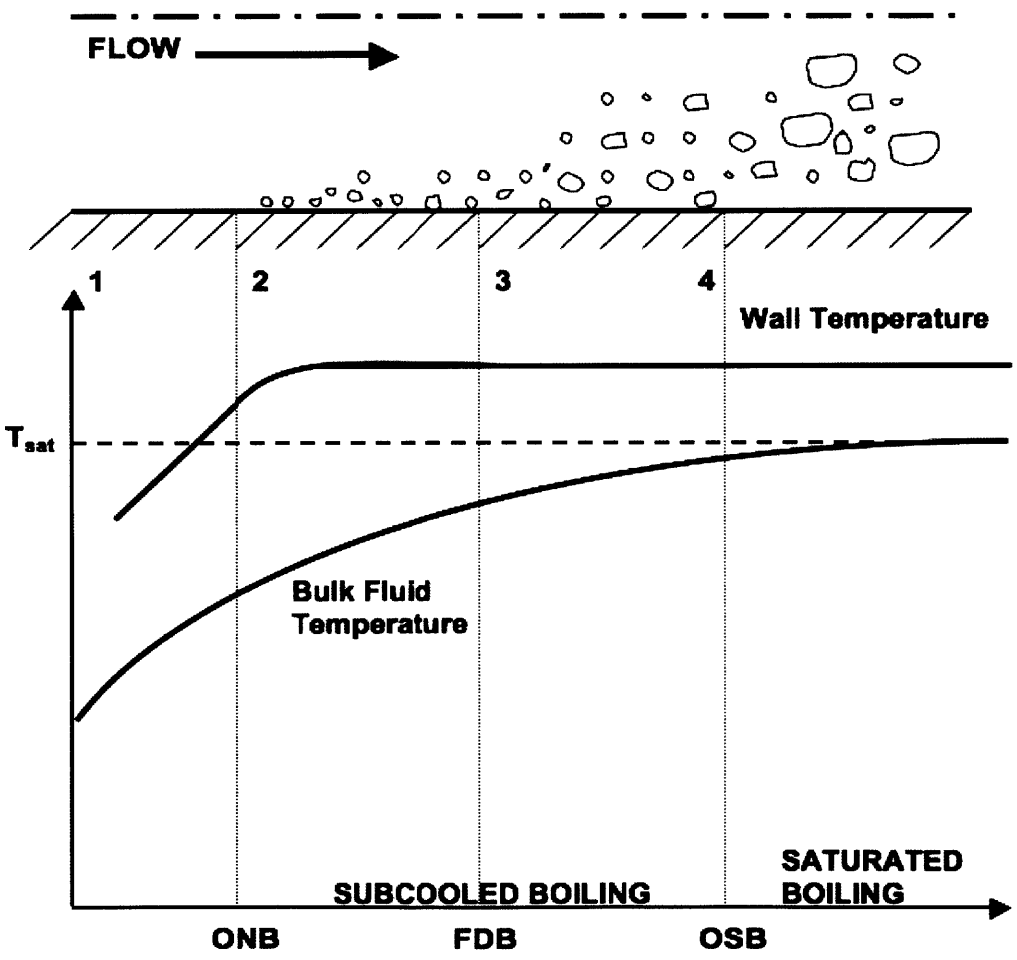

Figure 1: Depiction of the regions and temperature distributions in flow boiling.

Subcooled boiling begins with the onset of nucleate boiling, ONB, when the temperature of the fluid

near the wall is above saturation. This is shown in Figure 1 at point 2. Since the fluid temperature near the wall of the heated surface is above the saturation point, vapor bubbles initially begin to nucleate on the wall while most of the liquid remains subcooled. At this stage, bubbles nucleate and grow on the heated surface but do not detach because of the bulk fluid's low temperature, which causes condensation of the bubbles. With increasing temperature, the initiation of bubble growth and detachment occurs. This region, between points 2 and 3, is referred to as the fully developed boiling (FDB), or low subcooled, region [2, 3]. Bubbles continue to increase in size and detach more frequently until bulk saturation is reached, which represents the onset of saturated boiling, OSB [1]. Figure 1 shows these regions as well as the temperature distributions for the various boiling phases. Subcooled boiling, the region between ONB and OSB, points 2 and 4 in Figure 1, consists of a number of dynamic processes which include heat and mass transfer, nucleation, and departure of bubbles.

Although there are a plethora of studies published on the boiling phenomenon in general as well as subcooled boiling, bubble nucleation and departure dynamics are still not clearly understood [4]. A number of mechanistic models have, however, been developed for bubble nucleation, growth, and departure [5]. Direct visualization of bubble parameters is an effective means to validate models with high quality resolution experimental data to incorporate into 3-D CFD multi-fluid predictive simulations [6].

The state-of-the-art simulation approach for nuclear systems with two-phase flow and heat transfer relies on CFD simulations implementing the Eulerian-Eulerian, two-fluid, six-equation model [8], [9], [10], with or without an interfacial area transport model [7]. These approaches require closure relations for the phase-to-phase and wall-to-flow mass, momentum and energy terms in the governing equations. Subcooled boiling heat transfer is captured by the wall-to-flow constitutive relation for energy. Examples of boiling heat transfer constitutive relations are the heat flux partitioning model of Kurul and Podowski [11], Kolev's bubble interaction model [12], and the more recent hybrid numerical-empirical model of Sanna et al. [13]. They all require accurate knowledge of the bubble departure diameter. For example, in the partitioning heat flux model the heat removed by the boiling fluid is assumed to be through three contributions, (i) the latent heat of evaporation to

form the bubbles ($q_e^{"}$), (ii) heat expended in re-formation of the thermal boundary layer following bubble departure, or the so-called quenching heat flux ($q_q^{"}$), and (iii) heat transferred to the liquid phase outside the zone of influence of the bubbles by convection ($q_c^{"}$). Then the total boiling heat flux is obtained through the addition of the three fluxes as:

$$q_{tot}^{"} = q_e^{"} + q_q^{"} + q_c^{"} \tag{1.1}$$

The latent heat flux is often the dominant term in this equation, and can be written as:

$$q_e^{"} = \frac{\pi}{6} D_b^3 \rho_v h_{fg} f_b n^{"} \tag{1.2}$$

where D_b is the bubble departure diameter, f_b is the frequency of bubble departure, and n" is the nucleation site density. The cubic dependence in this equation suggests that small uncertainties on the bubble departure diameter are greatly magnified in the heat transfer model, thus deteriorating the accuracy of the overall CFD simulation. Therefore, it is imperative to develop robust and accurate bubble departure models for flow boiling conditions.

To generate the visualization data needed for CFD models and for the validation of mechanistic formulations, high-speed digital photography, among other methods, has been utilized to study bubble characteristics in a variety of flow boiling contexts. Thorncroft et al. [14] experimentally investigated vapor bubble growth and detachment processes for vertical upflow as well as downflow boiling under slightly subcooled conditions utilizing high-speed digital imagery to assess bubble size; growth rate; bubble departure and lift-off diameter; and waiting time from isolated nucleation sites. The studies were conducted for FC-87 refrigerant over a nichrome heating surface with mass flux ranging from 190 to 666 kg/m^{2}s and heat flux from 1.3 to 14.6 kW/m^2. Results indicated that the bubble characteristics associated with upflow and downflow boiling are significantly different, with upflow bubble dynamics more conducive for augmenting energy transfer than the downflow configuration. Thorncroft et al. conjectured that the process of bubble sliding was responsible for the enhanced energy transfer in view of the larger heat transfer coefficients for upflow compared with downflow under the same operating conditions. This was consistent with Bibeau who found,

using high-speed imaging, that the bubble continued growing as it slid along the heating surface until reaching a maximum size where the condensation rate exceeded evaporation [15].

Several other investigations have also used digital imaging with the intent of developing or improving correlations for more accurate mechanistic models in subcooled boiling contexts [6]. Situ et al. conducted a series of studies in forced convective subcooled flow boiling under vertical upflow in an annulus with water as the working fluid, using a high-speed digital camera to assess bubble lift-off diameters, growth rate, and velocity after lift off. Data was taken at atmospheric pressure with mass flux values between 466 to 900 kg/m^{2}s and heat flux in the range of 54 to 206 kW/m^2. Visualization results indicated that bubble departure frequency was directly correlated with nucleate boiling heat flux [16]. Basu et al., in a series of investigations using an upward-vertical subcooled flow facility, assessed waiting time, bubble growth time, and bubble departure size with water as the working fluid on two different surfaces. Heat flux and wall superheat required for boiling inception were found to be dependent on flow rate, liquid subcooling, and contact angle [17].

Subsequently, Situ and colleagues [4] determined bubble departure characteristics, such as bubble departure frequency, lift-off diameter, and growth rate, for 58 test conditions in a vertical upward annular channel with water as the working fluid, and compared their results with those obtained by Thorncroft et al. as well as Basu et al. Tests were run at atmospheric pressure with inlet temperature ranging from 80.0° to 98.0°C and heat flux from 60.7 to 206 kW/m^2 utilizing a high speed digital camera to capture bubble nucleation. Their findings, illustrating that in the partial boiling region bubble departure frequency was related to nucleate boiling transfer, led to a proposed correlation for bubble lift-off diameter as a function of Jakob number and Prandtl number, which reproduces data well at low wall superheat. Euh et al. investigated bubble nucleation in vertical upward forced-convective subcooled boiling flow using water under varying pressures from 167 to 346 kPa, mass fluxes ranging from 214 to 1869 kg/m^{2}s, and heat fluxes from 61 to 238 kW/m^2. Results indicated that bubble departure frequency increased with heat flux and pressure but decreased with mass flux and degree of subcooling [18]. This was consistent with Situ et al. findings (modifying the Situ et al. empirical equation for higher atmospheric pressures), but was not congruent with the Basu et al. data collected under lower mass flux and higher heat flux conditions.

A number of other experimental regimes and simulations have varied stimulant fluids, pressure, subcooled temperature levels, channel characteristics, pressures, and flow rates to develop and validate models predicting bubble parameters particularly with respect to bubble size and detachment [19, 20, 21, 22, 23]. The most commonly-used mechanistic bubble departure model for flow boiling is that of Klausner et al. [5], which is based on a balance of static and dynamic forces for the bubble throughout its growth cycle. Klausner postulates that at the time of departure the balance is broken and the bubble can either lift off (non-zero force perpendicular to the wall) or slide along the wall (non-zero force tangential to the wall). Thus, their mechanistic model is based on the premise that surface tension and symmetrical bubble growth act in a direction opposite to the fluid motion which is key in keeping bubbles at the nucleation site prior to departure. This model was originally calibrated to predict bubble departure size in refrigerant R113 flow. Subsequently, Zeng et al. modified and expanded the applicability of the Klausner et al. model for both horizontal and vertical channels under pool and flow boiling conditions with refrigerant R113, with pressure ranging from 20 to 280 kPa; Jakob number between 4 and 869; and gravity, 1 to 0.014 g [24].

Other modifications have been proposed to explain a wider range of fluid mediums, flow directions, pressure conditions, temperature, etc. Situ et al. [16] and Yeoh et al. [19] extended the model to flow conditions with water, and Yun et al. improved the model's predictive capability by incorporating a bubble condensation model as well as evaluating the model for a wider range of pressure, temperature, and flow rates [20, 21]. The specifics of these mechanistic models will be discussed in Section 3, and their test matrices are presented in Table 1 below.

Table 1: Test matrices of previous research done with respect to bubble departure.

Parameter	**Klausner [5]**	**Situ [16]**	**Yeoh [19]**	**Yun [20]**
Orientation:	horizontal	vertical	vertical	vertical
Pressure:	101 kPa	101 kPa	139.4 kPa	1455 - 2990 kPa
Mass Flux:	112 - 287 kg/m^{2}s	487 - 939 kg/m^{2}s	474, 1059.2 kg/m^{2}s	1000 - 3000 kg/m^{2}s
Heat Flux:	11 - 26 kW/m^2	60.7 - 206 kW/m^2	152.3, 251.5 kW/m^2	58 - 109 kW/m^2
Working Fluid:	R113	water	water	R12
Subcooling:	n/a	2 - 20°C	13.4, 17.9°C	n/a

2 Objectives and Hypotheses

Although the studies referenced above have shed some light on bubble parameters in subcooled flow boiling under various conditions, none have assessed the impact that the orientation angle of the channel may have on bubble departure diameter. In high mass flux contexts, which are typical of full-power reactor operation, orientation should not be a factor and its effect would, in fact, be predicted from Froude number order-of-magnitude estimates [26]. However, when the mass flux is lower, buoyancy forces and channel orientation are expected to be important. This is the case in applications such as current reactors under off-normal operations (e.g., natural circulation following loss of flow, or decay heat removal from the vessel surface during severe accidents, the so-called in-vessel retention), in small modular reactors using natural circulation under normal operation, and in electronic cooling applications [27].

Thus, the primary objective of this study is to investigate the effects of mass flux, heat flux, degree of subcooling, pressure, and angle of orientation of the heater surface on the departure diameter of steam bubbles in subcooled flow boiling. Specifically, bubble departure diameter will be visually observed and measured using a high-speed video camera under conditions of upward and downward facing vertical (90°), 30°, 45°, 60° upflow, as well as horizontal (0°) flow. Each of these orientations will be studied under conditions of varying mass flux (250, 300, 350, 400 kg/m^{2}s), heat flux (0.05 and 0.1 MW/m^2), subcooling (10 and 20°C), and pressure (101, 202, and 505 kPa). The values of mass flux were chosen to be sufficiently low in order to ensure a significant effect of the orientation angle, as suggested by Klausner's model. The heat flux range was chosen to ensure that subcooled flow boiling occurs in the so-called 'isolated bubbles' regime, where interactions between bubbles at adjacent nucleation sites can be neglected. The ranges for the other parameters were chosen to produce measurable changes of the bubble departure diameter, within the operating envelope possible in the flow loop, described below.

It is anticipated that bubble departure diameter will increase as the test section becomes more inclined with respect to the vertical (90°) position for a downward-facing setup. Diameters are predicted to be smallest for a vertical test section, and largest for a downward-facing horizontal (0°)

setup. Further, bubble departure diameter should increase with decreasing mass flux, increasing heat flux, decreasing levels of subcooling, and decreasing pressure. Empirical data will be compared with existing bubble departure models to assess their validity and potential refinement to enhance the data set needed for CFD code validation.

In addition, the data collected for this investigation will utilize a custom designed flow loop that allows for the measurement of multiple bubble, heater, and flow parameters in subcooled flow boiling context with a high-speed, high-resolution video camera. While many of the experimental studies noted above used high-speed video or photographic visualization techniques to measure bubble diameter, most were conducted in a vertical or horizontal annulus with an interior heating mechanism. Few of these designs have utilized the high spatial resolution of advanced cameras, which is needed to validate predictive models for CFD applications.

Unlike the aforementioned designs, this experiment will assess bubble parameters for a full range of orientation angles, including downward-facing (0°) horizontal, 30°, 45°, 60°, and vertical (90°). Further, the Phantom high-speed camera and Lowel LED lights will allow for high enough resolution to determine bubble departure diameters with minimal experimental uncertainty.

3 Bubble Departure Models

As previously noted, Klausner et al. in 1993 proposed a popular model used to predict bubble size and departure dynamics which is based on a mechanistic force balance equation for a bubble at its departure from a single nucleation site [5]. This method was first applied to flow boiling in both vertical and horizontal conditions using refrigerant R113 and was later modified for a wider range of flow conditions by Zeng et al. [24], Situ [16], Yeoh et al. [19], and Yun et al. [21].

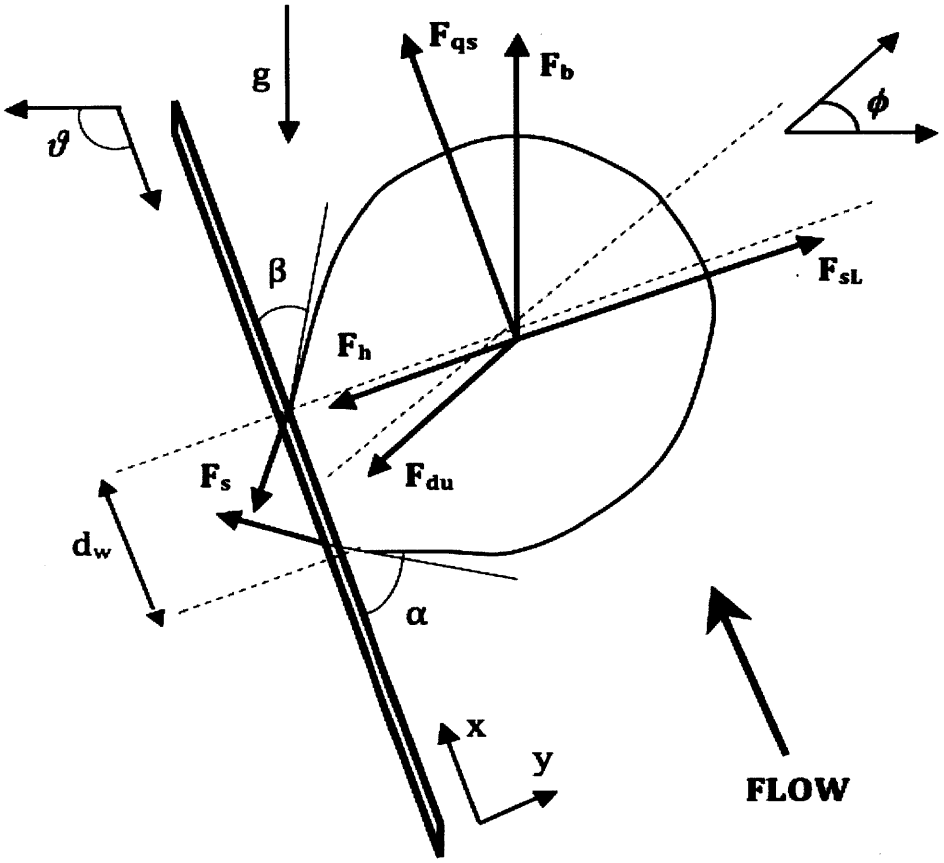

Figure 2: Schematic diagram of the forces acting on a bubble for bubble departure in subcooled flow boiling.

Essentially, the basis of the model is a sum of forces in the x-direction, parallel to the flow, and

y-direction, perpendicular to the flow and heater surface. Specifically:

$$\sum F_x = F_{sx} + F_{qs} - F_b sin\vartheta + F_{du} sin\phi \tag{3.1}$$

$$\sum F_y = F_{sy} + F_{sL} - F_b cos\vartheta + F_h + F_{cp} + F_{du} cos\phi \tag{3.2}$$

where F_s is the surface tension force, F_{qs} is the quasi-steady drag force, F_b is the buoyancy force, F_{du} is the unsteady drag force due to asymmetric growth, F_{sL} is the shear lift force, F_h is the hydrodynamic pressure force, F_{cp} is the contact pressure force, ϑ is the orientation angle of the heater surface (flow direction), and ϕ is the angle representing the direction of bubble growth with respect to the y-axis. Figure 2 illustrates these forces.

As a bubble forms from a nucleation site on the heater surface, the sum of the forces in each direction must equal zero, $\sum F_x = 0$ and $\sum F_y = 0$. Bubble departure occurs when either of these conditions is violated such that detaching forces exceed the attaching forces. Specifically, if $\sum F_x = 0$ is violated before $\sum F_y = 0$, then the bubble will slide along the heater surface before detaching. In this case, bubble departure will be based upon the point at which $\sum F_x$ becomes greater than zero. If the opposite is true, and $\sum F_y = 0$ is violated before $\sum F_x = 0$, then bubble will detach without sliding and the point at which $\sum F_y$ becomes greater than zero will determine the criterion for bubble departure [5, 24].

The surface tension force was modeled by Klausner et al. (1993) as follows:

$$F_{sx} = -1.25 d_w \sigma \frac{\pi(\alpha - \beta)}{\pi^2 - (\alpha - \beta)^2} \tag{3.3}$$

in the x-direction and as the following, in the y-direction:

$$F_{sy} = -d_w \sigma \frac{\pi}{\alpha - \beta} [cos\beta - cos\alpha] \tag{3.4}$$

where d_w is the bubble contact diameter on the heater surface, σ is the surface tension, α is the advancing contact angle, and β is the receding contact angle. Klausner recommended a constant

contact diameter of 0.009mm based on his experimental data set. Yun et al. improved the model by incorporating a constant fraction factor, d_b, where $d_w/d_b = 1/15$ which proves to be more accurate for the smaller contact diameters that would arise in high pressure flow conditions [21]. However, Zeng at al. suggested that this surface tension force be neglected because it is significantly smaller than other, more dominant buoyancy and growth forces. Their contention is supported by experimental data that indicates the magnitude of the contact diameter of a bubble near its point of departure is insignificant [24].

The quasi-steady drag force is the dominant component of the unsteady drag which exists over a stationary bubble in viscous flow. The memory or history term and added mass component of the unsteady drag also have proven to be insignificant [24]. Klausner suggested the following model, which is an expression that assumes a spherical bubble in uniform flow:

$$F_{qs} = 6\pi\nu\rho_l\Delta v R\left[\frac{2}{3} + \left[\left(\frac{12}{Re_b}\right)^n + 0.796^n\right]^{-1/n}\right] \tag{3.5}$$

where ρ_l is the liquid (water) density, Δv is the velocity difference between the vapor bubble and the bulk fluid, ν is the kinematic viscosity of the water, R is the bubble departure radius, n is a variable which is set to 0.65 (in Klausner's model), and Re_b is the Reynolds number of the bulk fluid which can be expressed as

$$Re_b = \frac{\rho_l \Delta v D_e}{\mu_l} \tag{3.6}$$

where μ_l is the dynamic viscosity of the bulk fluid, and D_e is the equivalent hydraulic diameter, defined by:

$$D_e = \frac{4A_f}{P_w} \tag{3.7}$$

where A_f is the flow area and P_w is the wetted perimeter of the channel. The time-averaged velocity profile, which is assumed to follow Reichardt's turbulent single-phase flow relation, can be used to evaluate the velocity of the bulk fluid. Specifically,

$$\frac{U(y)}{u^*} = \frac{1}{\kappa}ln(1+\kappa y^+) + c\left[1 - exp\left(-\frac{y^+}{\chi}\right) - \frac{y^+}{\chi}exp(-0.33y^+)\right] \tag{3.8}$$

where U(y) represents the fluid velocity at a distance y away from the wall, τ_w is the wall shear stress, ν is the kinematic viscosity, κ is a constant set to 0.4, χ is set to 11, c is set to 7.4, and y^+ and U^* are defined as follows:

$$y^+ = \frac{yu^*}{\nu} \tag{3.9}$$

and

$$u^* = \sqrt{\frac{\tau_w}{\rho}} \tag{3.10}$$

Klausner instead used a relationship between u^* and u_l, the mean liquid velocity for two-phase flow. For his experimental setup, u^*/u_l is 0.04, and u_l is defined as

$$u_l = \frac{G(1-X)D}{\rho_l \delta} \tag{3.11}$$

where G is the mass flux, X is the vapor quality, δ is the liquid film thickness, ρ_l is the liquid density, and D is the inner width of the flow channel. Klausner's original model requires knowledge of the liquid film thickness, so in the present study, u^* will be calculated directly from Equation 3.10 to be used in the turbulent velocity profile, and the following relationship will determine the wall shear stress.

$$\tau_w = \frac{f}{4}\rho\frac{v_l^2}{2} \tag{3.12}$$

where f is the friction factor, and v_l is the velocity of the bulk fluid (based on the mass flux in the test section).

The buoyancy force can be expressed as

$$F_b = V_b(\rho_l - \rho_v)g = \frac{4}{3}\pi R^3(\rho_l - \rho_v)g \tag{3.13}$$

where V_b is the bubble volume, ρ_l is the liquid density, ρ_v is the vapor bubble density, and g is the gravitational acceleration. This force makes a contribution in both the x and y directions based on the inclination of the heater surface. The x-component of the buoyancy force will have a $\cos\vartheta$ multiplier and the y-component will have a $\sin\vartheta$ multiplier, as shown in Equations 3.1 and 3.2 above.

The shear lift force can be approximated using the following equation, as presented by Klausner

$$F_{sL} = \frac{1}{2}\rho_l \Delta v^2 \pi R^2 \left[3.877 G_s^{1/2} \left[Re_b^{-2} + 0.014 G_s^2\right]^{1/4}\right] \tag{3.14}$$

where ρ_l is the liquid (water) density, Δv is the velocity difference between the vapor bubble and the bulk fluid, R is the bubble departure radius, Re_b is the bubble's Reynolds number, and G_s is the non-dimensional liquid shear gradient, given by

$$G_s = \frac{dv}{dy}\frac{R}{\Delta v} \tag{3.15}$$

where y is the distance from the wall. As with the quasi-steady drag force, the velocity of the bulk fluid is used for Δv since the velocity of the bubble is approximately zero at the point of interest. Manipulation of frictional pressure drop equations yields the following relationship for dv/dy at the wall

$$\frac{dv}{dy} = \frac{\tau_w}{\mu} = \frac{f}{8\mu}\rho_l v^2 \tag{3.16}$$

where f is the friction factor for turbulent flow, μ is the dynamic viscosity of the bulk fluid, ρ_l is the liquid density, and v is the velocity of the bulk fluid. Yun et al. modified the equation for the shear lift force by adjusting the second G_s multiplier from 0.014 to 0.118 [21].

The hydrodynamic pressure force, which arises due to the pressure on top of the bubble's symmetric area of $\pi d_w^2/4$, can be expressed as:

$$F_h = \frac{9}{8}\rho_l \Delta v^2 \frac{\pi d_w^2}{4} \tag{3.17}$$

where ρ_l is the liquid density, Δv is the velocity difference between the vapor bubble and the bulk fluid (the velocity of the bulk fluid is used here), and d_w is the bubble contact diameter on the heater surface.

The contact pressure force arises due to the pressure difference between the inside and outside pressure of the bubble. Specifically:

$$F_{cp} = \frac{\pi d_w^2}{4}\frac{2\sigma}{r_r} \tag{3.18}$$

where r_r is the radius of curvature of the base of the bubble, d_w is the bubble contact diameter on the heater surface, and σ is the surface tension. Since the ratio of d_w to r_r is much smaller than 1, the contact pressure force term can be neglected in the force balance.

Finally, an unsteady force arises due to asymmetrical bubble growth and is essentially a measure of inertia. In Klausner's original work, the following equation was suggested for the unsteady force

$$F_{du} = -\rho_l \pi R^2 \left(\frac{3}{2} C_s \dot{R}^2 + R\ddot{R} \right) \tag{3.19}$$

where ρ_l is the density of the bulk fluid, R is the bubble departure radius, $\dot{R}$ is the first differentiation with respect to time, and $\ddot{R}$ is the second differentiation with respect to time. The constant, C_s, was introduced later by Zeng et al. in order to account for the presence of a wall (heater, in this case) [24]. This force has a contribution in both the x and y directions and acts in the direction opposite of flow, therefore having a negative contribution in both directions. Klausner used the following expression that was originally developed by Mikic et al. [25] to predict the time rate of change of the radius for a spherical bubble:

$$R(t) = \frac{2}{3} \frac{B^2}{A} \left[(t^+ + 1)^{3/2} - (t^+)^{3/2} - 1 \right] \tag{3.20}$$

where

$$t^+ = \frac{A^2 t}{B^2} \tag{3.21}$$

and B and A are related to the wall superheat, ΔT_{sat}, and are expressed as

$$A = \left[\frac{\pi}{7} \frac{h_{fg} \rho_v \Delta T_{sat}}{\rho_l T_{sat}} \right]^{1/2} \tag{3.22}$$

and

$$B = \left[\frac{12}{\pi} \eta_l \right]^{1/2} \frac{\Delta T_{sat} c_{pl} \rho_l}{h_{fg} \rho_v} \tag{3.23}$$

h_{fg} is the latent heat of vaporization, ρ_v is the vapor density, ρ_l is the liquid density, η_l is the liquid thermal diffusivity, and c_{pl} is the liquid specific heat.

Zeng and Klausner [24] later suggested the use of Zuber's bubble growth model, below, for the formulations of R and its time differentiations [28] such that:

$$R(t) = \frac{2b}{\sqrt{\pi}} Ja\sqrt{\nu t} \tag{3.24}$$

where the Jakob number is

$$Ja = \frac{\rho_l C_{pl} \Delta T_{sat}}{\rho_v h_{fg}} \tag{3.25}$$

and b is a constant which accounts for aspherity, η is the liquid thermal diffusivity ($\eta = k_l/\rho_l c_{pl}$), t is time, ρ_l is the liquid density of water, C_{pl} is the liquid specific heat, ΔT_{sat} is the liquid superheat temperature difference (between the heater and the bulk fluid), ρ_v is the vapor density of water, and h_{fg} is the latent heat of vaporization.

In Klausner's original bubble growth model, bubble condensation around a growing bubble was not considered, a condition which is only valid if the temperature of the bulk fluid reaches saturation. In a later improvement to the model, Yun et al. took bubble condensation and liquid subcooling into account, which resulted in modifications, shown below, to the time rate of change in the radius of a bubble [21]:

$$R(t) = \frac{2b}{\sqrt{\pi}} Ja\sqrt{\eta t}\left[1 - \frac{q_l'' \sqrt{\pi \eta t}}{2sk(T_{wall} - T_{sat})}\right] = \frac{2b}{\sqrt{\pi}} Ja\sqrt{\eta t} - \frac{bq_l''}{sh_{fg}\rho_g} t \tag{3.26}$$

where the coefficient b is 1.56, s is 2, Ja, η, t, h_{fg}, and ρ_g are the same as defined above. Yun et al. also suggested the following relationship for q

$$q = h_i(T_{sat} - T_l) \tag{3.27}$$

where h_i is the interfacial heat transfer coefficient. This can be expressed in terms of a non-dimensional Nusselt number (shown below) and then a heat transfer correlation can be applied.

$$Nu = \frac{h_i d_b}{k_l} \tag{3.28}$$

where d_b is the bubble diameter and k_l is the thermal conductivity of the bulk fluid. The heat

transfer correlation that was used by Yun et al. [21] was the Ranz and Marshall correlation which models the Nusselt number as

$$Nu = 2 + 0.6Re_b^{0.5}Pr^{0.3} \tag{3.29}$$

where Re_b is the Reynolds number of the bubble and Pr is the Prandtl number for the liquid. Since the velocity of the bubble immediately before its departure can be approximated as zero, its respective Reynolds number is roughly that of the bulk fluid. Thus, combining these expressions for Nusselt number gives the following equation for the interfacial heat transfer coefficient:

$$h_i = \frac{k}{d_b}\left(2 + 0.6Re_b^{0.5}Pr^{0.3}\right) \tag{3.30}$$

Solving this set of equations is a tedious, iterative process. Many of the parameters are known and set based on the specific experimental setup. These are used as inputs, and values for bubble departure diameter can be solved iteratively using Matlab. Equations 3.1 and 3.2 are effectively two equations with two unknowns - bubble size and time of departure - which can be solved via Equations 3.3 through 3.30, making this a complete system of equations. As mentioned earlier, departure can occur either when the sum of forces in the x-direction exceeds the sum of the forces in the y-direction, or vice versa.

Several trends can be predicted based on this model. Because of several inverse relationships to the Reynolds number (and Re $\propto$ v) throughout the force balance equations, an increase in velocity will cause bubble diameters to decrease. Specifically, it should follow a power law relationship (d $\sim$ 1/v), meaning that small changes in velocity will result in significant changes in diameter, especially at low velocities. Thus, as mass flux increases, bubble departure diameter will decrease.

Likewise, because of the ideal gas law (PV = nRT), an increase in pressure will cause a decrease in vapor volume, which scales with the radius cubed. The effect of heat flux on bubble diameter is not as significant, but it is expected that an increase in heat flux will result in larger bubble diameters because of the increase in wall superheat that would arise from the increase in heat flux. Subcooling should not have much of an effect because of the boundary layer that would

form under these conditions along the heater surface. Since the bubble sizes that are predicted under these flow conditions are smaller than the predicted width of this boundary layer, the bulk fluid subcooling should not affect the amount to which each bubble will grow before detaching. Finally, based on the explained convention that 0° corresponds to a downward-facing horizontal heater and 90° corresponds to a vertical heater, bubble departure diameter should increase as orientation angle decreases. This is explained by the various components of the dominant forces in x and y directions as the heater becomes more inclined from a downward-facing horizontal position.

The primary conclusions from Klausner's model validation were that bubble departure diameter increases with increasing heat flux and decreasing mass flux (and velocity). Further, superheat seems to affect bubble departure in that an increase in superheat results in larger bubble diameters. Finally, it was concluded that bubble departure is significantly different in flow boiling as compared with pool boiling, which most of the existing models are based on. Therefore, it is crucial to generate additional data in order to develop a model that applies directly to flow boiling conditions, which are important in nuclear power plant applications.

4 Experimental Setup

4.1 Flow Loop Description

The primary components in the experimental flow loop include a pump, pre-heater, test section, accumulator, condenser, power supply, Nitrogen gas tank, measurement instrumentation, and data acquisition system. These components will be discussed in more detail below. A schematic and photo of the loop are shown in Figures 3 and 4 respectively.

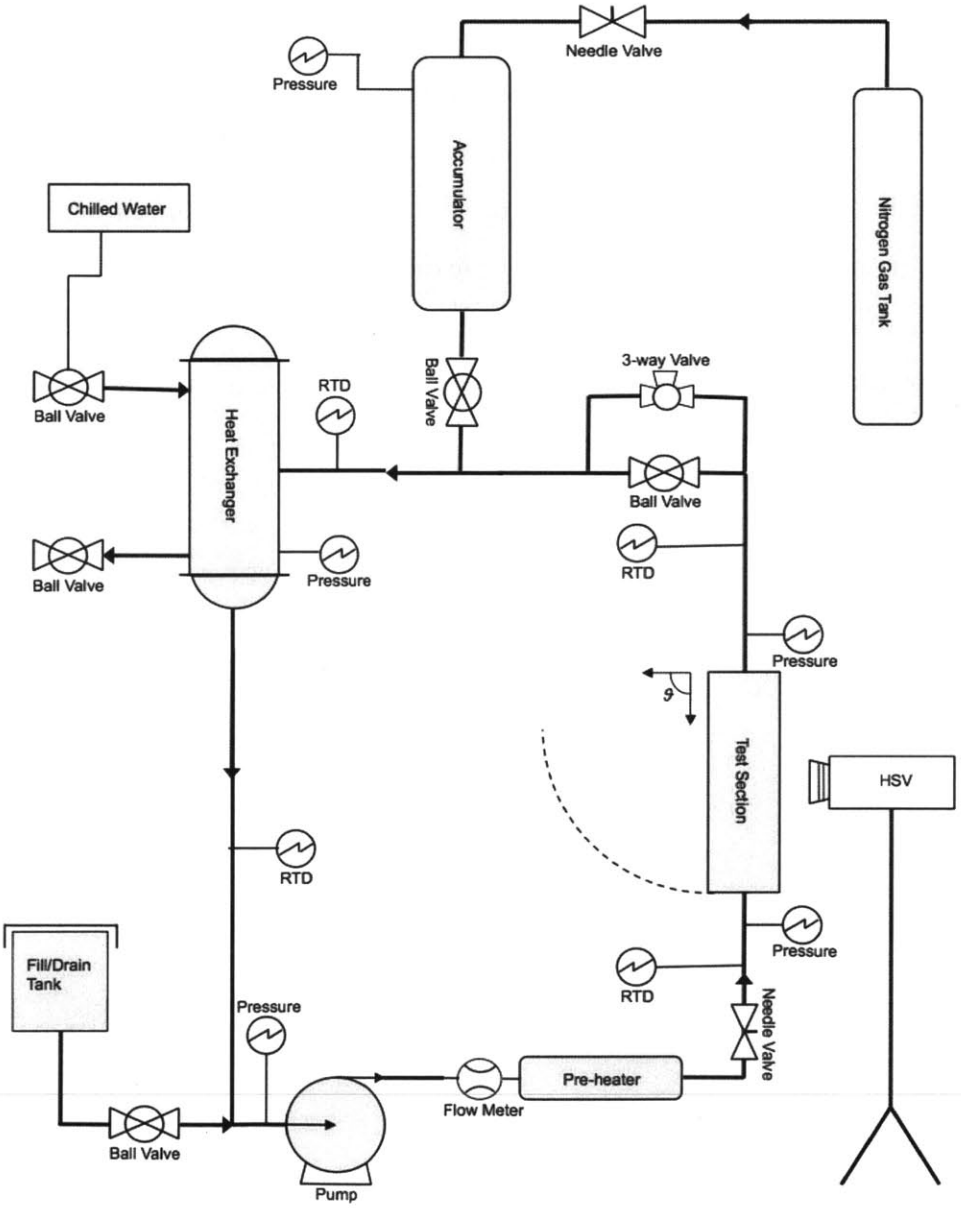

Figure 3: Schematic of the single closed flow loop. Loop taken from and designed by G.L. DeWitt, Ph.D. thesis [29].

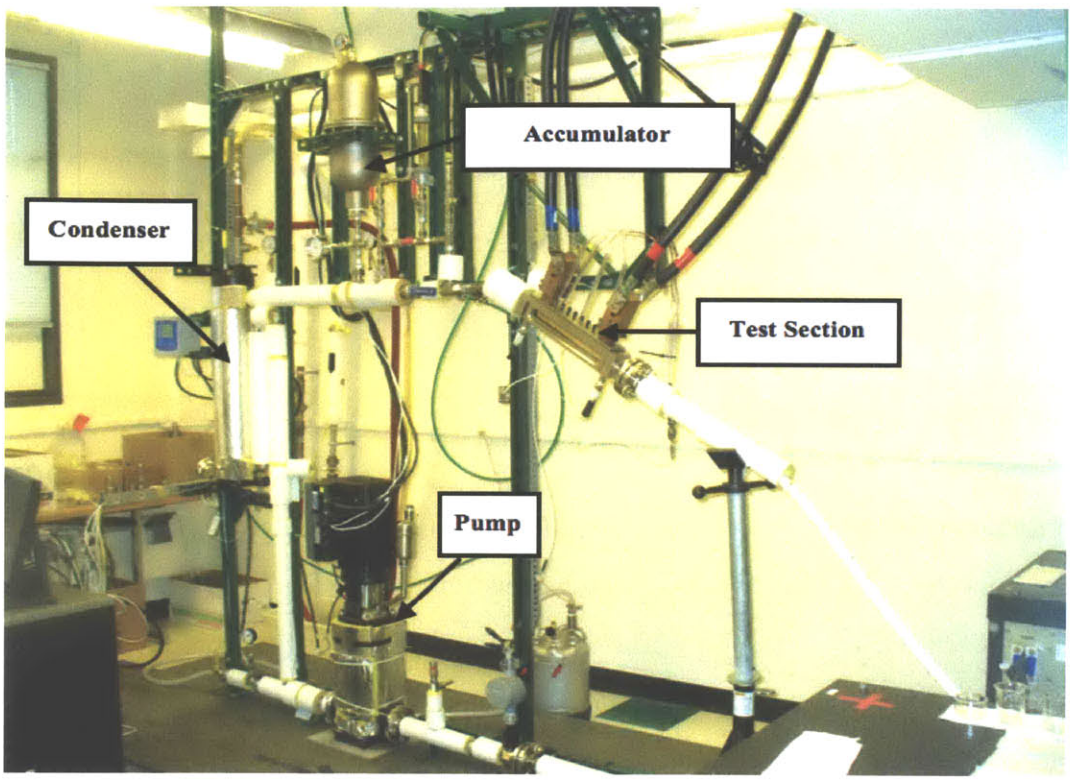

Figure 4: Photo of the two-phase flow loop [29].

A variable speed Grundfos centrifugal pump, model A97518318-P10943121, which can reach a maximum of 58.4 liters per minute (or 15.4 gpm), is used to drive the bulk fluid (DI water) through the loop at various mass fluxes. Since the mass fluxes of interest in this experiment are relatively low, a needle valve, located after the pump and before the test section, is used for fine tuning adjustments at low pump settings.

A 2 kW immersion pre-heater is used to control the bulk fluid at the desired temperatures as it enters the test section. It also protects the pump from cavitation by allowing for the required pump inlet subcooling. This, along with the chilled water system, is used to reach the desired levels of subcooling during the various experimental runs. Images of the preheater are shown in Figure 5 below.

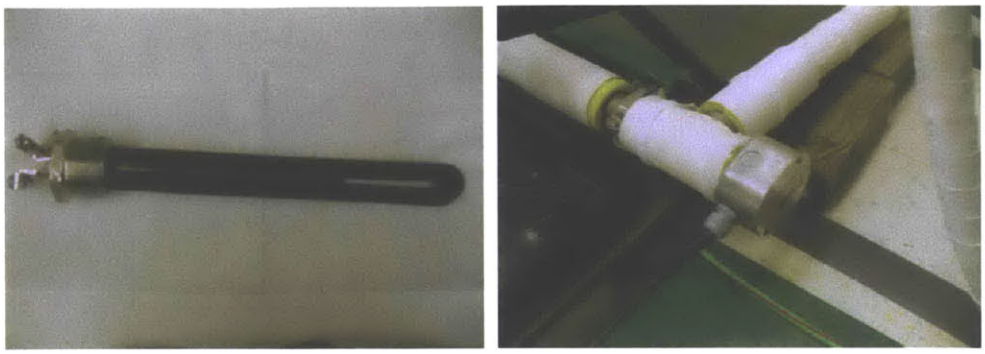

Figure 5: Images of the immersion heater used in the loop [29].

The test section consists of a rectangular stainless steel (316L) body and frame, two viewing windows (front and back), a heater, and a Macor insulator. The heater is flat, 1 cm wide by 24 cm long, made of SS316L and fits into a Macor ceramic insulator, which acts as both an electrical insulator and a high thermal resistor. The receding and advancing contact angles of water on the heater surface at room temperature are 8° and 91° respectively, as measured with a goniometer, and the surface roughness is 1.22μm, as determined using confocal microscopy. The rectangular flow channel through the test section body has a width of 0.0143 m, a height of 0.0199 m, an equivalent diameter of 0.0167 m, and a heated length of 0.24 m. Figure 6 shows drawings of the test section body with specific dimensions, Figure 7 shows drawings of the heater, and Figure 8 shows drawings of the Macor ceramic insulator. The assembly of the test section with the body, frame, viewing windows, heater, Macor insulator, and copper studs is shown in Figure 9.

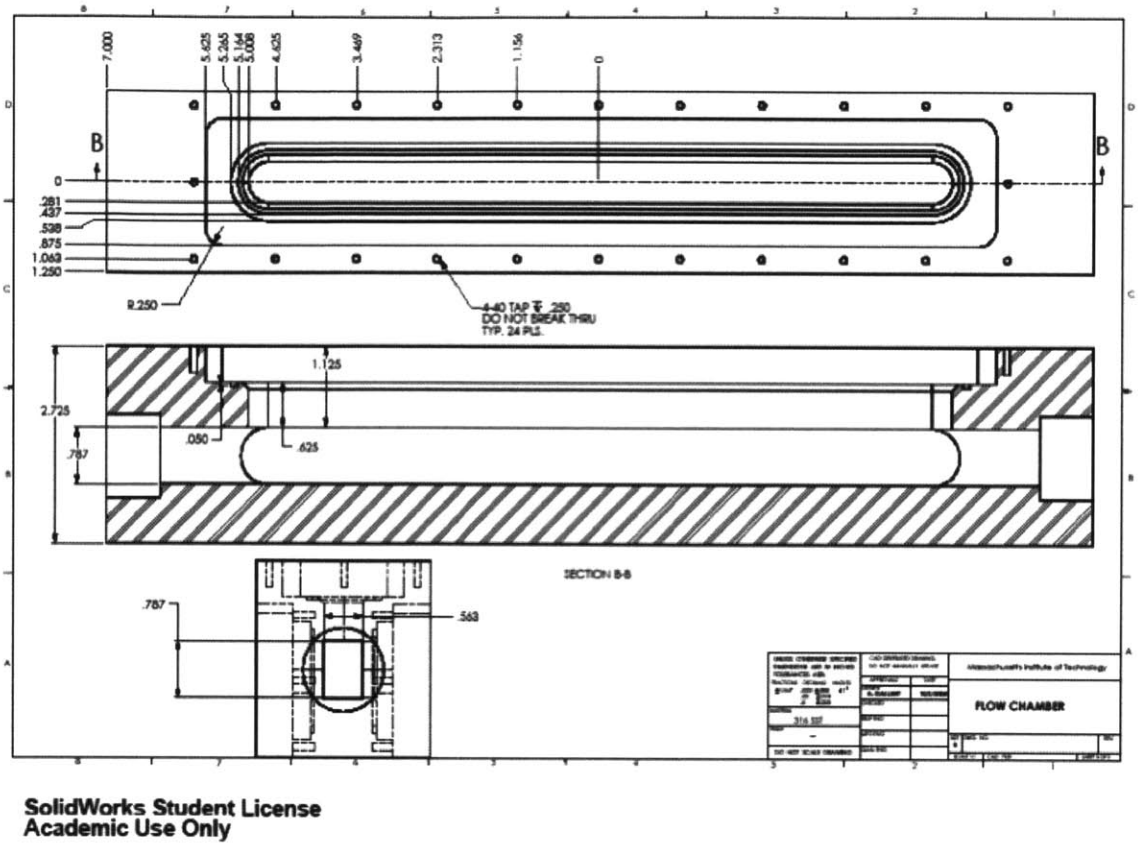

Figure 6: SolidWorks drawings of the test section body [29].

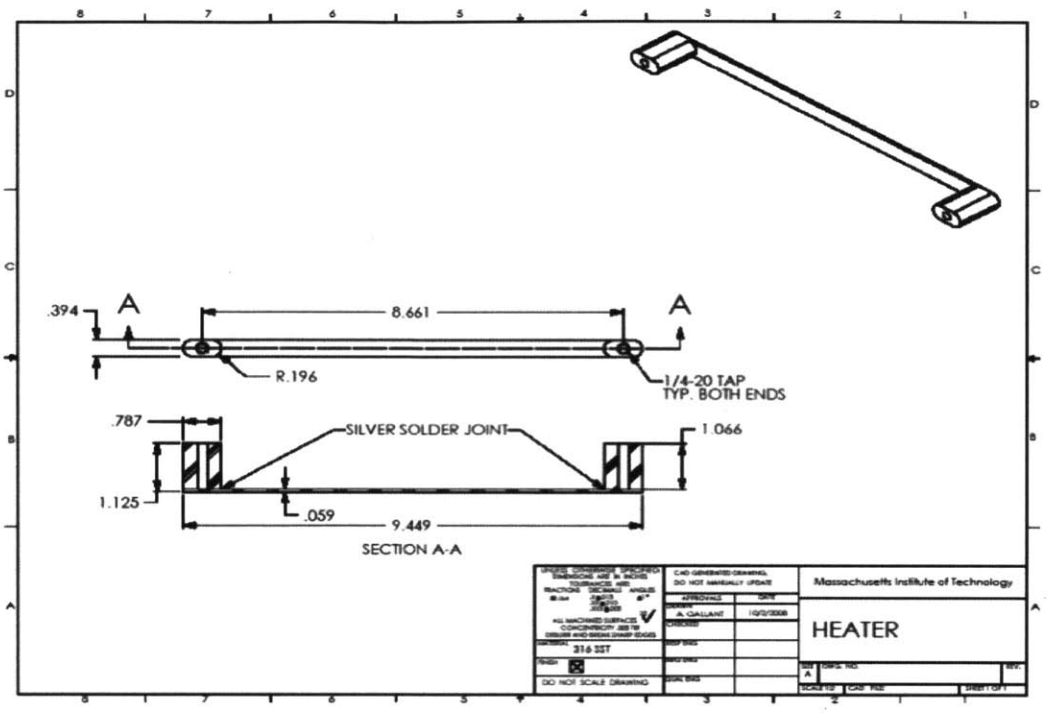

Figure 7: SolidWorks drawings of the heater [29].

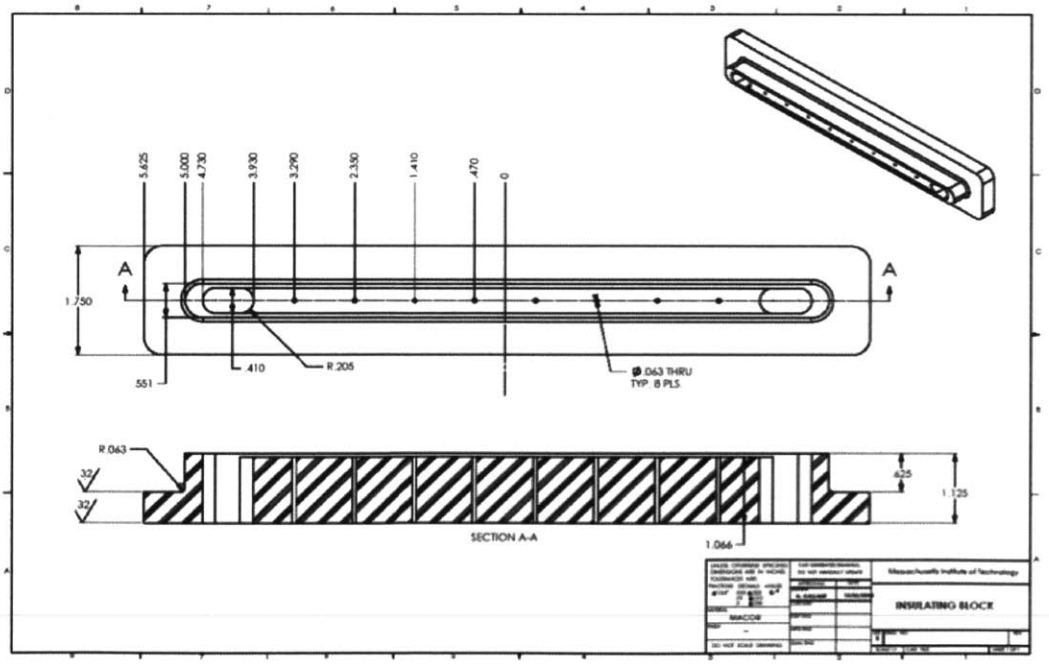

Figure 8: SolidWorks drawings of the Macor ceramic insulator [29].

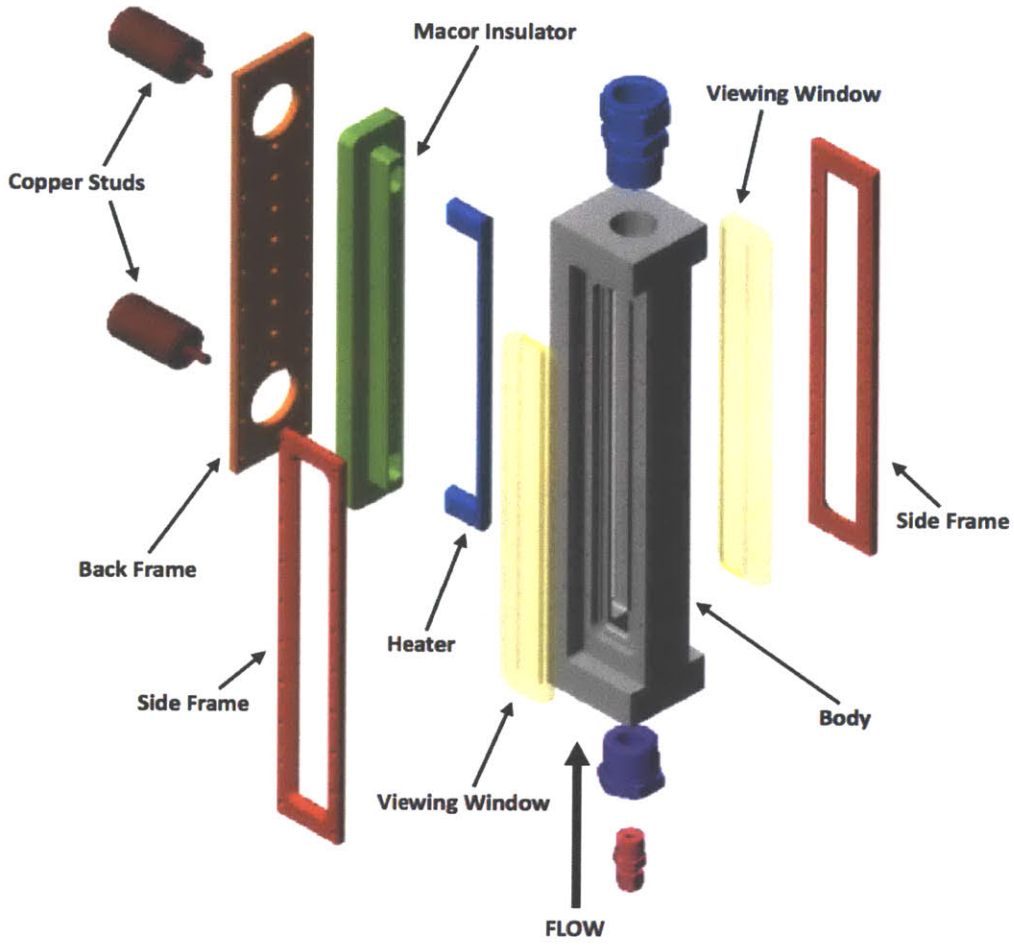

Figure 9: Schematic of the test section assembly [29].

Copper studs, used as connections to the power supply lines that provide DC current, are screwed into the ends of the heater. Eight thermocouples are screwed into the back of the ceramic insulator and touch the back of the heater to provide temperature readings throughout the experiments. The downward facing test section can be adjusted for any angle because it is connected to the loop by a stainless steel reinforced flexible (viton) tube and a 90° elbow compression fitting. Figures 10 and 11 show the heater and test sample (heater fitted inside of the Macor insulator), and the test section attached to the loop at different orientation angles, respectively.

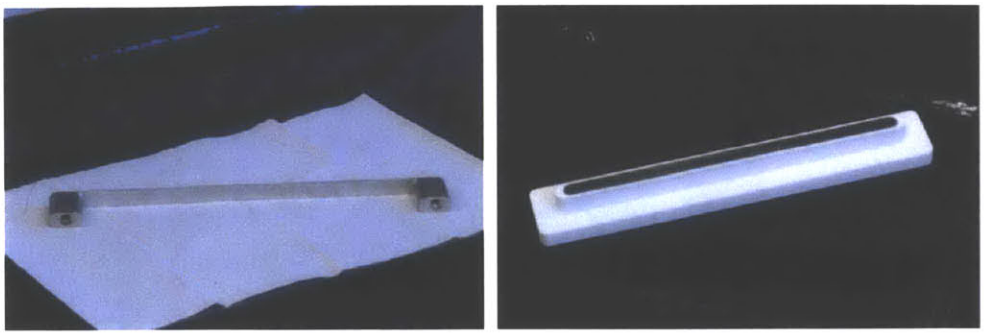

Figure 10: Images of the heater and the Macor ceramic insulator used in the test section of the loop [29].

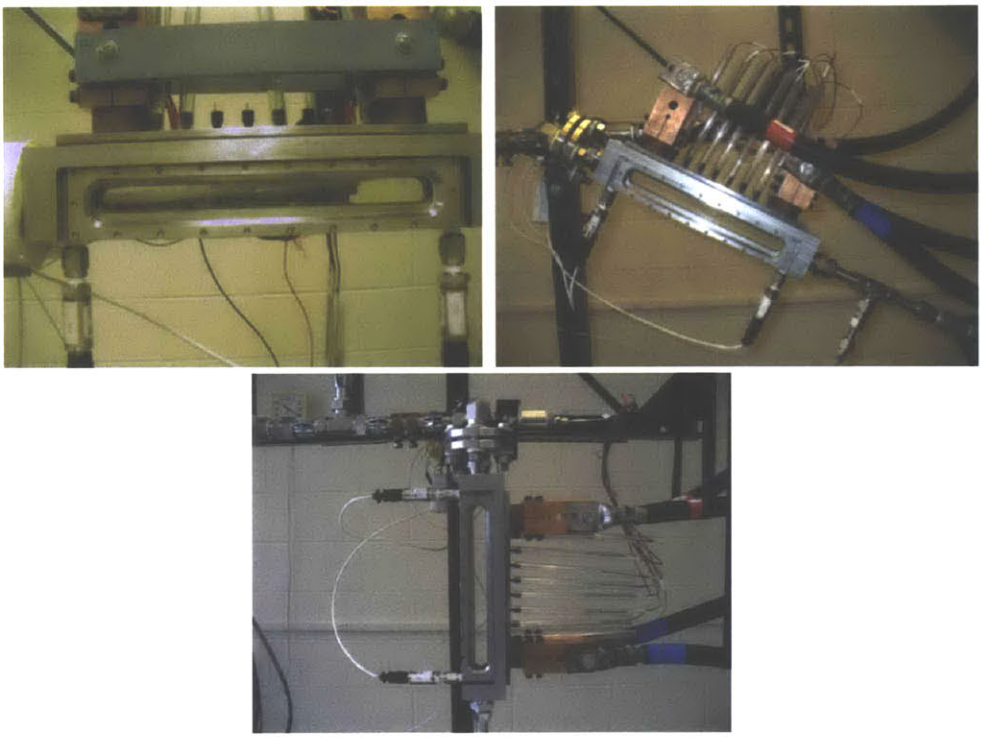

Figure 11: Photos of the downward facing test section at 0° (downward-facing horizontal), 45°, and 90° (vertical) [29].

An accumulator, a Blacoh CT2420V bladder-style design which acts as a shield between the nitrogen cover gas and the bulk fluid, is used to adjust for volume expansion which results from boiling during experiments. The condenser and heat sink in the loop is a Thermasys heat exchanger. Chilled water is provided to the top side of the condenser, and single phase fluid is released at the bottom where it enters the loop to the pump.

Two 18 kW DC power supplies, each capable of delivering up to 30 Volts and 600 amperes of current, are utilized to provide joule heating in the test section. As can be seen in Figure 12, they are connected to four locomotive cables, two for each DC power supply, which attach to the positive and negative copper electrodes on the back side of the test section.

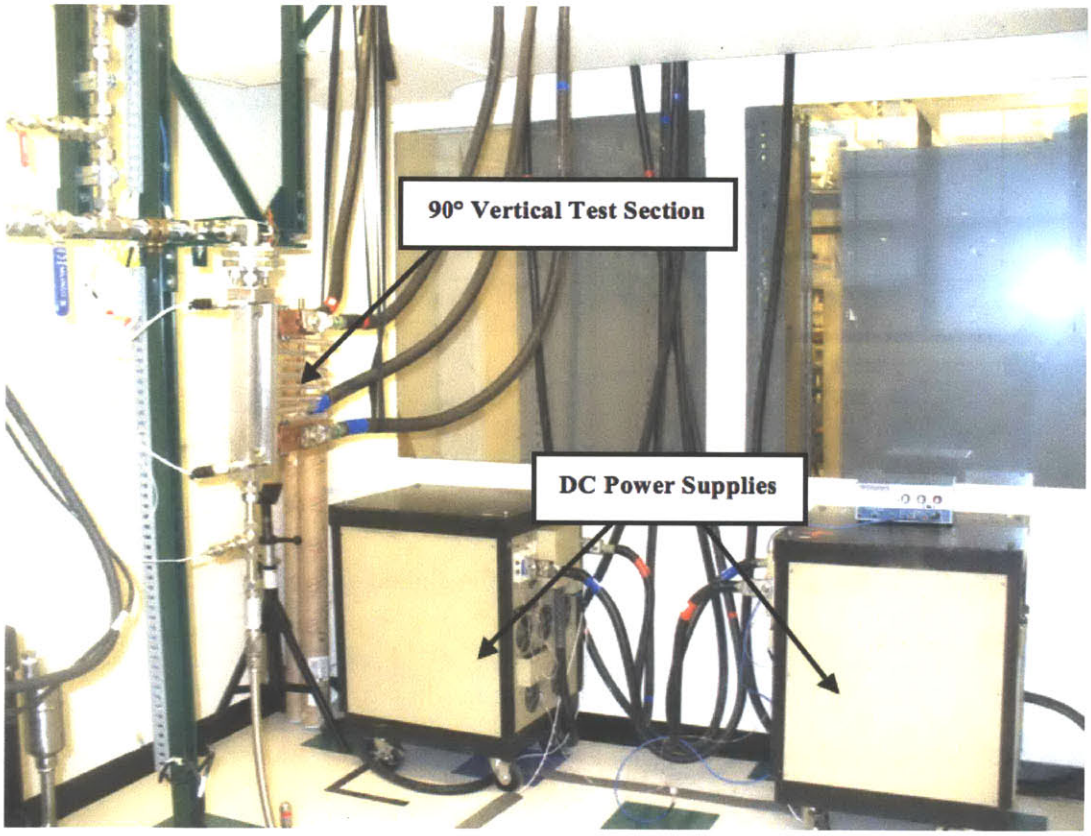

Figure 12: Photo of the DC power supplies connected to the back side of the test section [29].

A nitrogen gas system, shown in Figure 13, is used to set the system pressure and is connected to the top of the accumulator and to the fill tank. The line to the accumulator is usually left open so that atmospheric pressure can be maintained. It is also used in the beginning of an experiment to assist in bringing water into the loop. The fill tank is closed and pressurized so that water can be pushed through to the top of the loop, making it completely water solid.

Figure 13: Photo of the Nitrogen Gas System with lines to the accumulator and fill tank [29].

To maintain the temperature at the desired level of subcooling during the experimental conditions, a chilled water system is connected to the experimental loop which supplies water at about 10°C, at a constant pressure of approximately 7 bar gauge and a maximum possible flowrate of 5 gpm. A small needle valve is used for fine adjustments of the chilled water flow rate.

All wetted pipes, tubes, fittings, and valves (ball and needle) are made of type 316L stainless steel. In order to minimize heat loss, the loop is insulated with a paper-reinforced fiberglass.

LabVIEW software is used to acquire and process data during the experiments. It is usually set to a scan rate of once every three seconds, which is sufficient as measurements are made at equilibrium. The Data Acquisition System receives signals from five types of measurement instrumentation in the loop - temperature, pressure, flow rate, voltage drop, and current.

Four RTDs are used to measure the bulk fluid temperature in the loop. The first is located in between the outlet of the condenser and the inlet of the pump; the second between the pump outlet and the inlet of the test section; the third right after the test section; and the fourth immediately prior to the inlet of the condenser. The RTDs right before and after the test section are used to calculate the bulk temperature at the nucleation site of interest during experiments, based on its

distance between the two. Four Type-K thermocouples are used to measure the temperature of the back of the heater.

Four pressure transducers, which are located at various spots around the loop - one after the pump (PT1), two on the inlet and outlet of the test section (PT2 and PT3), and one on the condenser (PT4) - are used to measure pressure. There are also five visual pressure gauges around the loop. Two flow meters in the loop determine the flow rate - a turbine type flow meter on the hot water side (located right after the pump), and a vortex type on the chilled water side. The voltage drop across the test section is measured with the data acquisition system through two leads that are attached to the bolts which clamp the copper blocks onto the sample. Finally, two LEM inductive current transducers are used to measure the current from the two 18 kW DC power supplies (30 V and 600 A). The specific manufacturer and model numbers for the measurement instrumentation are presented in Table 2.

Table 2: Specifications of measurement instrumentation in the loop [29].

Measurement	**Manufacturer**	**Model**	**Label in Loop**
Temperature	Omega	PR-11-3-100-1/8-6-E	RTDs
		KMQXL-125U-6	Type Ks
Pressure	Omega	PX329-200A5V	PT2, PT3
	Danfoss	MBS3000	PT1
	Ashcroft	Xmitr25 X 1009 SD 02L 1FL	PT4
Turbine Flow Meter	Omega	FTB-1422	FM1
Vortex Flow Meter	Omega	FV103	FM2
Current	LEM	AHR 800 B10	PS1, PS3
Voltage Drop	Agilent	34980A	TSVD

4.2 High Speed Video Camera

A Phantom V12 high-speed video camera, shown in Figure 14, is used to measure the bubble departure diameter during experimental runs. The camera has a detector resolution of 1280x800 pixels and is capable of capturing images at a rate of 6242 frames per second at full image size (and up to 10^6 fps at a reduced number of pixels per image size). Three Digital Promaster Nikon extension rings (12mm, 20mm, and 36mm) are used to increase the magnification with a 200mm Nikon lens.

Two Lowel DC powered LED lights are used as direct backlighting during the experiments. They provide sufficient light for the desired camera acquisition rate and avoid the flickering associated with AC power, one of the typical problems associated with high-speed video for clear visualization [6].

Figure 14: Photo of the high-speed video camera with the three extension rings and 200mm Nikon lens.

5 Test Procedure

5.1 Setup

To initiate the experiments, the test section is adjusted at the desired orientation angle. 10 liters of de-ionized water are added to the fill tank and heated up to roughly 60°C using a 1kW immersion heater. After the water reaches this temperature, the fill tank is covered in order to minimize heat losses while the rest of the loop is set up. Meanwhile, the test section is prepared and assembled.

A heater is sandblasted and rinsed with water and acetone before being attached to the Macor insulating block. Sandblasting is done with silicon oxide, SiO_2, with particle size ranging from 210 to 305 μm. Copper tape is used to insure good electrical contact between the ends of the heater onto the insulator. This part of the test section and the two copper electrodes (which are used as connections to the power supply cables) are then heated to 110°C in a box furnace. The furnace temperature is set at 10° above the expected saturation temperature (usually 100°C). After removal, the copper electrodes are screwed into the test section (consisting of the Macor insulator and heater) which is done to protect the heater from bowing during the experiment due to thermal expansion of the heater.

A cover plate is screwed onto the back of the test section with twenty-four screws, and eight thermocouples are used to further secure the test section onto the experimental loop. Four of the eight thermocouples are actually used during the experiments, located at either end and at the center (approximate location of a typical nucleation site) of the heater. At this point, the loop is closed. All valves leading out of the system are closed, including the cork on top of the upper (degassing) loop. A line is then connected to a vacuum pump. The pump is turned on and the needle valve leading to the line is slowly opened and closed. The pressure reading decreases to approximately -28 psi at this point. Once the system is vacuumed, it is ready to be filled with water.

The ball valve at the bottom of the loop, leading to the fill tank, is then opened, which causes water to rush in due to the low pressure in the system. Since the water usually does not fill the loop completely, a nitrogen tank is used to increase the pressure on top of the accumulator and

the (covered) fill tank through two lines that go to each. Fine adjustments can then be made, as needed, by opening and closing ball valves. The system is then checked for any obvious leaks.

Once the system is water tight, the pump is turned on and a baseline test with a wide range of mass fluxes is conducted to insure a leak proof system, particularly in the test section. LabView software is then activated, the power supplies are turned on, and the system is ready for the initiation of the heat process.

5.2 Experiment

An inline heater is used to help raise the bulk temperature, while the power supplies are set to increasing levels in slow increments. The pump is initiated at a low setting of around 1.5 and the needle valve downstream is adjusted to reach desired mass fluxes.

Degassing is initiated once the fluid reaches 60°C by allowing non-condensible gases to exit the loop into the fill tank through a degassing line located on the top side of the loop. This is done in ten minute intervals until no bubbles appear to be released through the degassing line.

Once the bulk fluid heats to approximately 80°C, fine adjustments are made using the preheater and chilled water system to maintain a desired level of subcooling (within ±0.5°C). The subcooling is then decreased by adjusting chilled water flow and preheater power, and the heat and mass flux are easily adjusted according to the test matrix.

A single nucleation site is chosen approximately one third of the way up the heater, based on its activity at low heat flux and high subcooling, and is used for the range of parameters in the experimental matrix. High-speed videos are recorded for ten bubbles from that same nucleation site at each set of operating conditions.

5.3 HSV Setup

The high speed video camera is positioned while the rest of the loop heats up to the desired level of subcooling. A tripod is assembled roughly two feet in front of the test section to support the camera. Three extension rings (12mm, 20mm, and 36mm) are connected to the 200mm lens for an increase in magnification.

One of the problems associated with high speed video for clear visualization is the need for direct lighting [6]. To solve this problem, as well as AC to DC flickering interference issues, Lowel LED Blender lights were utilized to add the brightness necessary for crisp test section imagery. Figure 15 shows the HSV experimental setup.

Figure 15: Photo of the high speed video during an experiment with a horizontal test section.

5.4 Quantification of Experimental Uncertainties

Uncertainties are present in all measured quantities throughout the loop. Specifically, those from instrumentation are given by the manufacturers and are supported by calibration. These uncertainties are presented below in the form of measurement accuracy, which is defined as the 95% confidence interval ($2\sigma_{std}$), or better [29].

Table 3: Quantification of experimental uncertainties from instrumentation [29].

Measurement	**Manufacturer**	**Label in Loop**	**Accuracy**
Temperature	Omega	RTDs	± 0.35°
		Type Ks	± 1.1°
Pressure	Omega	PT2, PT3	± 0.25% full scale (0.5 psi)
	Danfoss	PT1	± 1.0% full scale (2 psi)
	Ashcroft	PT4	± 1.5% BFSL (psi)
Turbine Flow Meter	Omega	FM1	± 1.0% of reading (0.075 gpm)
Vortex Flow Meter	Omega	FM2	± 2.0% full scale (0.5 gpm)
Current	LEM	PS1, PS3	± 1% of FS (8 A)
Voltage Drop	Agilent	TSVD	± 0.004% of reading (V)
Orientation Angle	Wixley	θ	± 0.1°

Other uncertainties occur during the actual bubble measurement process. In order to minimize error and to scale the videos from pixels into meaningful units, a reticle is calibrated after each experiment. Specifically, the reticle is set at the location of the nucleation site particular for each run, and an image of the reticle is then recorded, as it would be for a bubble's departure, and its size is calculated in terms of the number of pixels. This is then scaled based on its actual size in order to set a conversion from pixels into millimeters. From this, it was determined that the conversion from pixels to millimeters is 0.01905mm/pixel. This was verified in both a water and dry environment to make sure that refraction through the liquid did not influence the size. However, given the resolution of the images, bubble diameters can only be determined up to a 1 pixel certainty, and thus an error of ±0.01905mm is assumed.

The potential errors presented throughout the experimental results for bubble departure diameter

arise from data spread (standard deviation) around a mean value of diameter. Each mean represents the average of at least ten data points that were collected for that specific setup in the test matrix.

6 Experimental Matrix and Results

6.1 Experimental Test Matrix

The main parameters of interest in this research are mass flux, heat flux, subcooling, and orientation angle of the heater surface. Bubble diameters are measured for various combinations of these variables at atmospheric pressure. As verified by applying Klausner's model, orientation angle does not affect bubble size at high mass fluxes, so the values of interest are in the range of 250 kg/m^{2}s to 400 kg/m^{2}s. The heat flux values used in the test matrix are 0.05 MW/m^2 and 0.1 MW/m^2, and the subcooling range is from 10°C to 20°C. The test section is set up in vertical (90°), 60°, 45°, 30°, and downward-facing horizontal (0°) orientations, which correspond to the heater surface inclination angles. All experiments are run at atmospheric pressure with a downward-facing test section. However, several additional runs with a horizontal test section are conducted to explore the effects of increased pressure on bubble size. Table 6.1 below shows the specific variables of interest.

Table 4: Experimental test matrix - variables of interest.

Parameter	**Units**	**Experiment Range**
Angle:	[degrees]	0, 30, 45, 60, 90
Mass Flux:	[kg/m^{2}s]	250, 300, 350, 400
Subcooling:	[degrees Celsius]	10, 20
Heat Flux:	[MW/m^2]	0.05, 0.1
Pressure:	[kPa]	101, 202, 505

6.2 Results for Experimental Test Matrix

A complete presentation of the results from the experimental test matrix can be found in Tables 5 and 6. Table 5 shows the full test matrix for all orientation angles at atmospheric pressure, and Table 6 shows the data from the elevated pressure experiments. The errors reported on all values of diameter are the standard deviations from the spread of data around a mean diameter, and given the resolution of the images, the minimum value is the size of a pixel, 0.01905 mm.

Specific results and discussions from the various orientation angles will then be presented in the sections following these summary tables.

Table 5: Summary of experimental results at atmospheric pressure. The first line in each row presents the bubble diameters and their related uncertainty, defined as the standard deviation of 10 bubbles or the lower limit of resolution (±0.019 mm), whichever is larger. The second line shows the wall temperature at the nucleation site of interest. Subcooling is given in °C, heat flux in MW/m^2, mass flux in kg/m^{2}s, and diameters in mm.

P	ΔT_{sub}	q"	G	0°	30°	45°	60°	90°
101 kPa	20	0.05	250	0.615±0.026 102°C	0.547±0.019 102°C	0.514±0.087 102°C	0.471±0.019 102°C	0.372±0.019 102°C
			300	0.528±0.019 102°C	0.446±0.019 102°C	0.421±0.113 102°C	0.391±0.019 102°C	0.295±0.019 102°C
			350	0.429±0.019 102°C	0.375±0.019 102°C	0.377±0.101 102°C	0.333±0.019 102°C	0.267±0.019 102°C
			400	0.389±0.019 102°C	0.312±0.019 102°C	0.325±0.035 102°C	0.299±0.019 102°C	0.229±0.019 102°C
		0.10	250	0.632±0.029 105°C	0.598±0.022 104°C	0.532±0.069 105°C	0.497±0.019 105°C	0.381±0.019 104°C
			300	0.560±0.028 104°C	0.444±0.028 104°C	0.439±0.030 105°C	0.389±0.025 105°C	0.324±0.019 104°C
			350	0.453±0.045 104°C	0.392±0.019 104°C	0.399±0.036 104°C	0.356±0.019 104°C	0.267±0.019 104°C
			400	0.434±0.033 104°C	0.337±0.019 105°C	0.331±0.044 104°C	0.286±0.019 104°C	0.248±0.019 104°C
	10	0.05	250	0.623±0.034 103°C	0.581±0.051 103°C	0.538±0.096 103°C	0.457±0.030 103°C	0.362±0.001 103°C
			300	0.503±0.033 103°C	0.453±0.021 103°C	0.478±0.095 103°C	0.379±0.019 103°C	0.314±0.019 103°C
			350	0.432±0.020 103°C	0.381±0.020 103°C	0.405±0.070 103°C	0.345±0.019 103°C	0.295±0.019 103°C
			400	0.370±0.033 103°C	0.345±0.019 103°C	0.349±0.050 103°C	0.301±0.019 103°C	0.248±0.019 103°C
		0.10	250	0.668±0.070 106°C	0.625±0.060 106°C	0.519±0.067 106°C	0.463±0.021 106°C	0.391±0.019 106°C
			300	0.518±0.052 106°C	0.490±0.050 106°C	0.427±0.042 106°C	0.358±0.020 106°C	0.352±0.019 106°C
			350	0.440±0.042 106°C	0.394±0.029 106°C	0.373±0.046 106°C	0.333±0.019 106°C	0.305±0.019 106°C
			400	0.358±0.020 106°C	0.324±0.019 106°C	0.333±0.030 106°C	0.305±0.019 106°C	0.267±0.019 106°C

Table 6: Summary of experimental results for elevated pressures and a downward-facing horizontal (0°) heater. The first line in each row presents the diameters (and related uncertainty), and the second line shows the measured wall temperature at the nucleation site of interest. Subcooling is given in °C, heat flux in MW/m^2, mass flux in kg/m^2s, and diameters in mm. The uncertainty on the values of the wall temperature is ±1°C.

ΔT_{sub}	q"	G	P = 202 kPa	P = 505 kPa
20	0.05	250	0.573±0.050 119°C	0.262 ±0.022 153°C
		300	0.456±0.073 119°C	0.192±0.022 153°C
		350	0.357±0.039 119°C	0.166±0.029 153°C
		400	0.337±0.046 120°C	0.160±0.026 153°C
	0.10	250	0.605±0.056 120°C	0.413±0.019 155°C
		300	0.533±0.064 120°C	0.290±0.020 155°C
		350	0.427±0.050 120°C	0.261±0.019 155°C
		400	0.387±0.022 120°C	0.224±0.019 155°C
10	0.05	250	0.419±0.025 122°C	0.282±0.024 155°C
		300	0.373±0.024 122°C	0.255±0.019 155°C
		350	0.322±0.035 122°C	0.231±0.019 155°C
		400	0.320±0.039 122°C	0.194±0.019 155°C
	0.10	250	0.511±0.064 122°C	0.326±0.032 157°C
		300	0.384±0.045 123°C	0.288±0.019 157°C
		350	0.357±0.027 123°C	0.278±0.019 157°C
		400	0.322±0.037 123°C	0.236±0.019 157°C

6.2.1 Vertical Test Section

The results from a test section in the vertical (90°) position will first be presented and discussed. The errors reported on the diameters are the values of the standard deviation from the spread of data around a mean value, which was calculated as an average of at least ten data points. Each setup in the experimental matrix was repeated as a reliability check.

Table 7 presents the bubble departure diameter data from a vertical test section at atmospheric pressure (101 kPa) for 20°C and 10°C subcooling. As can be seen, the observed trends show that diameters increase with decreasing mass flux, increasing heat flux, and, to a lesser extent, with decreasing amounts of subcooling.

Table 7: Bubble departure diameters off a vertical heater for 20°C and 10°C subcooling. Diameters are given in units of mm.

20°C subcooling		
Mass Flux (kg/m^2s):	**q" = 0.05 MW/m^2:**	**q" = 0.10 MW/m^2:**
400	0.2286±0.0190	0.2477±0.0190
350	0.2667±0.0190	0.2667±0.0190
300	0.2953±0.0190	0.3239±0.0190
250	0.3715±0.0190	0.3810±0.0190
10°C subcooling		
Mass Flux (kg/m^2s):	**q" = 0.05 MW/m^2:**	**q" = 0.10 MW/m^2:**
400	0.2477±0.0190	0.2667±0.0190
350	0.2953±0.0190	0.3048±0.0190
300	0.3143±0.0190	0.3524±0.0190
250	0.3620±0.0190	0.3905±0.0190

6.2.2 Angled Test Section

The downward-facing test section was inclined at orientation angles of 60°, 45°, and 30° in order to investigate the effect that orientation angle has on bubble departure diameter. These results

were compared to those from the vertical and horizontal test section position. All results from the angled test sections were taken at atmospheric pressure (101 kPa).

Table 8 shows bubble departure diameter results from a test section at an angle of 60° for 20°C and 10°C subcooling. These data seem to follow similar trends, in terms of mass flux, heat flux, and subcooling, as those seen from the data collected with a vertical test section. Specifically, bubble departure diameters increase with decreasing mass flux, increasing heat flux, and with decreasing amounts of subcooling.

Table 8: Bubble departure diameters off a 60° heater for 20°C and 10°C subcooling. Diameters are given in units of mm.

20°C subcooling		
Mass Flux (kg/m^2s):	**q" = 0.05 MW/m^2:**	**q" = 0.10 MW/m^2:**
400	0.2991±0.0190	0.2858±0.0190
350	0.3334±0.0190	0.3562±0.0190
300	0.3905±0.0190	0.3886±0.0247
250	0.4705±0.0190	0.4972±0.0190
10°C subcooling		
Mass Flux (kg/m^2s):	**q" = 0.05 MW/m^2:**	**q" = 0.10 MW/m^2:**
400	0.3010±0.0190	0.3048±0.0190
350	0.3448±0.0190	0.3334±0.0190
300	0.3791±0.0190	0.3581±0.0198
250	0.4572±0.0301	0.4629±0.0209

Bubble departure data from a 45° test section for 20°C and 10°C subcooling are shown in Table 9. Similar to the results from the 60° test section, these data also follow trends consistent with those recorded from the vertical test section (e.g., bubble departure diameter increases with decreasing mass flux, increasing heat flux, and, to a lesser extent, with decreasing levels of subcooling).

Table 9: Bubble departure diameters off a 45° heater for 20°C and 10°C subcooling. Diameters are given in units of mm.

20°C subcooling		
Mass Flux (kg/m^2s):	**q" = 0.05 MW/m^2:**	**q" = 0.10 MW/m^2:**
400	0.3249±0.0351	0.3310±0.0440
350	0.3774±0.1012	0.3990±0.0361
300	0.4210±0.1133	0.4393±0.0303
250	0.5144±0.0873	0.5322±0.0688
10°C subcooling		
Mass Flux (kg/m^2s):	**q" = 0.05 MW/m^2:**	**q" = 0.10 MW/m^2:**
400	0.3490±0.0495	0.3334±0.0301
350	0.4048±0.0704	0.3734±0.0462
300	0.4784±0.0953	0.4269±0.0417
250	0.5376±0.0961	0.5191±0.0671

Table 10 presents the bubble departure data from a 30° test section for 20° C and 10°C subcooling. Again, as can be seen, the data are consistent with the trends for the vertical, 60°, and 45° setups.

Table 10: Bubble departure diameters off a 30° heater for 20°C and 10°C subcooling. Diameters are given in units of mm.

20°C subcooling		
Mass Flux (kg/m^2s):	**q" = 0.05 MW/m^2:**	**q" = 0.10 MW/m^2:**
400	0.3119±0.0190	0.3372±0.0190
350	0.3752±0.0190	0.3924±0.0190
300	0.4458±0.0190	0.4439±0.0283
250	0.5467±0.0190	0.5982±0.0217
10°C subcooling		
Mass Flux (kg/m^2s):	**q" = 0.05 MW/m^2:**	**q" = 0.10 MW/m^2:**
400	0.3448±0.0190	0.3239±0.0190
350	0.3810±0.0202	0.3943±0.0290
300	0.4534±0.0209	0.4896±0.0498
250	0.5810±0.0513	0.6246±0.0596

6.2.3 Horizontal Test Section

The largest bubbles were observed off a downward-facing horizontal test section. As expected, diameters followed the same trends observed for the vertical and angled test sections. The specific bubble departure diameter data for a horizontal test section at atmospheric pressure (101 kPa) are presented in Table 11 below.

Table 11: Bubble departure diameters off a horizontal (downward facing) heater for 20°C and 10°C subcooling. Diameters are given in units of mm.

20°C subcooling		
Mass Flux (kg/m^2s):	**q" = 0.05 MW/m^2:**	**q" = 0.10 MW/m^2:**
400	0.3886±0.0190	0.4343±0.0327
350	0.4286±0.0190	0.4534±0.0450
300	0.5277±0.0190	0.5601±0.0281
250	0.6153±0.0257	0.6325±0.0290
10°C subcooling		
Mass Flux (kg/m^2s):	**q" = 0.05 MW/m^2:**	**q" = 0.10 MW/m^2:**
400	0.3696±0.0333	0.3581±0.0198
350	0.4324±0.0198	0.4401±0.0423
300	0.5029±0.0333	0.5182±0.0524
250	0.6229±0.0341	0.6683±0.0696

6.3 General Trends

6.3.1 Effect of Orientation Angle

For downward-facing test sections, bubble departure diameters decrease as orientation angle increases, so the largest bubbles are observed off a horizontal (0°) heater, and the smallest off a vertical (90°) heater. This trend was true for all mass fluxes, heat fluxes, and levels of subcooling in the test matrix. Graphical visualizations of this trend are displayed in Figures 16 through 19.

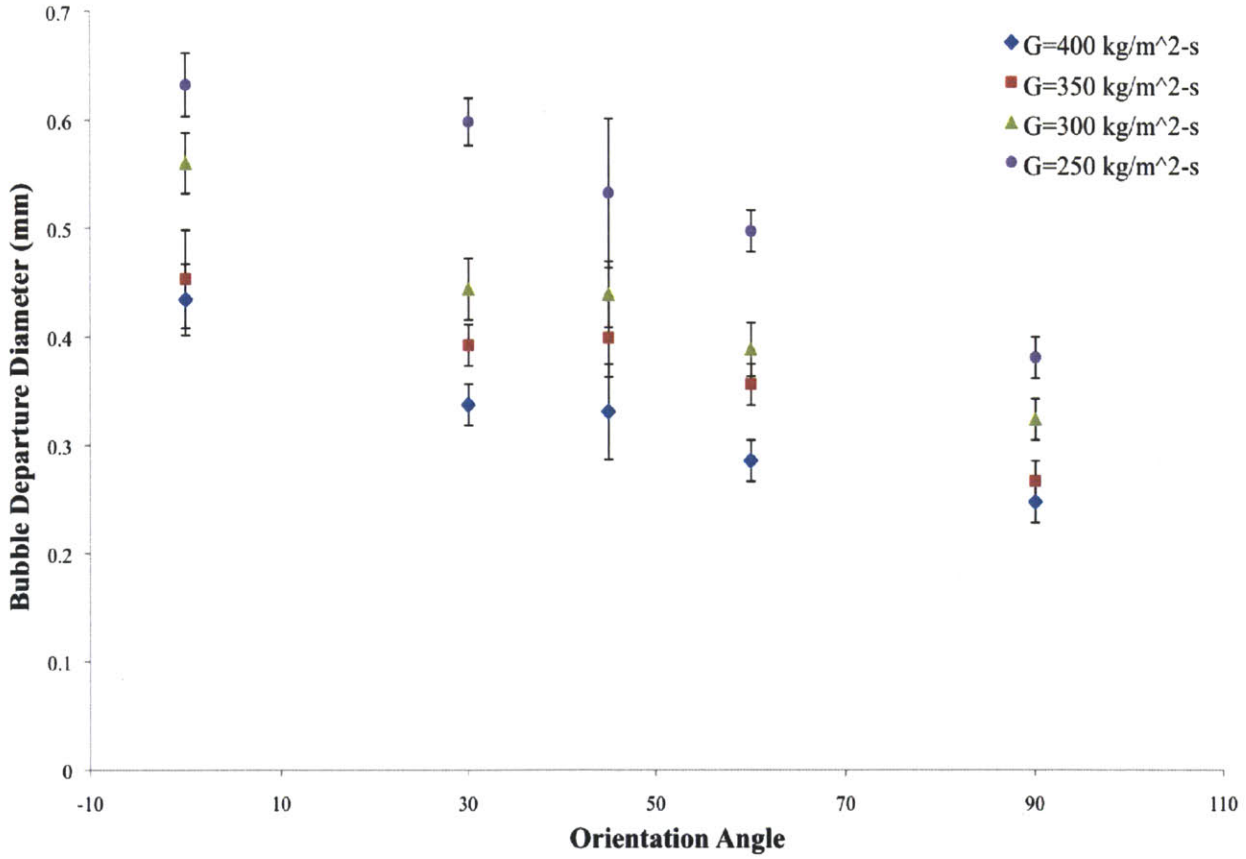

Figure 16: Bubble departure diameter as a function of orientation angle for various mass fluxes, 20°C subcooling and 0.1 MW/m^2 heat flux.

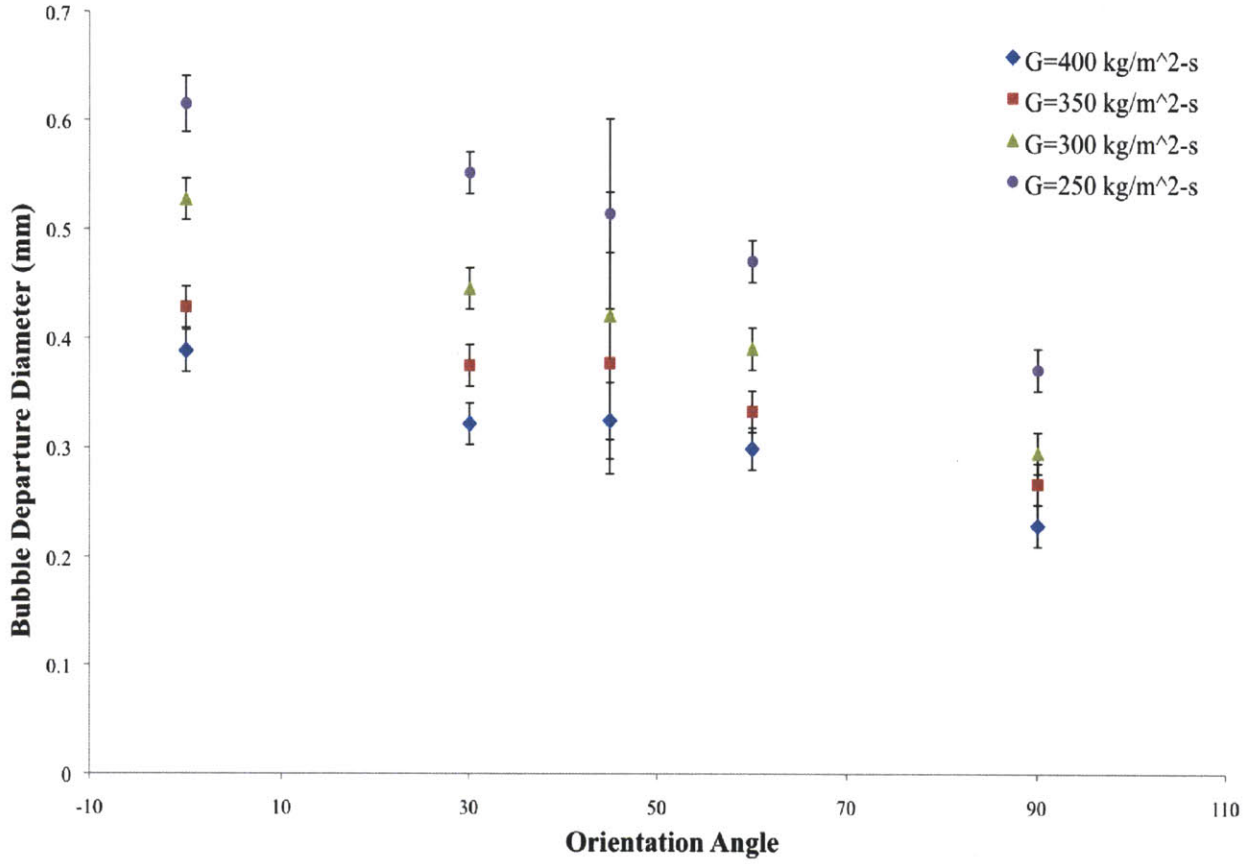

Figure 17: Bubble departure diameter as a function of orientation angle for various mass fluxes, 20°C subcooling and 0.05 MW/m^2 heat flux.

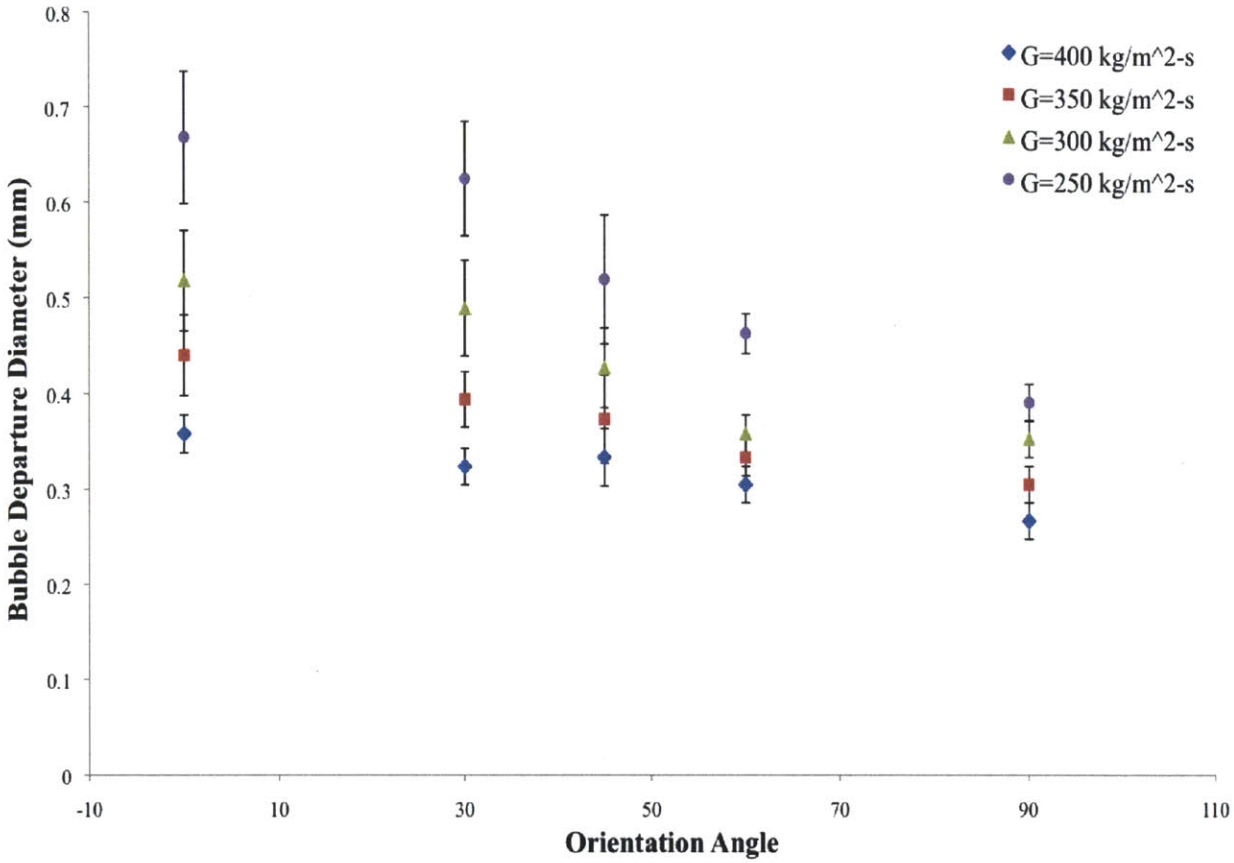

Figure 18: Bubble departure diameter as a function of orientation angle for various mass fluxes, 10°C subcooling and 0.1 MW/m^2 heat flux.

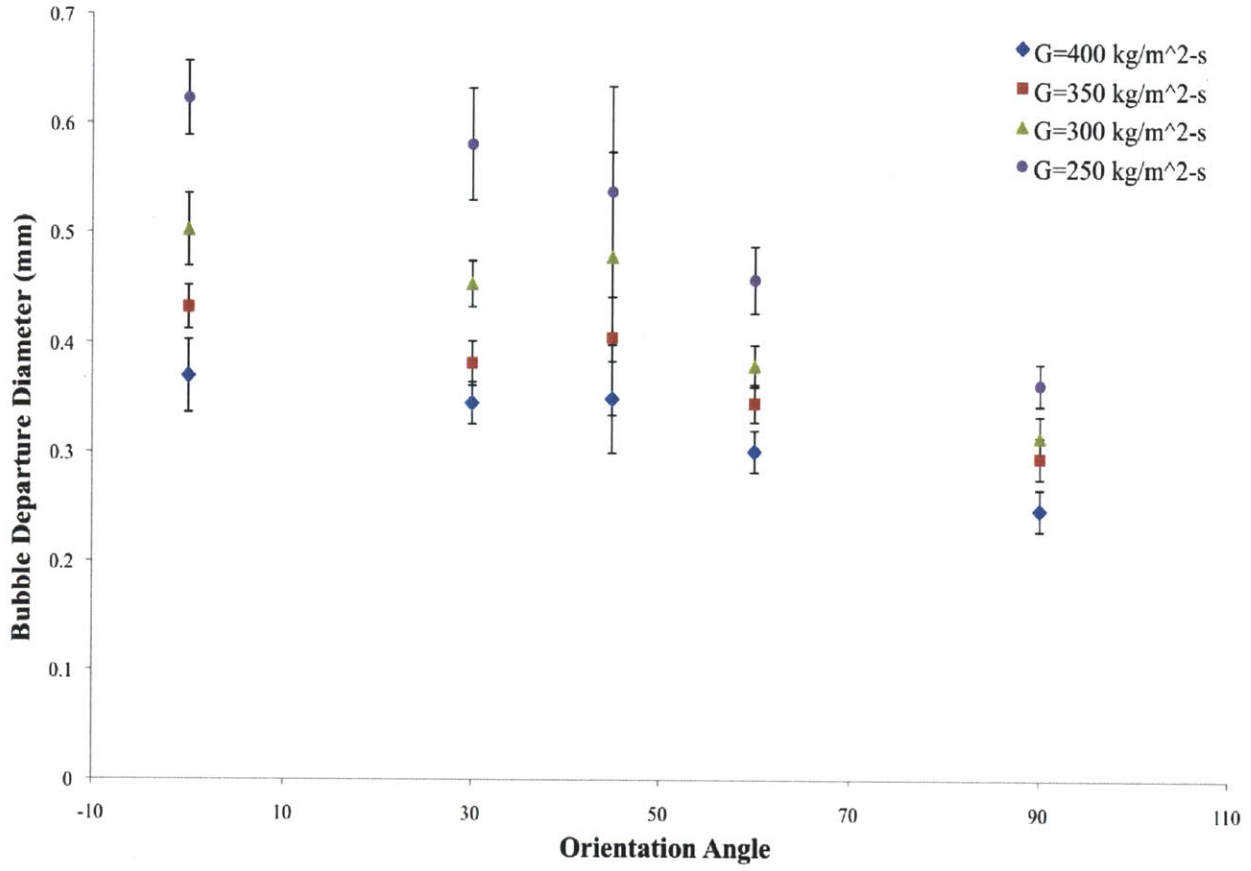

Figure 19: Bubble departure diameter as a function of orientation angle for various mass fluxes, 10°C subcooling and 0.05 MW/m^2 heat flux.

6.3.2 Effect of Pressure

Consistent with the predictions from Klausner's model and the ideal gas law, the bubble volume is inversely proportional to pressure, thus bubble size is inversely proportional to the third root of pressure.

$$PV = nRT \tag{6.1}$$

and

$$V = \frac{3}{4}\pi R^3 \tag{6.2}$$

where V is the volume of a bubble, P is the pressure, and R is the bubble radius. Thus,

$$P \propto 1/V \propto 1/R^3 \tag{6.3}$$

Figures 20, 21, 22, and 23 below show these trends graphically.

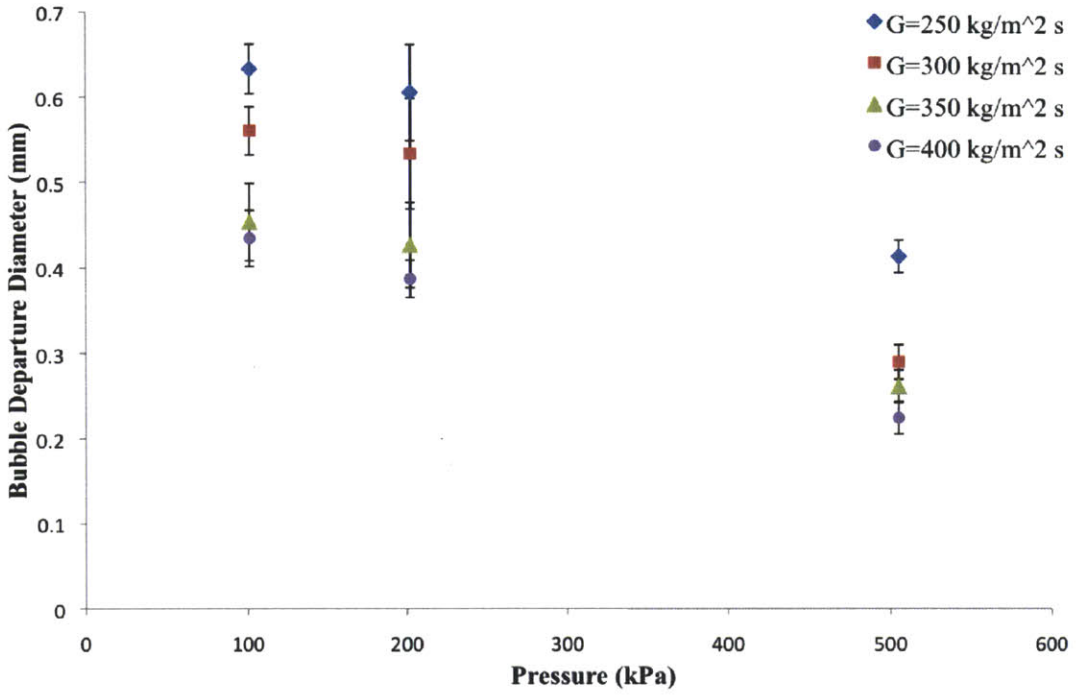

Figure 20: Bubble departure diameter as a function of pressure for various mass fluxes, 20°C subcooling and 0.1 MW/m^2 heat flux.

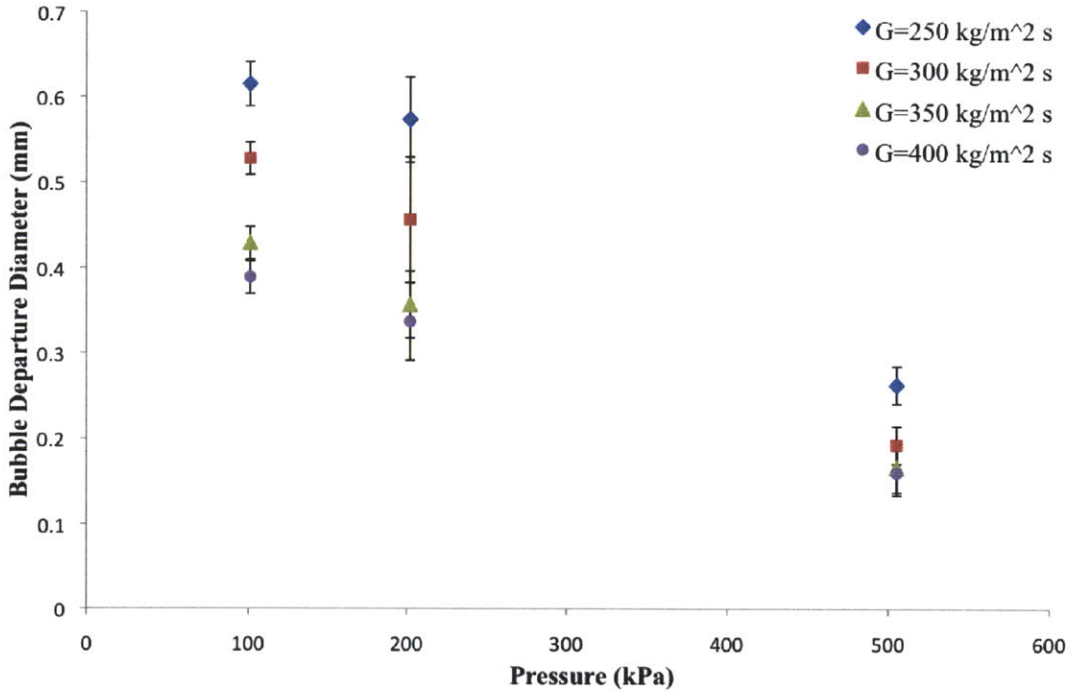

Figure 21: Bubble departure diameter as a function of pressure for various mass fluxes, 20°C subcooling and 0.05 MW/m^2 heat flux.

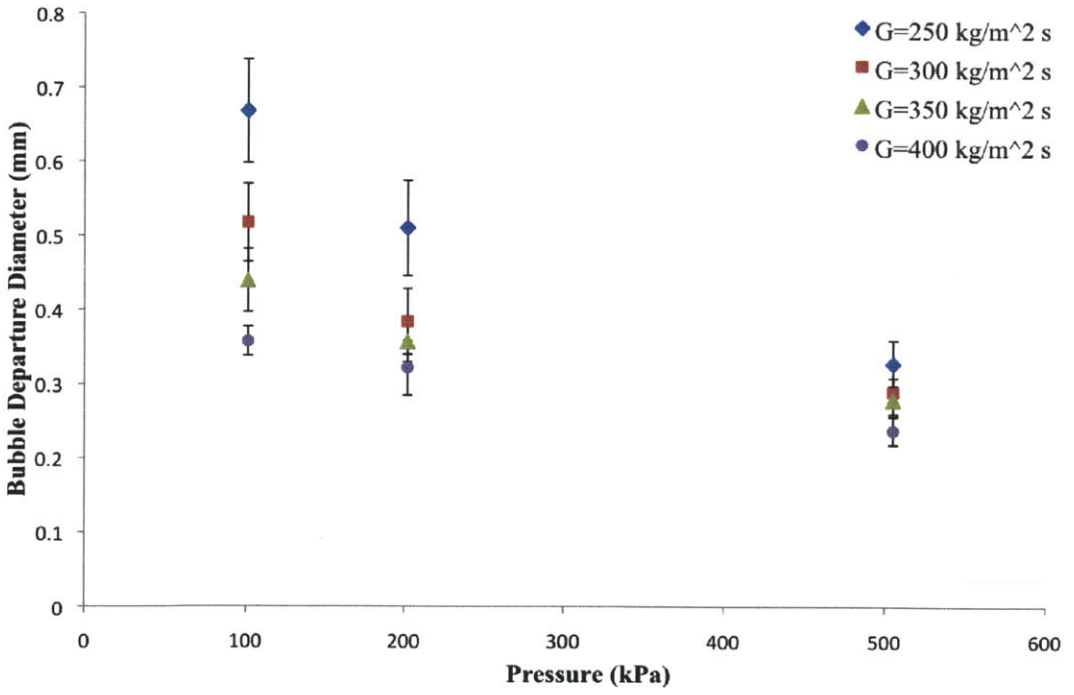

Figure 22: Bubble departure diameter as a function of pressure for various mass fluxes, 10°C subcooling and 0.1 MW/m^2 heat flux.

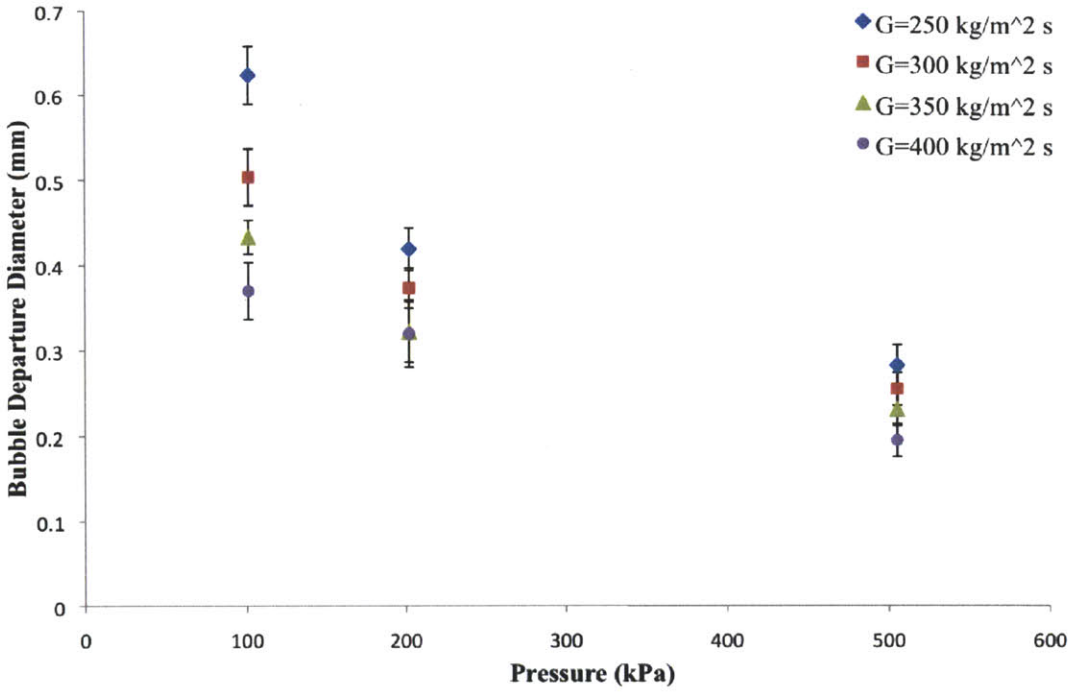

Figure 23: Bubble departure diameter as a function of pressure for various mass fluxes, 10°C subcooling and 0.05 MW/m^2 heat flux.

As can be seen from Figures 20, 21, 22, and 23, as pressure increases, bubble departure diameter decreases for all mass fluxes, heat fluxes, and levels of subcooling.

6.3.3 Effect of Mass Flux

As explained before, the effect of mass flux on bubble departure is such that an increase in mass flux results in a decrease in bubble diameter. Figures 24, 25, 26, and 27 below show this trend graphically.

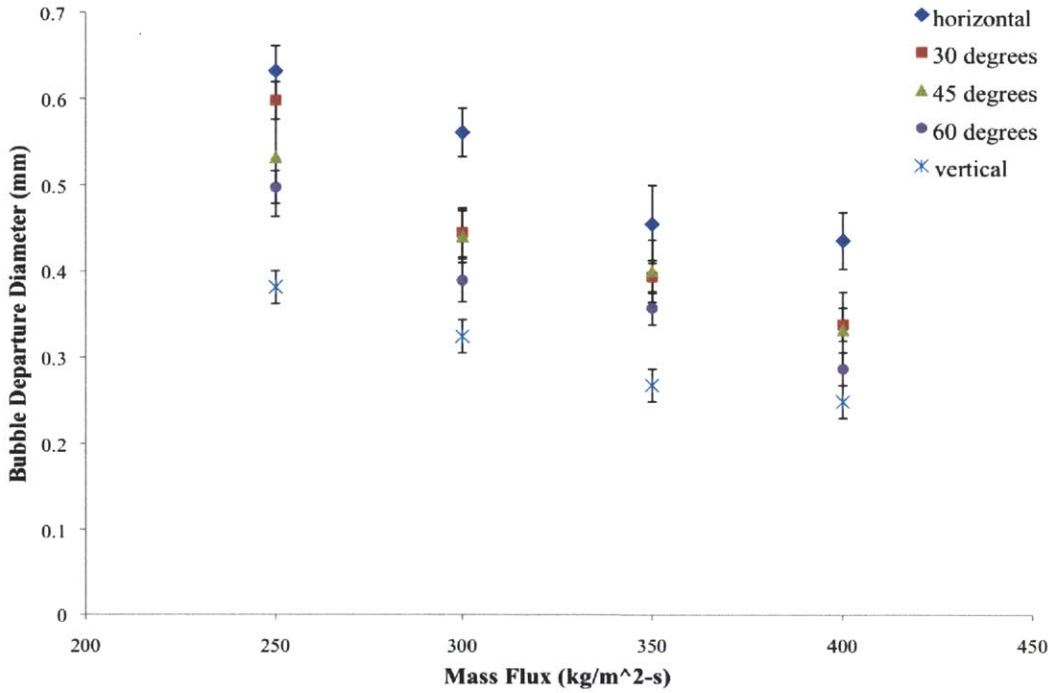

Figure 24: Bubble departure diameter as a function of mass flux for various orientation angles, 20°C subcooling and 0.10 MW/m^2 heat flux.

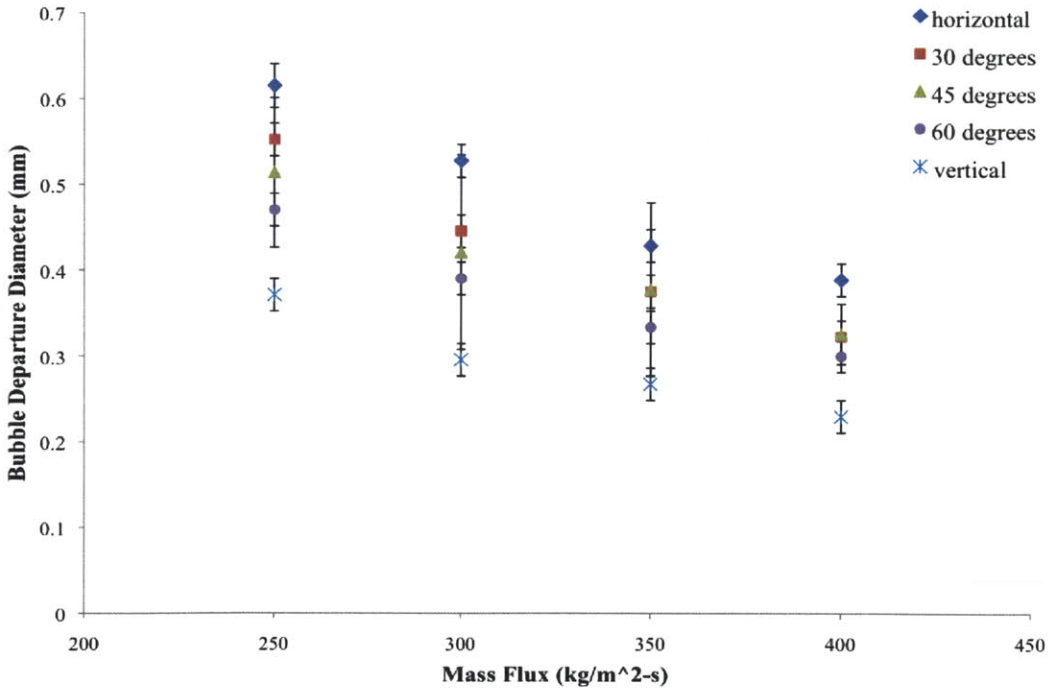

Figure 25: Bubble departure diameter as a function of mass flux for various orientation angles, 20°C subcooling and 0.05 MW/m^2 heat flux.

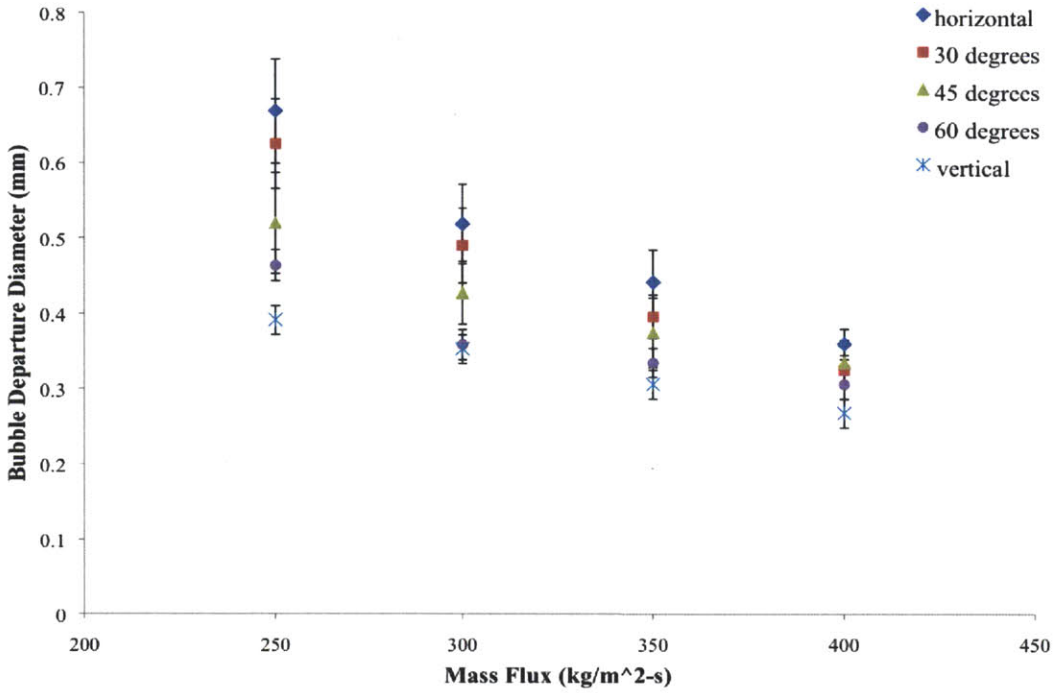

Figure 26: Bubble departure diameter as a function of mass flux for various orientation angles, 10°C subcooling and 0.10 MW/m^2 heat flux.

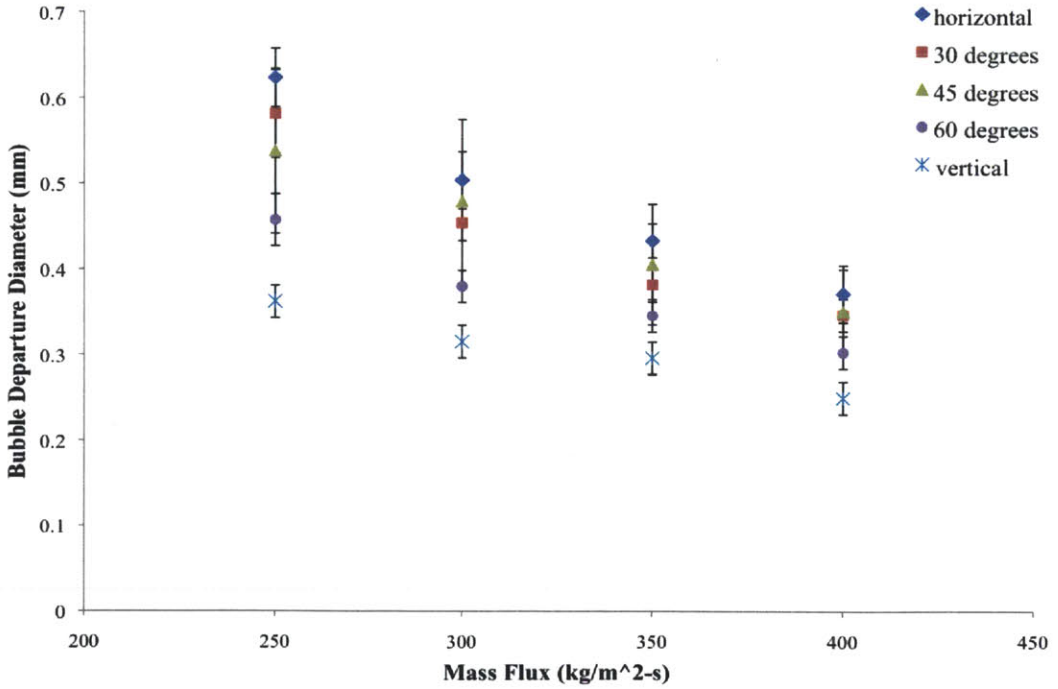

Figure 27: Bubble departure diameter as a function of mass flux for various orientation angles, 10°C subcooling and 0.05 MW/m^2 heat flux.

6.4 High Speed Video Visualization

6.4.1 Vertical Test Section

The images taken with the HSV were all captured at a frame rate of 5000 fps with an image size of 1280 x 800 pixels. All the bubbles imaged in this work are near-perfectly spherical. The bubble departure diameter is the diameter of the bubble measured at the instant (frame) in which the bubble detaches from the surface. The uncertainty on the diameter of a single bubble is one pixel or ± 0.019 mm, as measured with respect to a reference reticule. The bubble departure frequency was low enough that 5000 fps allowed for capture of the bubble departure for all test conditions.

Figures 28 through 31 show the effect of mass flux on a bubble detaching from a nucleation site off a vertical (90°) heater. It is apparent from these figures that as mass flux increases, bubble departure diameter decreases. The images in Figure 28 were taken from videos of a vertical heater, with a heat flux of 0.1 MW/m^2 and 10°C subcooling, while the images in Figure 29 were taken from videos with a heat flux of 0.05 MW/m^2 and 10°C subcooling. A comparison of these figures shows that as heat flux decreases, bubble departure diameter decreases as well. Figures 30 and 31 show the same effect of mass flux on bubble diameter but for 20°C subcooling, and heat flux values of 0.1 MW/m^2 and 0.05 MW/m^2, respectively. In comparison with the images in Figures 28 and 29, the bubble diameters are relatively smaller, which is anticipated given that bubble size should decrease as the amount of subcooling increases.

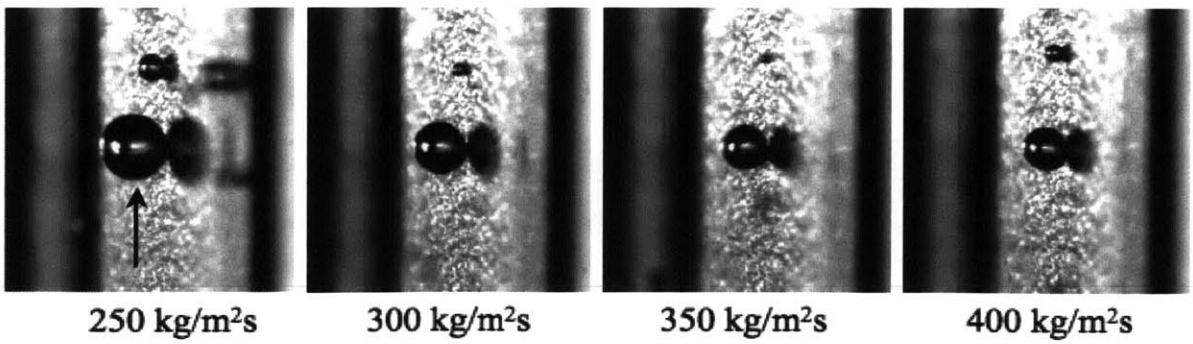

Figure 28: The effect of mass flux on a detaching bubble for 10°C subcooling and a heat flux of 0.1 MW/m^2. Mass flux increases from left to right.

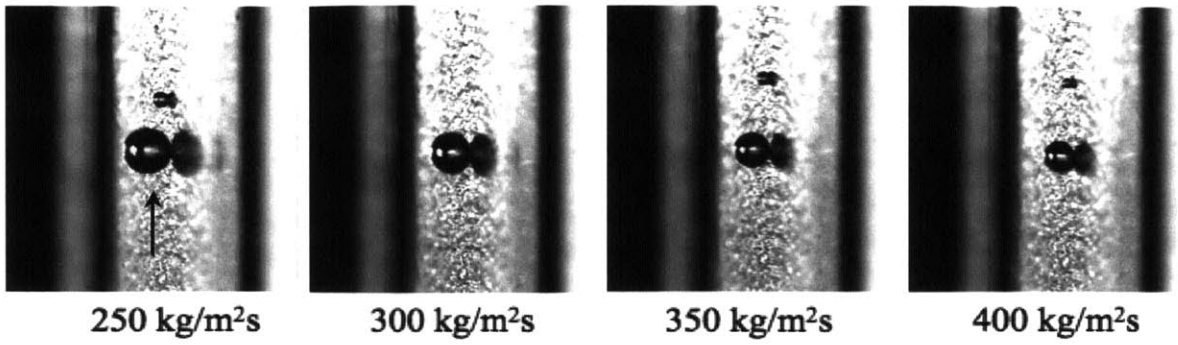

Figure 29: The effect of mass flux on a detaching bubble for 10°C subcooling and a heat flux of 0.05 MW/m^2. Mass flux increases from left to right.

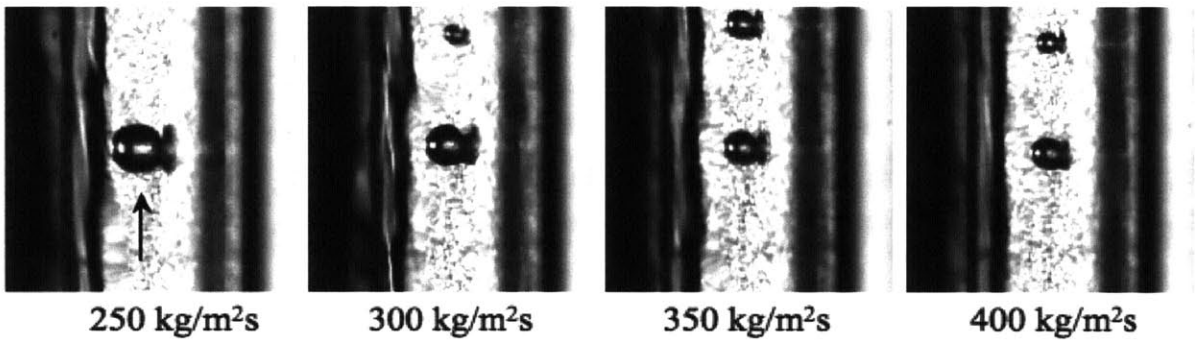

Figure 30: The effect of mass flux on a detaching bubble for 20°C subcooling and a heat flux of 0.1 MW/m^2. Mass flux increases from left to right.

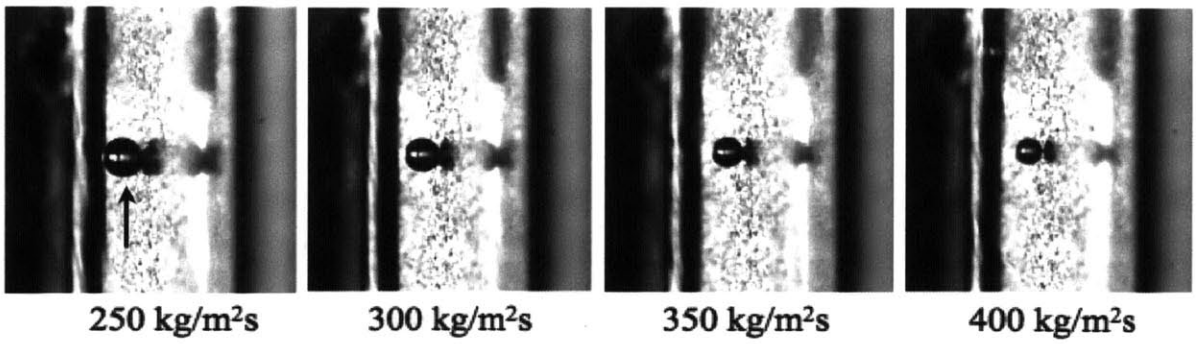

Figure 31: The effect of mass flux on a detaching bubble for 20°C subcooling and a heat flux of 0.05 MW/m^2. Mass flux increases from left to right.

6.4.2 Angled Test Section

Figures 32 and 33 display images of bubbles departing off a 60° heater in 20°C and 10°C subcooling, and 0.05 MW/m^2.

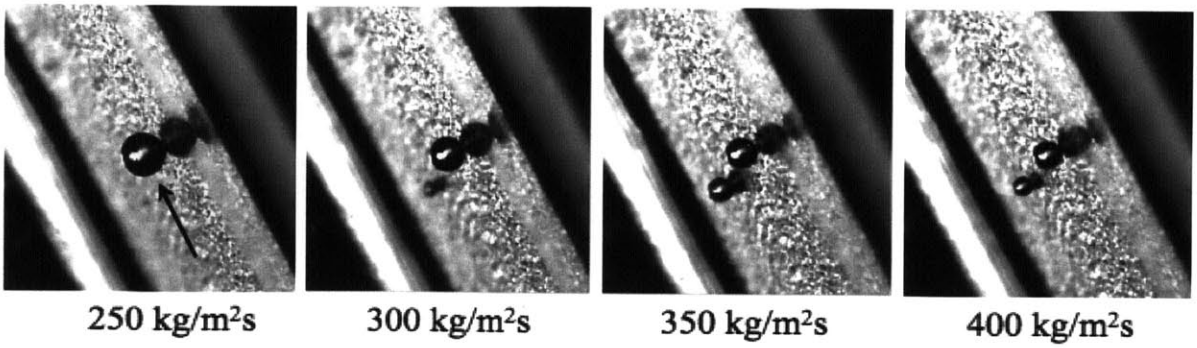

Figure 32: The effect of mass flux on a detaching bubble off a 60° heater for 20°C subcooling and a heat flux of 0.05 MW/m^2. Mass flux increases from left to right.

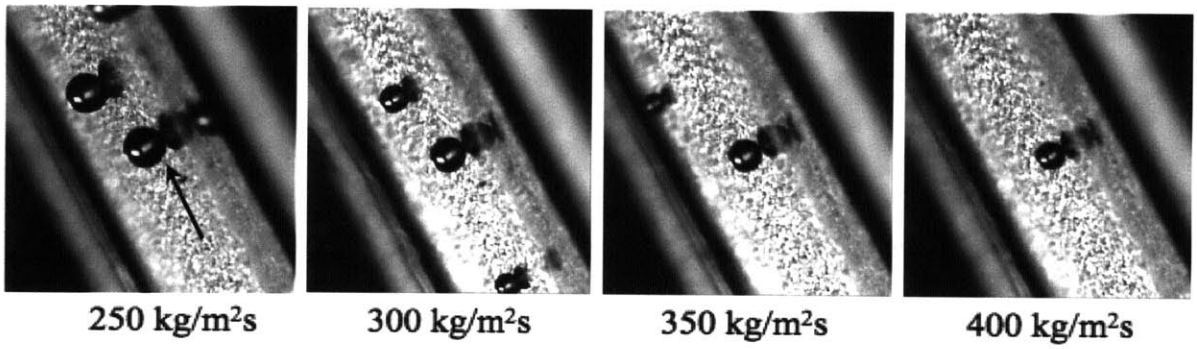

Figure 33: The effect of mass flux on a detaching bubble off a 60° heater for 10°C subcooling and a heat flux of 0.05 MW/m^2. Mass flux increases from left to right.

Figures 34 and 35 show a series of images of bubbles detaching from a 45° heater for various mass fluxes, 0.05 MW/m^2 heat flux, and 20°C and 10°C subcooling, respectively. As was seen in Figures 32 and 33 above, a comparison between the images in both of the figures below shows that the effect of subcooling is not very significant.

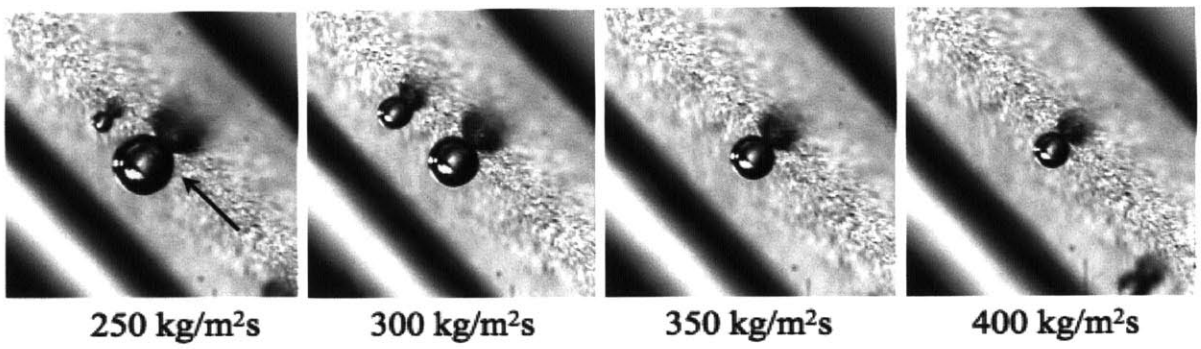

Figure 34: The effect of mass flux on a detaching bubble off a 45° heater for 20°C subcooling and a heat flux of 0.05 MW/m^2. Mass flux increases from left to right.

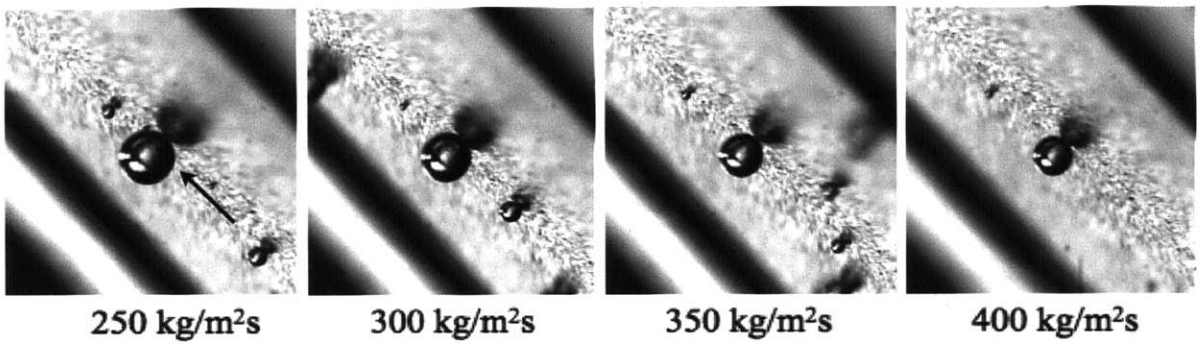

Figure 35: The effect of mass flux on a detaching bubble off a 45° heater for 10°C subcooling and a heat flux of 0.05 MW/m^2. Mass flux increases from left to right.

Series of bubbles departing from a single nucleation site off a 30° heater for various mass fluxes, 20°C subcooling, and 0.05 MW/m^2 and 0.1 MW/m^2 heat flux are shown in Figures 36 and 37, respectively. A comparison of the images in these figures indicates that the effect of heat flux does not appear to be very significant based on bubble departure size, but that an increase in heat flux results in a slight increase in bubble diameter.

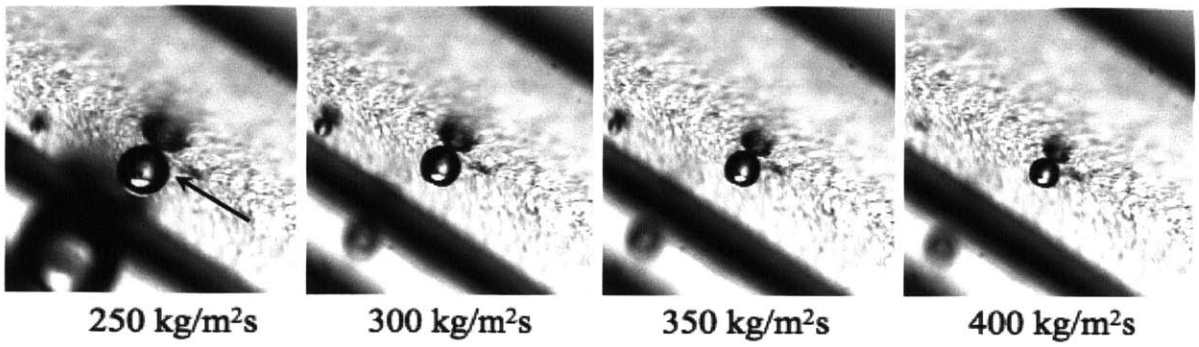

Figure 36: The effect of mass flux on a detaching bubble off a 30° heater for 20°C subcooling and a heat flux of 0.05 MW/m^2. Mass flux increases from left to right.

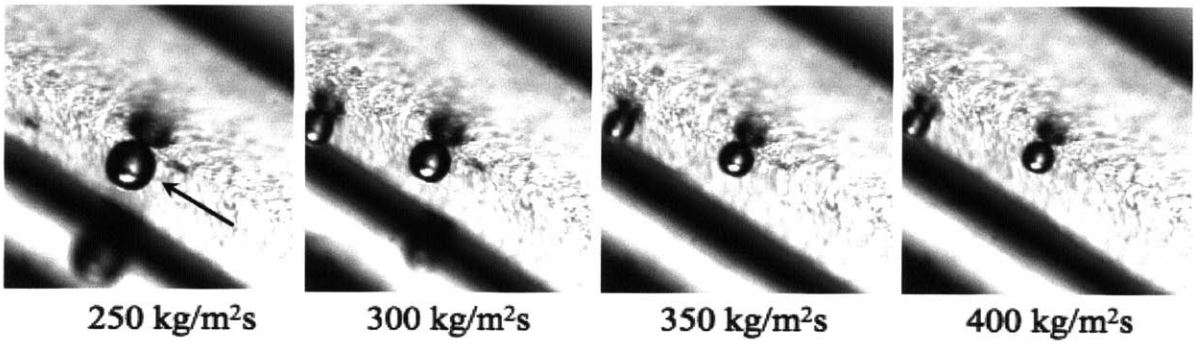

Figure 37: The effect of mass flux on a detaching bubble off a 30° heater for 20°C subcooling and a heat flux of 0.1 MW/m^2. Mass flux increases from left to right.

6.4.3 Horizontal Test Section

Figure 38 below shows a series of bubbles detaching from a downward-facing horizontal heater with 20°C subcooling, 0.05 MW/m^2 heat flux, and varying values of mass flux. Figure 39 illustrates the same series but for a heat flux of 0.1 MW/m^2. A comparison of these two figures indicates that increasing heat flux results in a slight, but not very significant, overall increase in bubble departure diameter.

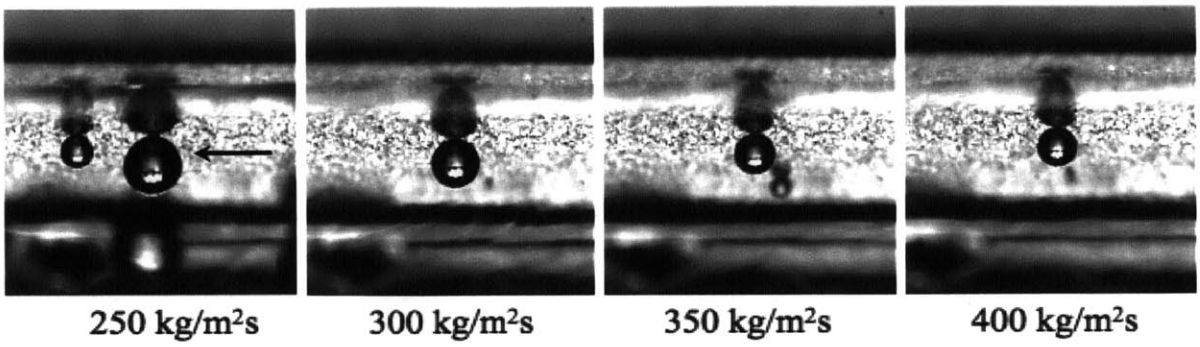

Figure 38: The effect of mass flux on a detaching bubble off a downward facing horizontal heater for 20°C subcooling and a heat flux of 0.05 MW/m^2. Mass flux increases from left to right.

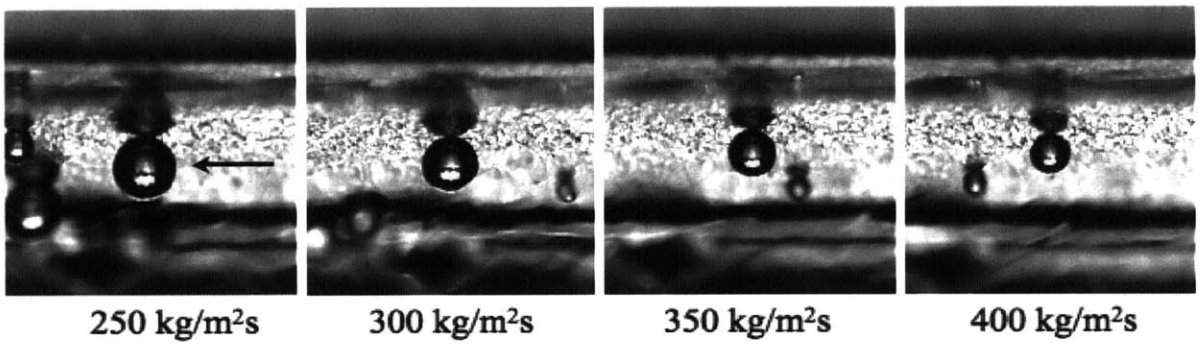

Figure 39: The effect of mass flux on a detaching bubble off a downward facing horizontal heater for 20°C subcooling and a heat flux of 0.1 MW/m^2. Mass flux increases from left to right.

Figures 40 and 41 show a series of bubbles detaching from the same nucleation site off a downward-facing horizontal heater with 10°C subcooling. The images in Figure 40 were taken with a heat flux of 0.05 MW/m^2, while those in Figure 41 were taken with a heat flux of 0.1 MW/m^2. A comparison of the two figures shows again that although the effect of heat flux is not very significant, increasing heat flux does increase the bubble departure diameter.

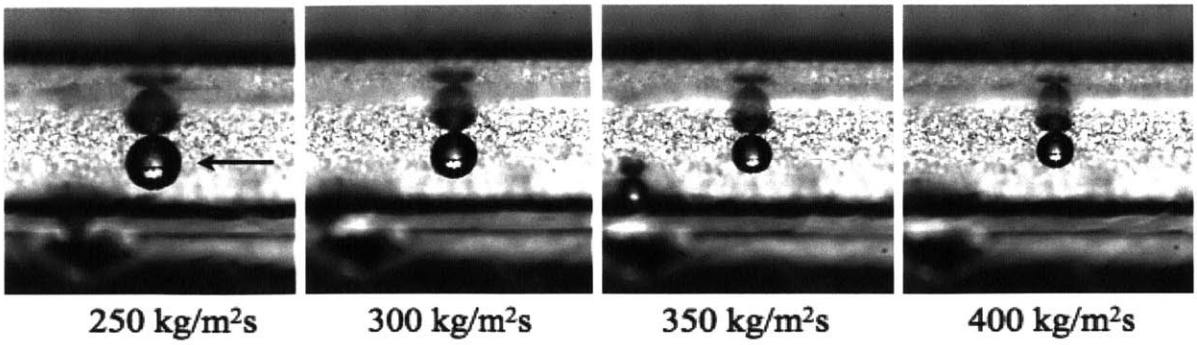

Figure 40: The effect of mass flux on a detaching bubble off a downward facing horizontal heater for 10°C subcooling and a heat flux of 0.05 MW/m^2. Mass flux increases from left to right.

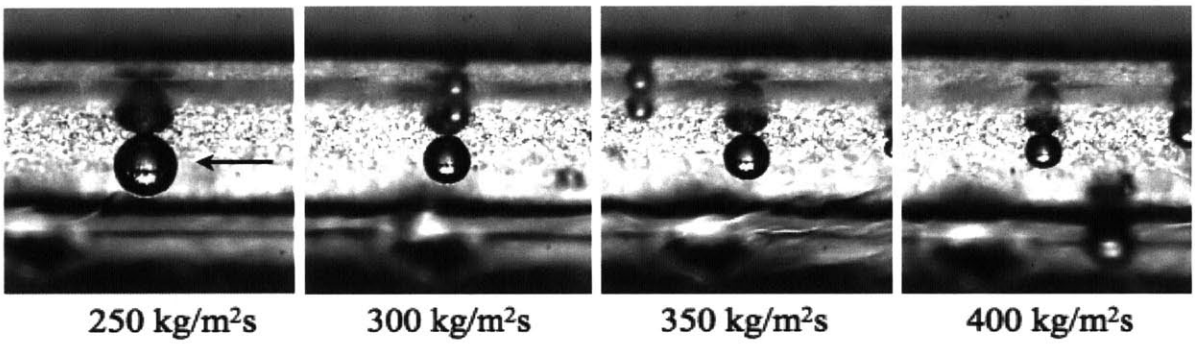

Figure 41: The effect of mass flux on a detaching bubble off a downward facing horizontal heater for 10°C subcooling and a heat flux of 0.1 MW/m^2. Mass flux increases from left to right.

7 Analysis

7.1 Summary of Results

The primary trends observed from this investigation followed the predictions from pre-existing models, specifically Klausner's original bubble departure model [5] and Yun's modified version of Klausner's model [20]. Notably, bubble departure diameter increased with decreasing mass flux, increasing heat flux, and, to a lesser extent, with increasing levels of subcooling. The model was also applied to elevated pressure conditions and various orientation angles to investigate the effect of these parameters on bubble departure. Klausner's research did not explicitly investigate these parameters but their effects can be predicted from his original model. Although the majority of the experimental runs were conducted at atmospheric pressure, additional tests run at elevated pressure with a horizontal test section did indicate that bubble departure diameter decreases with increased pressure. The effect of orientation angle was investigated by running the full test matrix, varying mass flux, heat flux, and levels of subcooling, at various inclinations of the test section (heater surface), specifically, at 0° (downward-facing horizontal), 30°, 45°, 60°, and 90° (vertical). Bubble departure diameter was observed to increase as orientation angle decreases. Thus, the largest bubbles departed off a downward-facing horizontal surface, whereas the smallest bubbles departed off a vertical surface with upflow conditions. These observations are qualitatively consistent with the predictions of Klausner's models.

The specific numerical predictions from Klausner's original model, applied to the experimental conditions in the present study, will be discussed in the following sections. Overall, this model significantly overpredicts bubble departure diameter. The most recent version of his model, with modifications by Yun et al., seems to decrease the gap between model predictions and actual experimental results. However, an accurate model that can be applied to a wide range of experimental conditions is still needed.

The specific behaviors and dependences of bubble departure diameter on various parameters can be elucidated by studying the individual forces in Klausner's Model.

7.2 Dominant Forces in Klausner's Model

Ultimately we wish to develop an accurate model for bubble departure diameter that can be applied to PWR fuel assembly conditions. The database we have generated in this thesis can be utilized to improve and further test the applicability of Klausner's model. However, the relevancy of such mechanistic models can only be established if the dominant forces are shown to be important in the context of a PWR core. Therefore, it is important to determine which forces from Klausner's Model are the most dominant in affecting bubble departure.

To assess the applicability of this model in the context of PWR core conditions, a Matlab script was written to iterate over time and bubble size in Klausner's model. As a starting point, the code was run for the same conditions as in Klausner's estimate, with liquid properties of R113. The specific parameters used in his setup are presented in Table 12.

Table 12: Klausner's experimental test matrix and parameters [5].

Parameter	**Units**	**Experiment Range**
Mass Flux:	[kg/m^{2}s]	112 - 287
Heat Flux:	[kW/m^2]	11 - 26
Saturated Temperature:	[°C]	55 - 71
Superheat:	[°C]	12 - 17
Measured Parameters		
d_w	[mm]	0.09
α	[radian]	$\pi/4$
β	[radian]	$\pi/5$
δ	[mm]	6.5
X	[*dimensionless*]	0.106
σ	[N/m]	0.0135
ρ_l	[kg/m^3]	1479
ρ_v	[kg/m^3]	10.7
ν_l	[m^2/s]	2.91E-7

The following values were found as predictions for the forces based on the specific experimental parameters used in Klausner's experimental validation of his model. In the x-direction, F_{sx} is

-9.9E-8 N, F_{qs} is 2.8E-7 N, and F_{dux} is -1.8E-7 N. In the y-direction, F_{sy} is -2.5E-6 N, F_{duy} is -1E-6 N, F_{sL} is 1.3E-6 N, F_b is 1E-7 N, F_{cp} is 1.7E-7 N, and F_h is 2.7E-7 N. These result in a sum of x-forces of 0 N and a sum of y-forces of -1.7E-6 N. A comparison between these results and those from the Matlab model is presented in Table 13.

Table 13: Comparison of forces for R113 bubbles as calculated by Klausner using his model and the Matlab tool developed for this analysis. Forces are all given in units of N.

Force:	**Klausner:**	**Matlab Model:**
F_{sx}:	-9.90E-08 N	-9.86E-08 N
F_{sy}:	-2.50E-06 N	-2.48E-06 N
F_{qs}:	2.80E-07 N	2.71E-07 N
F_{dux}:	-1.80E-07 N	-1.35E-07 N
F_{duy}:	-1.00E-06 N	-7.65E-07 N
F_{sL}:	1.30E-06 N	9.32E-07 N
F_b:	1.00E-07 N	1.32E-07 N
F_h:	2.70E-07 N	2.79E-07 N

Given that the difference between the force values as calculated by Klausner and by the Matlab tool is less than 25% for all forces, it is clear that this script can reproduce his results well and thus it will be used for the rest of the analysis. The slight variation that shows up is most likely due to the fact that the specific properties of refrigerant R113, which was used as the bulk fluid in Klausner's experiments, were not reported by Klausner.

In the context of Klausner's experimental conditions, with the assumption that the contact diameter (d_w) approaches zero at departure, the surface tension, hydrodynamic pressure, and contact pressure forces can be assumed to be negligible compared to the other forces in both x and y directions. The quasi-steady drag, growth, shear lift, and buoyancy forces are thus left as the most dominant ones in this specific case. This assumption will be further verified in the context of typical

PWR conditions and the conditions of the experiment in this study, and the dominant forces in each setup will be compared.

7.2.1 Klausner's Model Applied to PWR Conditions

As was previously mentioned, it is important to determine which forces are most dominant in affecting bubble departure in PWR core conditions. The following parameters in Table 14 are typical for a Westinghouse PWR 17x17 fuel assembly and will be used in the analysis of Klausner's model.

Table 14: Parameters for a typical Westinghouse PWR 17x17 Fuel Assembly [1].

Parameter	**Units**	**Value**
Reactor General Parameters		
Nominal Pressure:	[MPa]	15.51
Core Inlet Temperature:	[°C]	292.7
Core Exit Temperature:	[°C]	343
Core Coolant Mass Flux:	[kg/m^{2}s]	3,733
Active Core Equivalent Diameter:	[m]	3.37
Fuel Rods		
Fuel Rod Outside Diameter:	[mm]	9.5
Total Fuel Rod Height:	[m]	3.876
Heated Fuel Height:	[m]	3.658
Subchannel Flow Area:	[mm^2]	87.9
Pitch:	[mm]	12.6
Equivalent (hydraulic) Diameter:	[mm]	11.8
Channel-averaged Subcooled Liquid Properties		
C_{pl}	[kJ/kg°C]	6.5
μ_l	[Pa-s]	8.4x10^{-5}
k_l	[W/m°C]	0.51
Saturation Properties at 15.51 MPa and 344.7°C		
ρ_f	[kg/m^3]	593
ρ_g	[kg/m^3]	101
h_f	[kJ/kg]	1,631
h_g	[kJ/kg]	2,596
μ_f	[Pa-s]	7.3x10^{-5}
μ_g	[Pa-s]	2.3x10^{-5}
k_f	[W/m°C]	0.448
k_g	[W/m°C]	0.123
σ	[N/m]	0.0048

These parameters were included in the model to determine the values of each force and thus which forces dominate in a PWR setting, particularly when compared to the dominant forces with the experimental conditions. The specific values are presented in Table 15 below.

Table 15: Forces in Klausner's model that result using PWR conditions. Values are given in units of N.

Force:	**Value:**
F_{sx}:	-3.0863E-07
F_{sy}:	-8.1317E-07
F_{qs}:	3.8791E-08
F_{dux}:	-8.7652E-09
F_{duy}:	-4.9710E-08
F_{sL}:	2.0500E-07
F_b:	2.0175E-11
F_h:	7.8816E-06

Several approximations and assumptions were made to determine these force values, but given the known parameters and conditions that exist in a typical PWR, these approximations should be representative of the relative magnitudes for each force. The dominant forces in this context are the hydrodynamic pressure force, shear lift force, surface tension forces, and quasi-steady drag force. This suggests that the assumption of a negligible contact diameter (as compared with the bubble departure diameter) is not necessarily true for PWR conditions, so the surface tension and hydrodynamic pressure forces can not be neglected.

7.2.2 Klausner's Model Applied to Experimental Conditions

As was done for PWR core conditions, Klausner's model will now be applied to the experimental conditions in the present setup. The general parameters that exist in this experiment were applied to the Klausner model and varied for the range of values in the test matrix in order to determine the dominant forces and to do a general sensitivity analysis. Table 16 presents the basic experimental parameters which are used as inputs in the code.

Table 16: Parameters for the experimental setup.

Parameter	**Units**	**Value**
Advancing Contact Angle:	[degrees]	90.63
Receding Contact Angle:	[degrees]	8.03
Angle of Bubble Growth:	[radian]	$\pi/18$
Flow Area:	[m^2]	0.00028
Equivalent Diameter:	[m]	0.0167

The variables of interest to the test matrix are used as either direct or indirect input variables for the code. Specifically, mass flux is given and used to calculate the velocity based on the flow configuration in the test section; heat flux is directly related to the wall temperature, which is another input; subcooling is reflected through the saturation and bulk fluid temperatures (inputs); pressure is used to calculate the fluid properties of water from steam tables (density, viscosity, surface tension, etc.); and orientation angle is a direct input (and used to calculate specific x and y components of the individual force terms). This leaves two general equations - the sum of forces in x and y - with two unknowns - bubble departure size and time of departure. Table 17 shows the values for each of the force terms for a vertical (90°) heater at each subcooling, heat flux, and mass flux.

Table 17: Forces in Klausner's model applied to the specific experimental conditions in this study, for a downward-facing horizontal (0°) heater. Subcooling is given in °C, heat flux in MW/m^2, and forces in N.

ΔT_{sub}	q"	Force	250 kg/m^{2}s	300 kg/m^{2}s	350 kg/m^{2}s	400 kg/m^{2}s
20°	0.05	F_{sx}	-3.9030E-06	-3.9030E-06	-3.9030E-06	-3.9030E-06
		F_{sy}	-1.0283E-05	-1.0283E-05	-1.0283E-05	-1.0283E-05
		F_{qs}	3.6913E-07	4.9527E-07	6.2050E-07	7.3895E-07
		F_{dux}	-1.5232E-09	-1.5232E-09	-1.5232E-09	-1.5232E-09
		F_{duy}	-8.6383E-09	-8.6383E-09	-8.6383E-09	-8.6383E-09
		F_{sL}	2.4794E-06	3.4307E-06	4.3855E-06	5.2918E-06
		F_b	7.7988E-06	6.8379E-06	5.8593E-06	4.9196E-06
		F_h	1.8551E-08	3.4720E-08	5.8416E-08	9.0902E-08
	0.10	F_{sx}	-3.9030E-06	-3.9030E-06	-3.9030E-06	-3.9030E-06
		F_{sy}	-1.0283E-05	-1.0283E-05	-1.0283E-05	-1.0283E-05
		F_{qs}	3.7920E-07	5.0972E-07	6.3940E-07	7.6347E-07
		F_{dux}	-1.2334E-07	-1.2334E-07	-1.2333E-07	-1.2333E-07
		F_{duy}	-6.9948E-07	-6.9947E-07	-6.9945E-07	-6.9943E-07
		F_{sL}	2.5711E-06	3.5635E-06	4.5612E-06	5.5223E-06
		F_b	8.3953E-06	7.4043E-06	6.3710E-06	5.3915E-06
		F_h	1.8551E-08	3.4720E-08	5.8416E-08	9.0902E-08
10°	0.05	F_{sx}	-3.9030E-06	-3.9030E-06	-3.9030E-06	-3.9030E-06
		F_{sy}	-1.0283E-05	-1.0283E-05	-1.0283E-05	-1.0283E-05
		F_{qs}	3.6331E-07	4.8421E-07	6.0358E-07	7.1564E-07
		F_{dux}	-1.5263E-09	-1.5263E-09	-1.5263E-09	-1.5263E-09
		F_{duy}	-8.6559E-09	-8.6559E-09	-8.6559E-09	-8.6559E-09
		F_{sL}	2.5148E-06	3.4505E-06	4.3892E-06	5.2787E-06
		F_b	7.7587E-06	6.8012E-06	5.8428E-06	4.9196E-06
		F_h	2.2060E-08	4.0961E-08	6.8363E-08	1.0554E-07
	0.10	F_{sx}	-3.9030E-06	-3.9030E-06	-3.9030E-06	-3.9030E-06
		F_{sy}	-1.0283E-05	-1.0283E-05	-1.0283E-05	-1.0283E-05
		F_{qs}	3.7350E-07	4.9825E-07	6.2186E-07	7.3924E-07
		F_{dux}	-1.2359E-07	-1.2359E-07	-1.2358E-07	-1.2358E-07
		F_{duy}	-7.0091E-07	-7.0089E-07	-7.0088E-07	-7.0086E-07
		F_{sL}	2.6085E-06	3.5816E-06	4.5635E-06	5.5084E-06
		F_b	8.3742E-06	7.3656E-06	6.3535E-06	5.3915E-06
		F_h	2.2060E-08	4.0961E-08	6.8363E-08	1.0554E-07

Based on the relative magnitude of these forces for the various heat fluxes, mass fluxes, and levels of subcooling, the dominant forces for the present experimental setup appear to be the shear lift, buoyancy, quasi-steady drag force, and surface tension forces.

The dominant forces under these experimental conditions are similar to the forces that were found to be most dominant in a PWR context, with the exception of the hydrodynamic pressure force which plays a greater role in the PWR core than in the experimental loop. Therefore, this experimental setup, with a vertical test section, is a relatively good representation of the forces that determine bubble formation and detachment in a PWR core.

7.3 Comparison of Results with Klausner's Bubble Departure Model

General trends have been noted based purely on the experimental data for bubble departure diameter with respect to various parameters, such as mass flux, heat flux, subcooling, pressure, and orientation angle. These trends can be further supported by the physical phenomena that are present in Klausner's original bubble departure model.

As mentioned before, a Matlab script was written in order to iterate Klausner's model and to apply it to different conditions, in particular, the conditions of this experiment. The following figures graphically show comparisons between the predictions from Klausner's model and the experimental results observed in the present study with respect to orientation angle. For all graphs, the model's predictions are presented in blue diamonds while the experimental data is shown in red squares. Figures 42, 43, 44, and 45 show results from 20°C subcooling and 0.10 MW/m^2 heat flux, at atmospheric pressure, for 250, 300, 350, and 400 kg/m^{2}s mass flux, respectively.

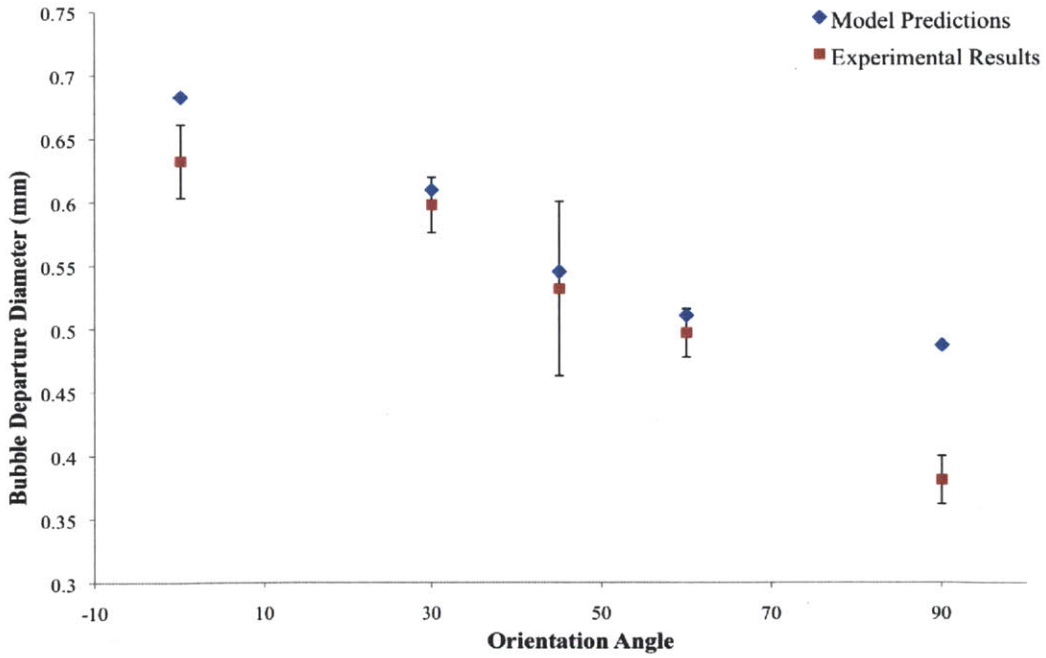

Figure 42: Comparison between Klausner's model predictions and experimental data for bubble departure diameter as a function of orientation angle; 20°C subcooling, 0.10 MW/m^2 heat flux, and 250 kg/m^{2}s mass flux, at atmospheric pressure.

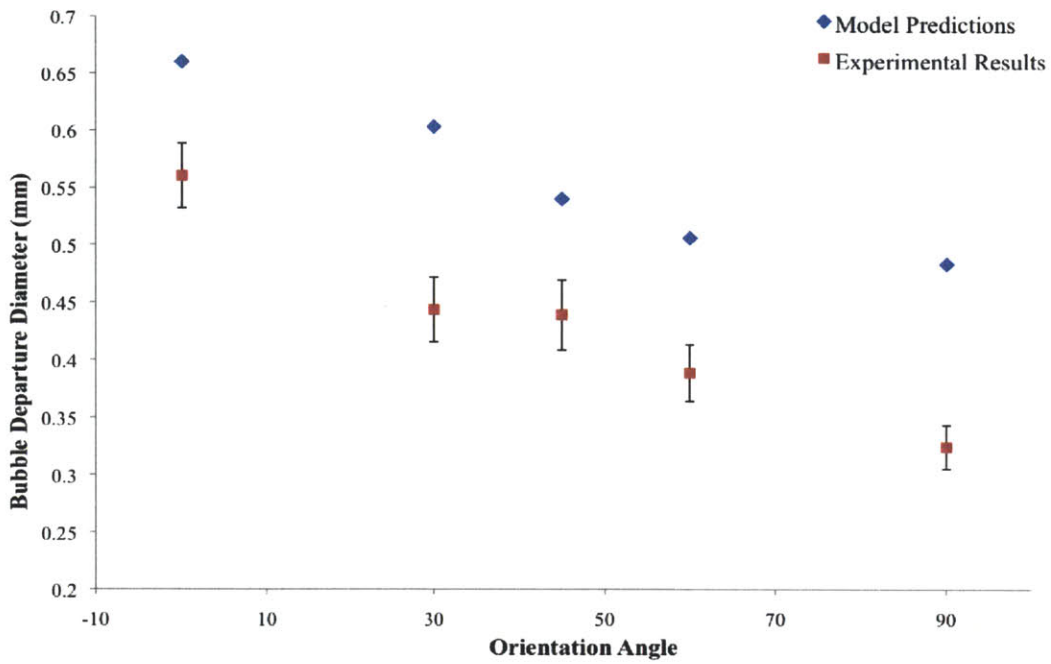

Figure 43: Comparison between Klausner's model predictions and experimental data for bubble departure diameter as a function of orientation angle; 20°C subcooling, 0.10 MW/m^2 heat flux, and 300 kg/m^{2}s mass flux, at atmospheric pressure.

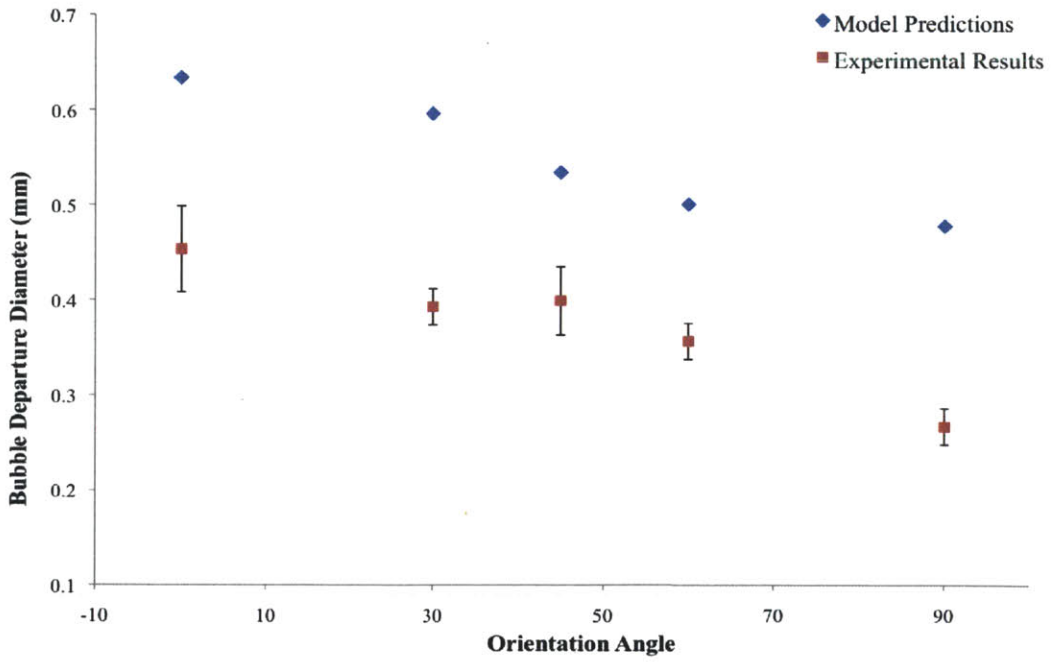

Figure 44: Comparison between Klausner's model predictions and experimental data for bubble departure diameter as a function of orientation angle; 20°C subcooling, 0.10 MW/m^2 heat flux, and 350 kg/m^{2}s mass flux, at atmospheric pressure.

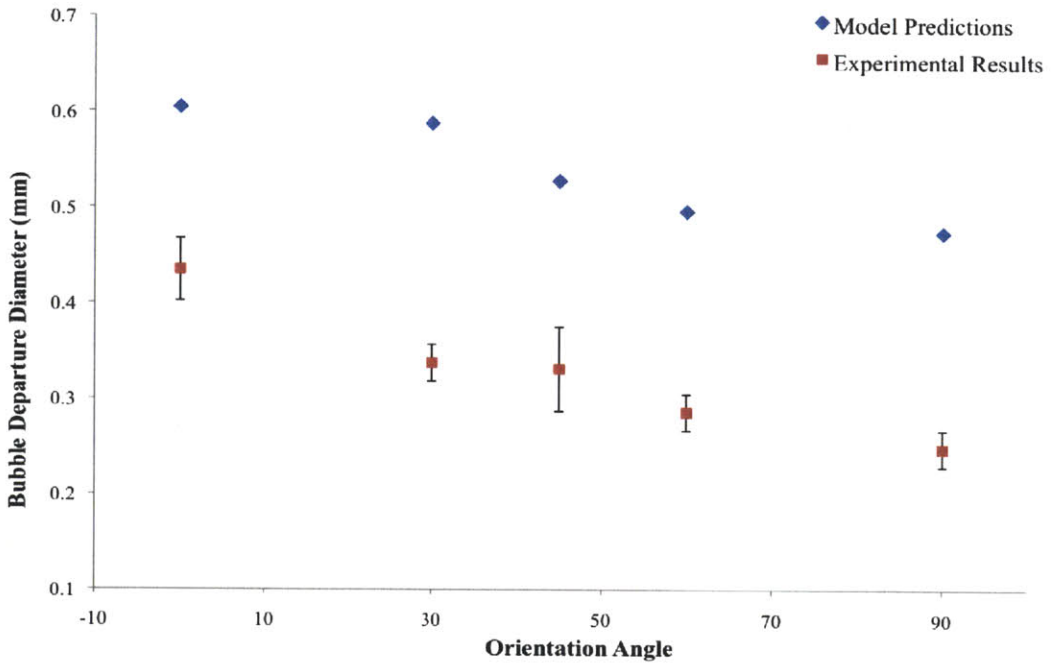

Figure 45: Comparison between Klausner's model predictions and experimental data for bubble departure diameter as a function of orientation angle; 20°C subcooling, 0.10 MW/m^2 heat flux, and 400 kg/m^{2}s mass flux, at atmospheric pressure.

For atmospheric pressure with 20°C subcooling and a heat flux of 0.10 MW/m^2, the model seems to predict the overall bubble departure trends relatively well and is generally consistent with the experimental data. The difference between the predictions and experimental data does increase as mass flux increases, which suggests that the model overpredicts bubble size for large mass fluxes and is more accurate for lower values.

To further investigate this observation, the following figures show the experimental data compared to the predictions from Klausner's model with respect to mass flux for a downward-facing (0°) heater.

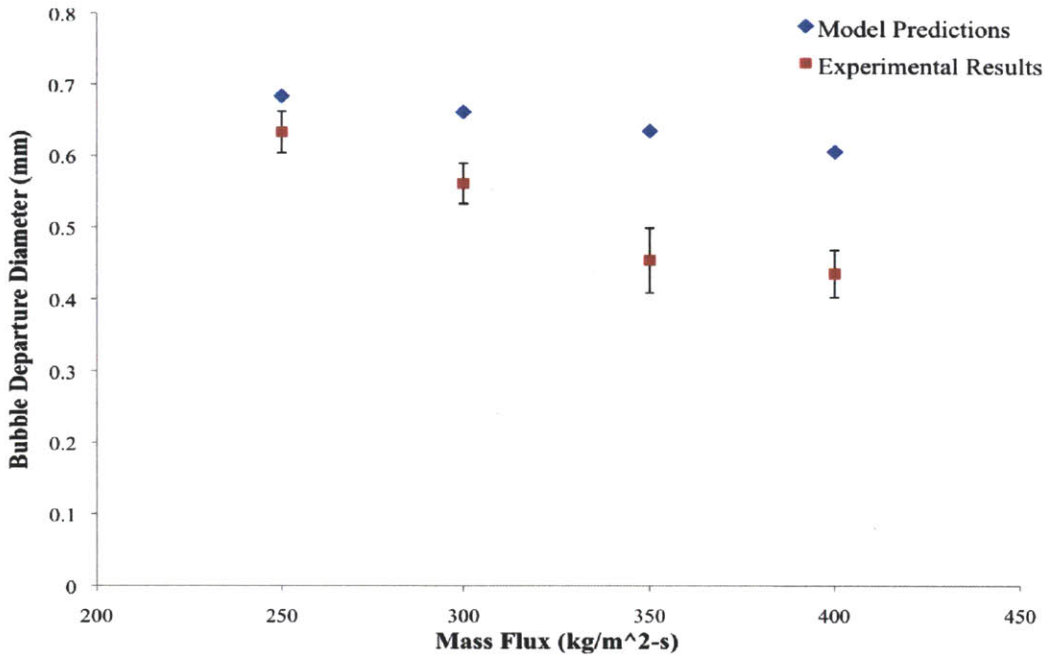

Figure 46: Comparison between Klausner's model predictions and experimental data for bubble departure diameter as a function of mass flux off a downward-facing (0°) heater; 20°C subcooling, 0.10 MW/m^2 heat flux, at atmospheric pressure.

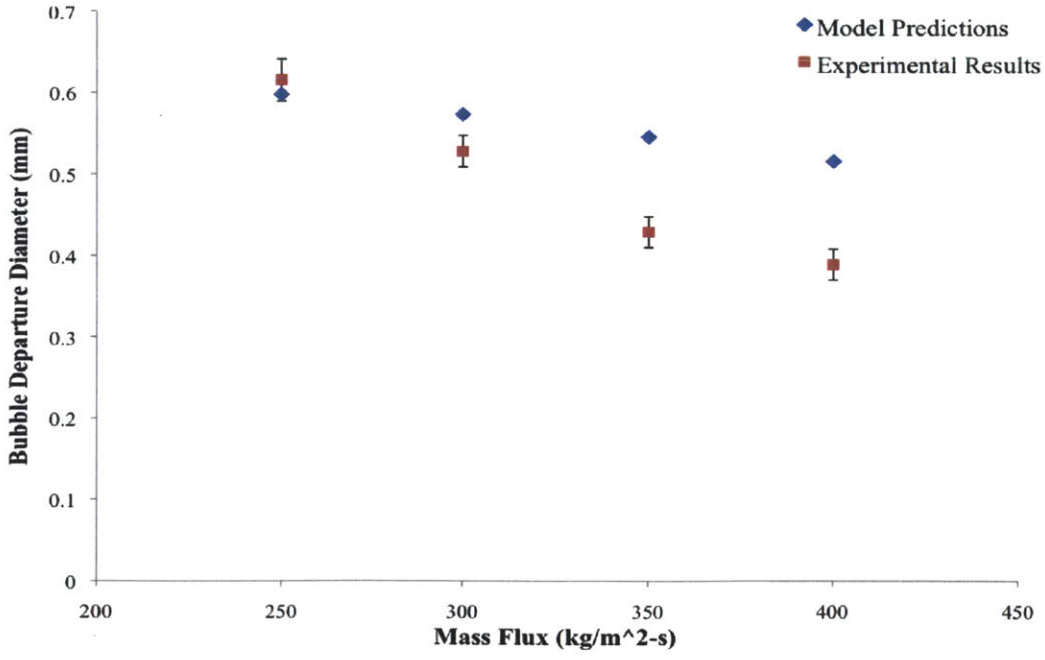

Figure 47: Comparison between Klausner's model predictions and experimental data for bubble departure diameter as a function of mass flux off a downward-facing (0°) heater; 20°C subcooling, 0.05 MW/m^2 heat flux, at atmospheric pressure.

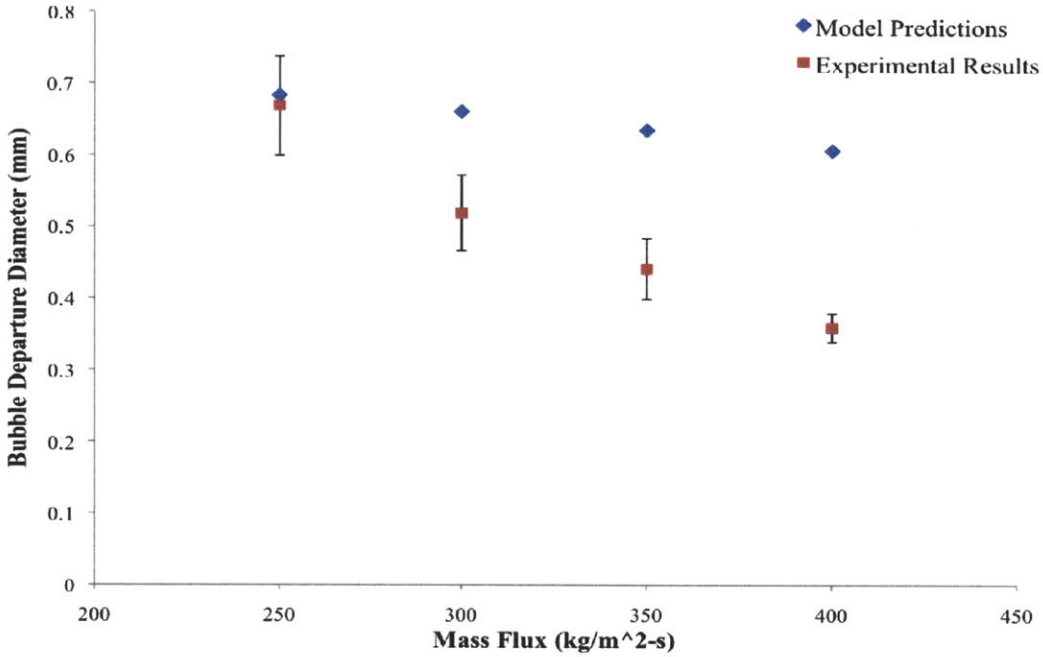

Figure 48: Comparison between Klausner's model predictions and experimental data for bubble departure diameter as a function of mass flux off a downward-facing (0°) heater; 10°C subcooling, 0.10 MW/m^2 heat flux, at atmospheric pressure.

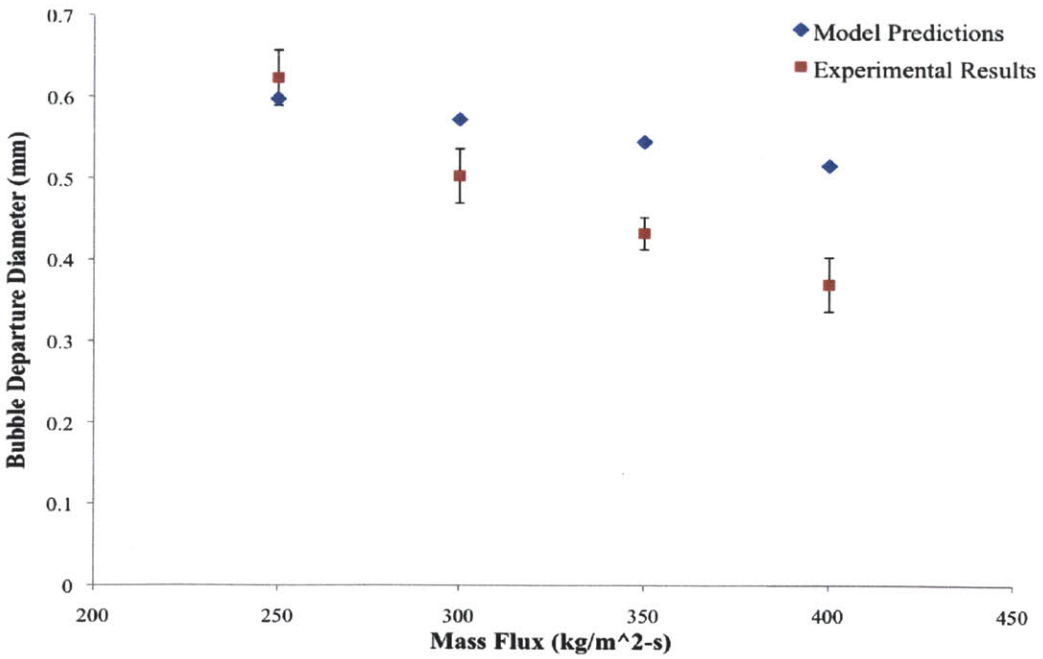

Figure 49: Comparison between Klausner's model predictions and experimental data for bubble departure diameter as a function of mass flux off a downward-facing (0°) heater; 10°C subcooling, 0.05 MW/m^2 heat flux, at atmospheric pressure.

It becomes clear from these figures that the model better predicts bubble departure diameter for values of mass flux. In the model, mass flux is accounted for through velocity, in the equation for uniform flow velocity, which assumes a turbulent single-phase flow relation. This uniform flow velocity is then used in Reynolds number calculations and in most of the individual force calculations.

The forces that are most sensitive to changes in mass flux are the quasi-steady drag, shear lift, buoyancy, and hydrodynamic pressure forces. A sensitivity analysis was performed and it was determined that the hydrodynamic pressure force is the most sensitive to changes in mass flux, followed by the shear lift force, then the quasi-steady drag, and finally the buoyancy force, which is affected by changes in mass flux, but not significantly. The specific percent increases (or decreases, for the buoyancy force) are shown in Table 18 below, and the behaviors for each of these forces with respect to mass flux are shown in Figures 50, 51, 52, and 53.

Table 18: Sensitivity analysis of mass flux [kg/m^{2}s] on the forces in Klausner's model. The values presented for each force are the percentage increase for each change in mass flux. Subcooling is given in °C and heat flux in MW/m^2.

ΔT_{sub}:	q":	Change in G:	F_{qs}	F_{sL}	F_b	F_h
20°	0.05	250 - 300	43.79%	52.71%	-7.41%	102.37%
		300 - 350	33.10%	38.65%	-9.25%	79.66%
		350 - 400	25.92%	29.64%	-10.52%	64.58%
	0.10	250 - 300	43.83%	52.54%	-7.24%	102.37%
		300 - 350	33.17%	38.61%	-9.04%	79.66%
		350 - 400	26.01%	29.68%	-10.27%	64.58%
10°	0.05	250 - 300	42.49%	50.42%	-7.66%	100.71%
		300 - 350	32.10%	37.11%	-9.29%	78.08%
		350 - 400	24.92%	28.28%	-10.80%	63.10%
	0.10	250 - 300	42.54%	50.29%	-7.49%	100.71%
		300 - 350	32.18%	37.09%	-9.08%	78.08%
		350 - 400	25.14%	28.50%	-10.31%	63.10%

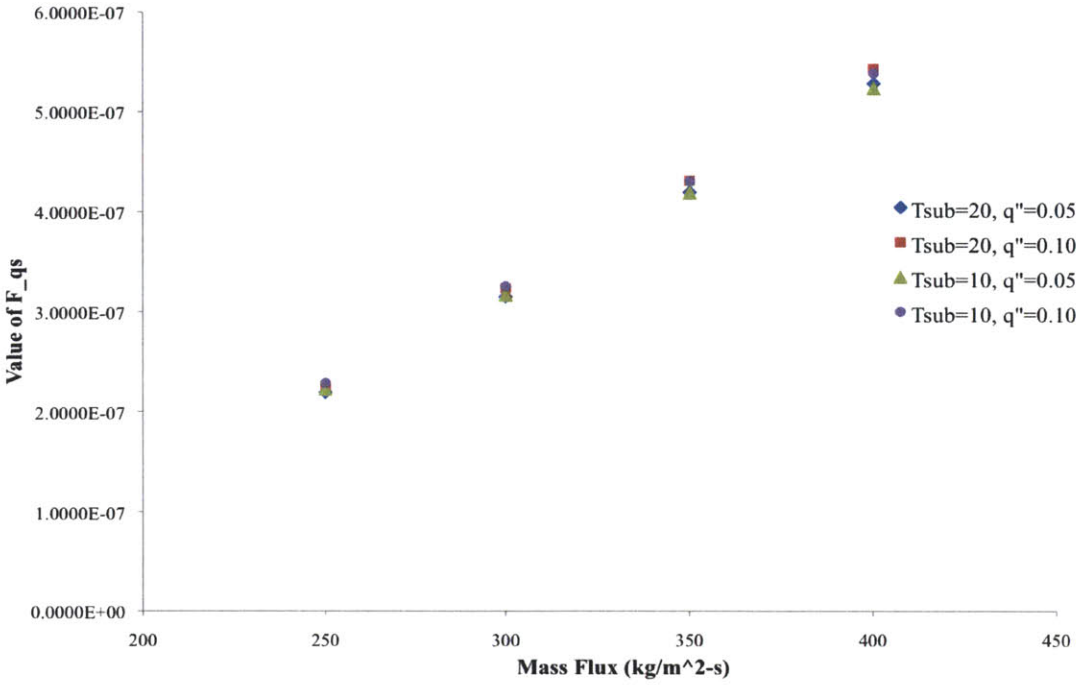

Figure 50: The effect of mass flux on the quasi-steady drag force, F_{qs}, for various levels of subcooling and values of heat flux. Note: subcooling is in units of °C and heat flux is in units of MW/m^2.

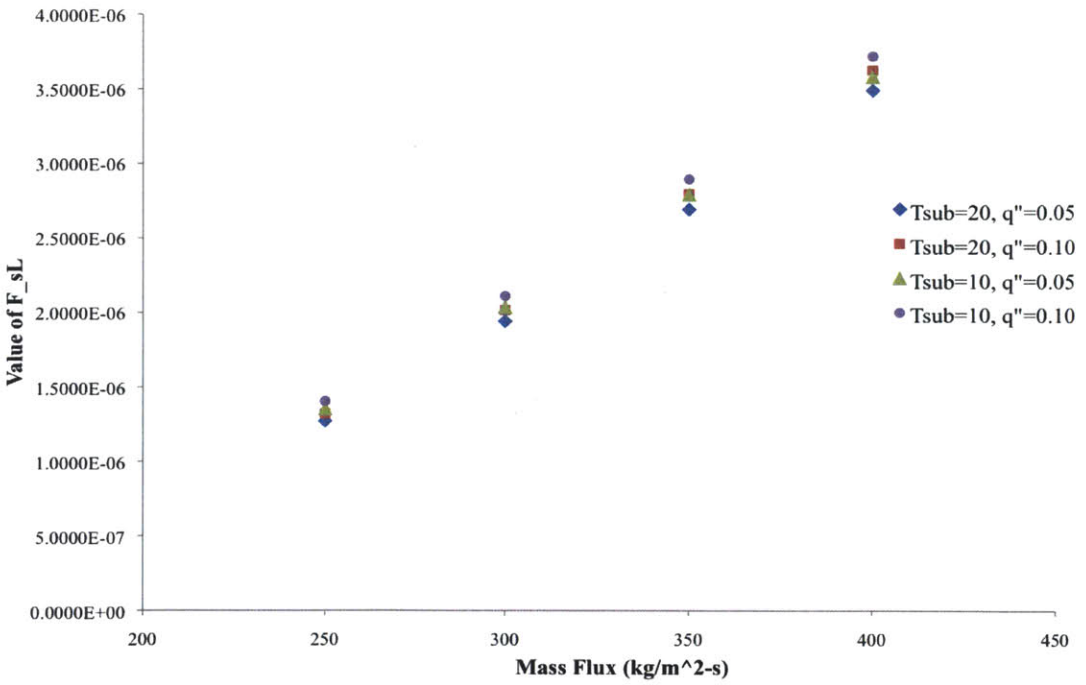

Figure 51: The effect of mass flux on the shear lift force, F_{sL}, for various levels of subcooling and values of heat flux. Note: subcooling is in units of °C and heat flux is in units of MW/m^2.

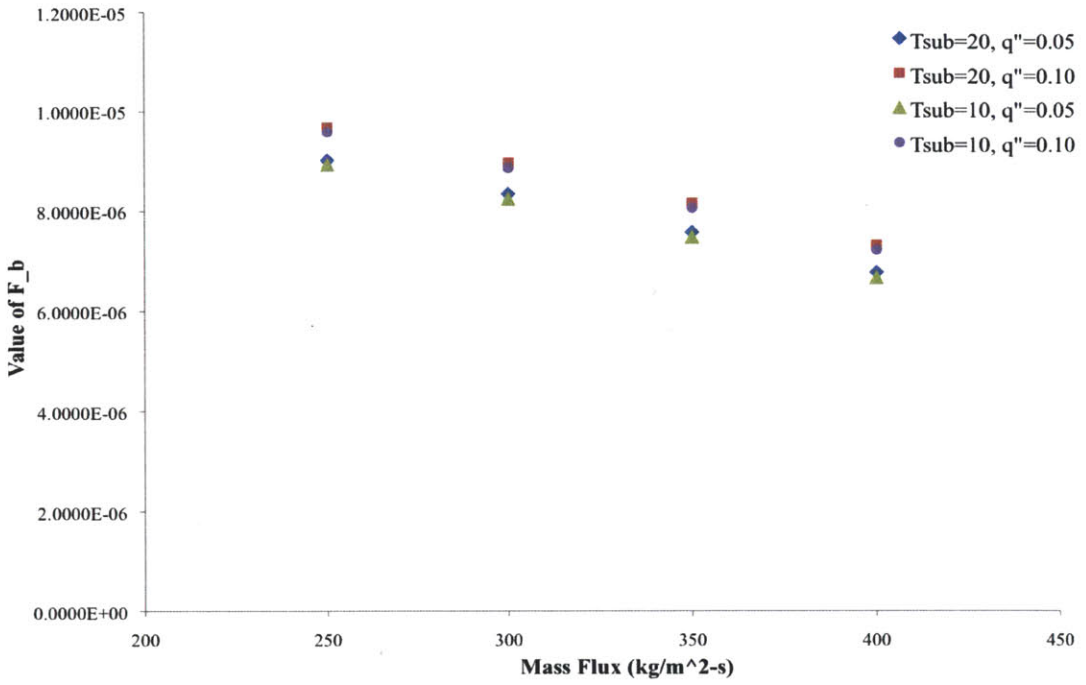

Figure 52: The effect of mass flux on the buoyancy force, F_b, for various levels of subcooling and values of heat flux. Note: subcooling is in units of °C and heat flux is in units of MW/m^2.

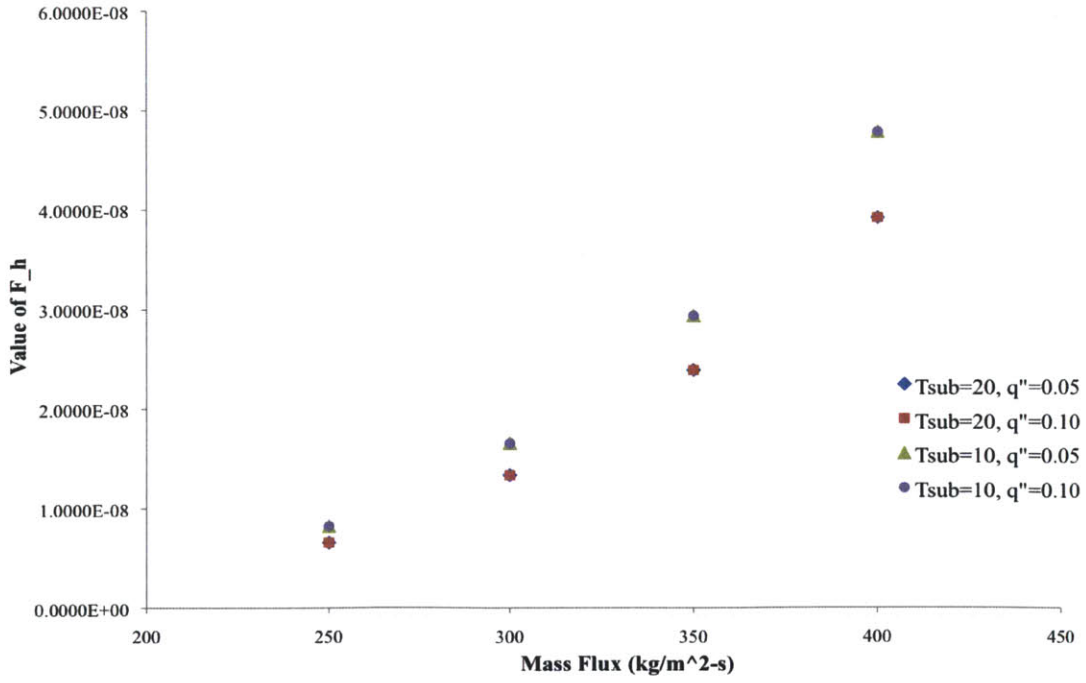

Figure 53: The effect of mass flux on the hydrodynamic pressure force, F_h for various levels of subcooling and values of heat flux. Note: subcooling is in units of °C and heat flux is in units of MW/m^2.

As can be seen in these figures, the quasi-steady growth, shear lift, and hydrodynamic pressure forces all become more dominant as mass flux increases. The buoyancy force, on the other hand, decreases in magnitude, becoming less dominant, as mass flux increases. Further, it is apparent that the hydrodynamic pressure force is the most sensitive to changes in mass flux.

Next, the results for a lower heat flux will be looked at. Figures 54, 55, 56, and 57 below show the same comparisons between experimental data and the model's predictions for 20°C subcooling and 0.05 MW/m^2 heat flux, at atmospheric pressure, for 250, 300, 350, and 400 kg/m^{2}s mass flux, respectively.

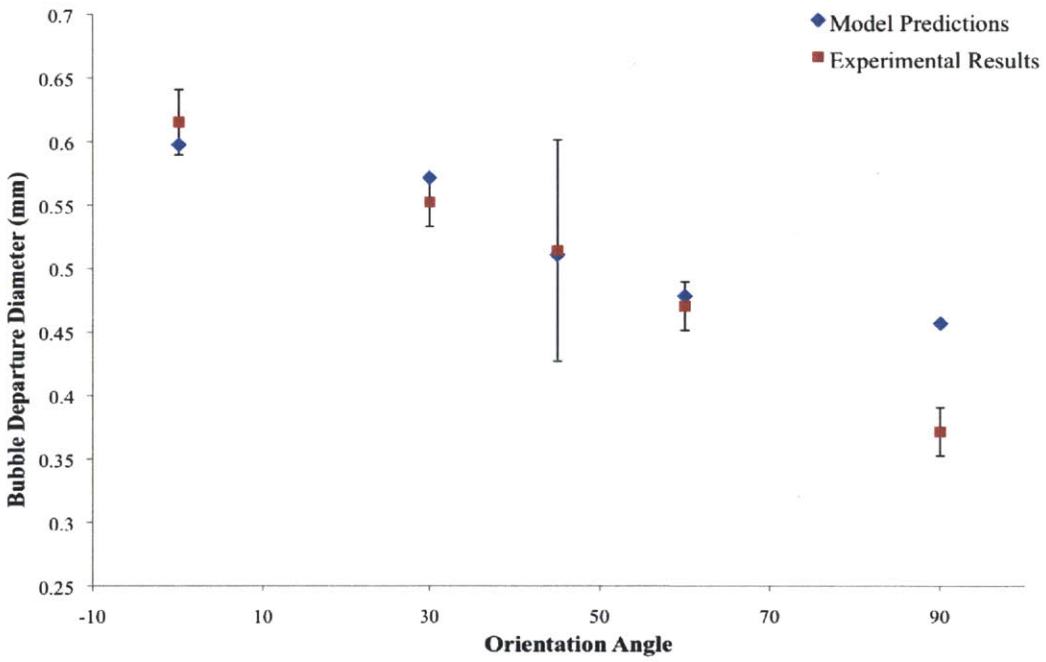

Figure 54: Comparison between Klausner's model predictions and experimental data for bubble departure diameter as a function of orientation angle; 20°C subcooling, 0.05 MW/m^2 heat flux, and 250 kg/m^{2}s mass flux, at atmospheric pressure.

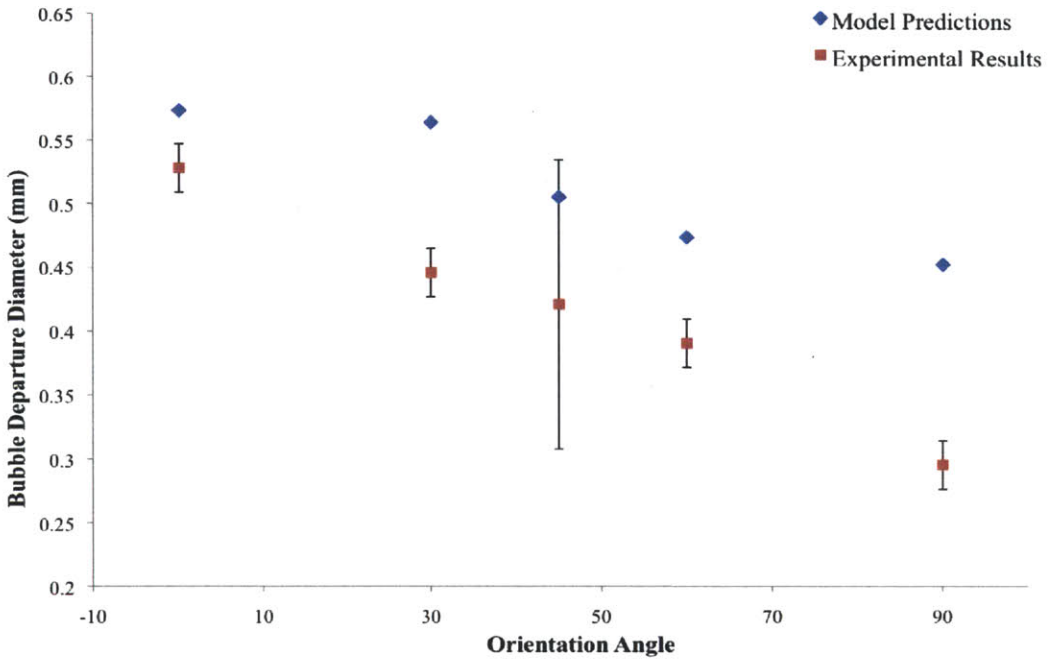

Figure 55: Comparison between Klausner's model predictions and experimental data for bubble departure diameter as a function of orientation angle; 20°C subcooling, 0.05 MW/m^2 heat flux, and 300 kg/m^{2}s mass flux, at atmospheric pressure.

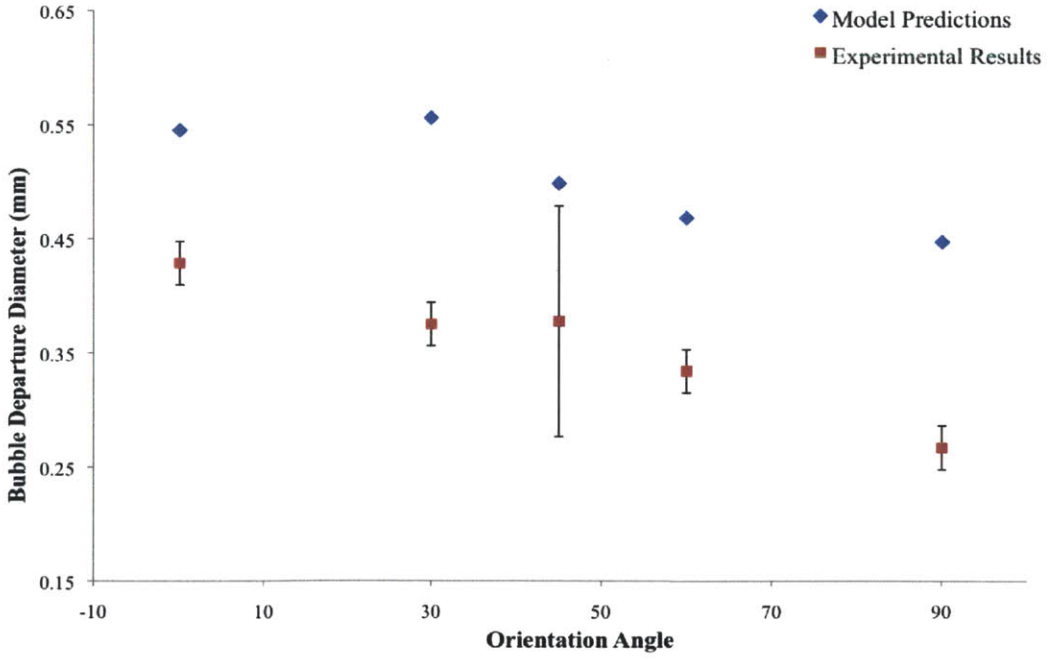

Figure 56: Comparison between Klausner's model predictions and experimental data for bubble departure diameter as a function of orientation angle; 20°C subcooling, 0.05 MW/m^2 heat flux, and 350 kg/m^{2}s mass flux, at atmospheric pressure.

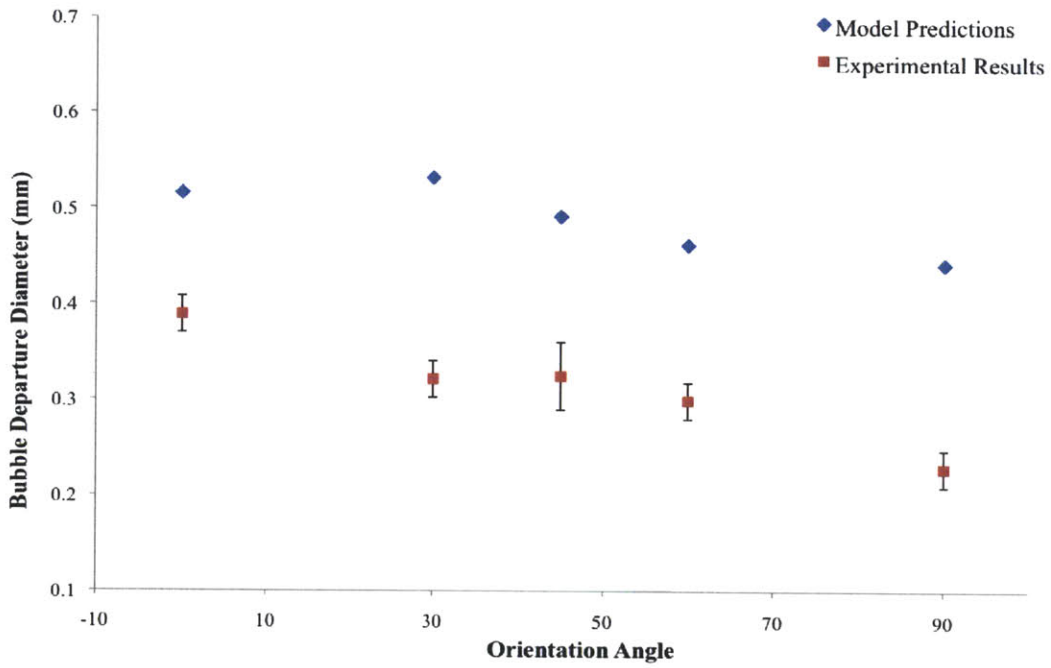

Figure 57: Comparison between Klausner's model predictions and experimental data for bubble departure diameter as a function of orientation angle; 20°C subcooling, 0.05 MW/m^2 heat flux, and 400 kg/m^{2}s mass flux, at atmospheric pressure.

Similar to Figures 42, 43, 44, and 45 for a heat flux of 0.1 MW/m^2, the experimental data in Figures 54, 55, 56, and 57 for a lower heat flux of 0.05 MW/m^2 follow the same general trends as those from the model's predictions. Again, the difference between the experimental data and predictions seems to increase for larger values of mass flux.

A general comparison between these two sets of graphs (those for a heat flux of 0.1 MW/m^2, and those for a heat flux of 0.05 MW/m^2) elucidates the impact of heat flux on bubble departure. Specifically, increasing heat flux results in larger bubble departure diameters. This makes sense because heat flux directly impacts the wall temperature (heater, in this case), and thus the wall superheat. As the heat flux increases, the wall temperature continues to rise above the saturation temperature. From a modeling perspective, this increase shows up in the Jakob number, which is an indication of the sensible heat available in the superheated liquid to support the growth of a bubble. Thus, as the liquid superheat is higher, the bubble grows faster and departs with a larger diameter.

The forces that are affected by changes in heat flux are the quasi-steady drag, growth, shear lift, and buoyancy forces. A sensitivity analysis was performed on each of these forces to determine the relative changes.

Table 19: Sensitivity analysis of heat flux [MW/m^2] on the forces in Klausner's model. The values presented for each force are the percentage increase for each change in heat flux. Subcooling is given in °C and mass flux in kg/m^{2}s.

Change in q":	**ΔT_{sub}:**	**G:**	**F_{qs}**	**F_{dux}**	**F_{duy}**	**F_{sL}**	**F_b**
0.05 - 0.10	20°	400	2.82%	98.76%	98.76%	3.84%	8.02%
		350	2.74%	98.76%	98.76%	3.81%	7.72%
		300	2.68%	98.76%	98.76%	3.84%	7.47%
		250	2.65%	98.76%	98.76%	3.95%	7.28%
	10°	400	2.91%	98.76%	98.76%	3.88%	8.35%
		350	2.73%	98.76%	98.76%	3.70%	7.76%
		300	2.67%	98.76%	98.76%	3.71%	7.50%
		250	2.64%	98.76%	98.76%	3.80%	7.30%

As heat flux increases from 0.05 to 0.10 MW/m^2, it appears that the x and y components of the unsteady growth force are by far the most sensitive to heat flux. Changes in the quasi-steady drag, shear lift, and buoyancy forces are all insignificant compared to those in the growth forces.

Next, for the same heat flux of 0.05 MW/m^2, the amount of subcooling is lowered to 10°C. As alluded to before, the effect of subcooling should not be substantial, especially compared to the effects of mass flux and heat flux. This will be discussed after Figures 58, 59, 60, and 61, consistent with Figures 54, 55, 56, and 57 discussed previously, which show comparisons between the model's predictions and experimental data for 250, 300, 350, and 400 kg/m^{2}s, respectively, but for conditions of 10°C subcooling, 0.05 MW/m^2, and atmospheric pressure.

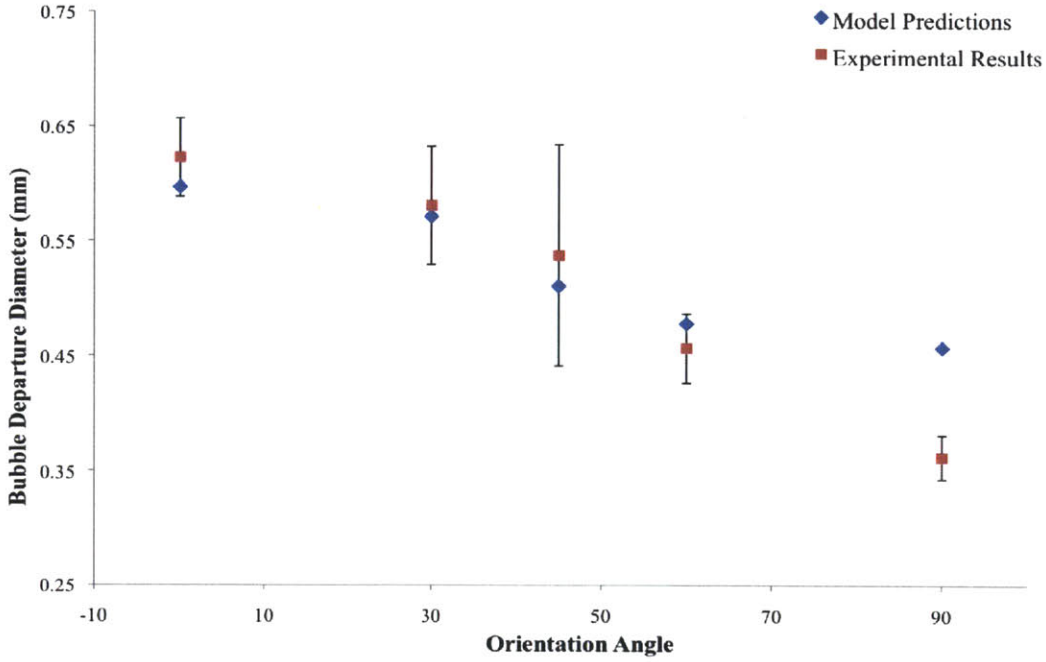

Figure 58: Comparison between Klausner's model predictions and experimental data for bubble departure diameter as a function of orientation angle; 10°C subcooling, 0.05 MW/m^2 heat flux, and 250 kg/m^{2}s mass flux, at atmospheric pressure.

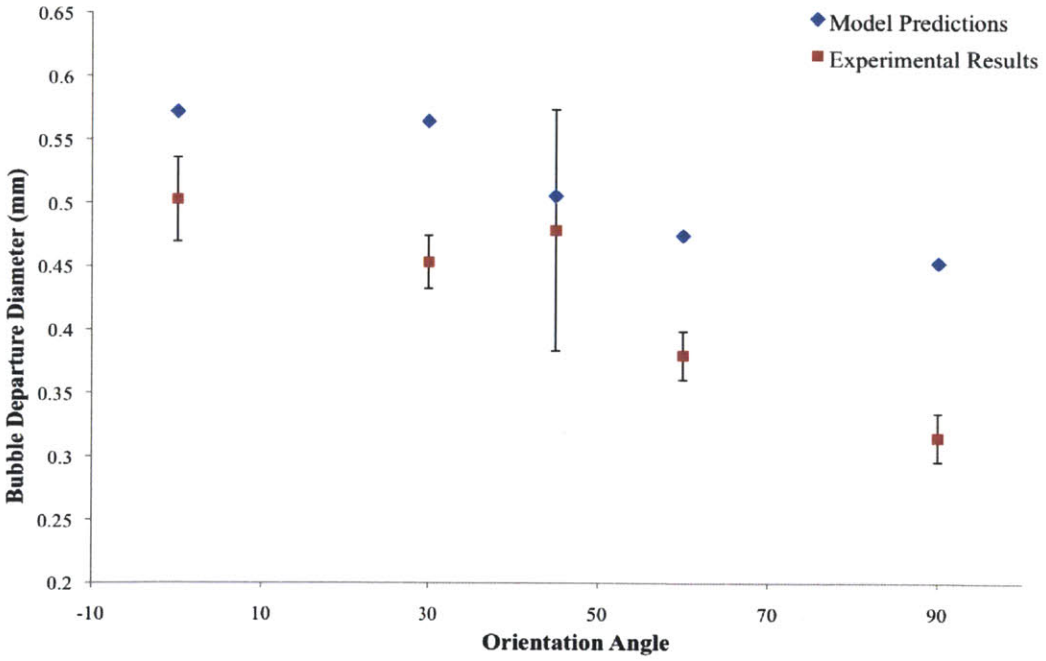

Figure 59: Comparison between Klausner's model predictions and experimental data for bubble departure diameter as a function of orientation angle; 10°C subcooling, 0.05 MW/m^2 heat flux, and 300 kg/m^{2}s mass flux, at atmospheric pressure.

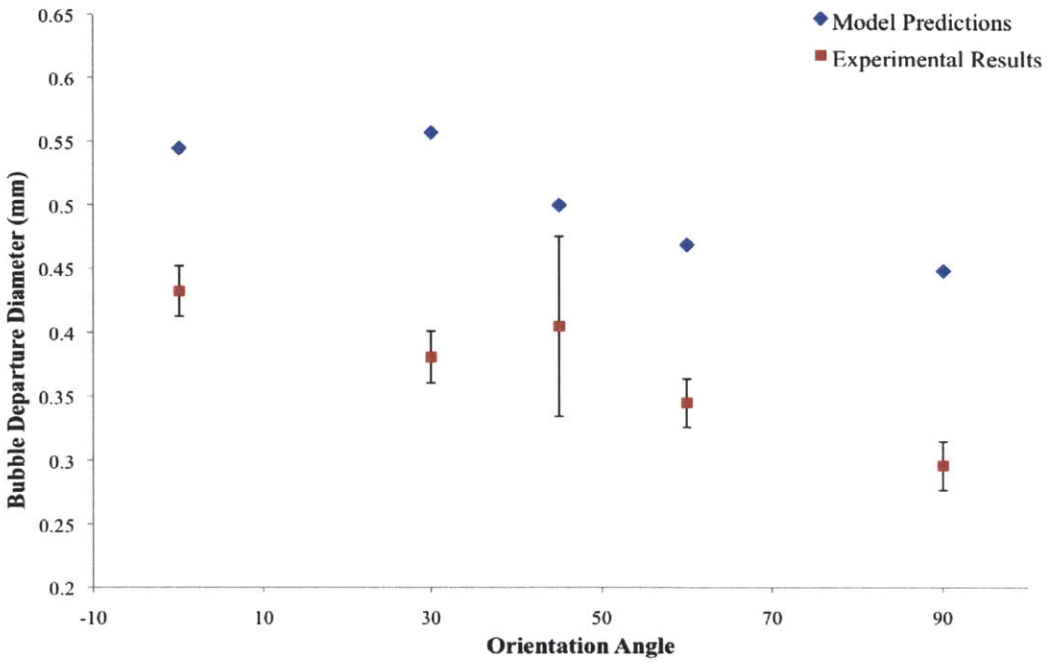

Figure 60: Comparison between Klausner's model predictions and experimental data for bubble departure diameter as a function of orientation angle; 10°C subcooling, 0.05 MW/m^2 heat flux, and 350 kg/m^{2}s mass flux, at atmospheric pressure.

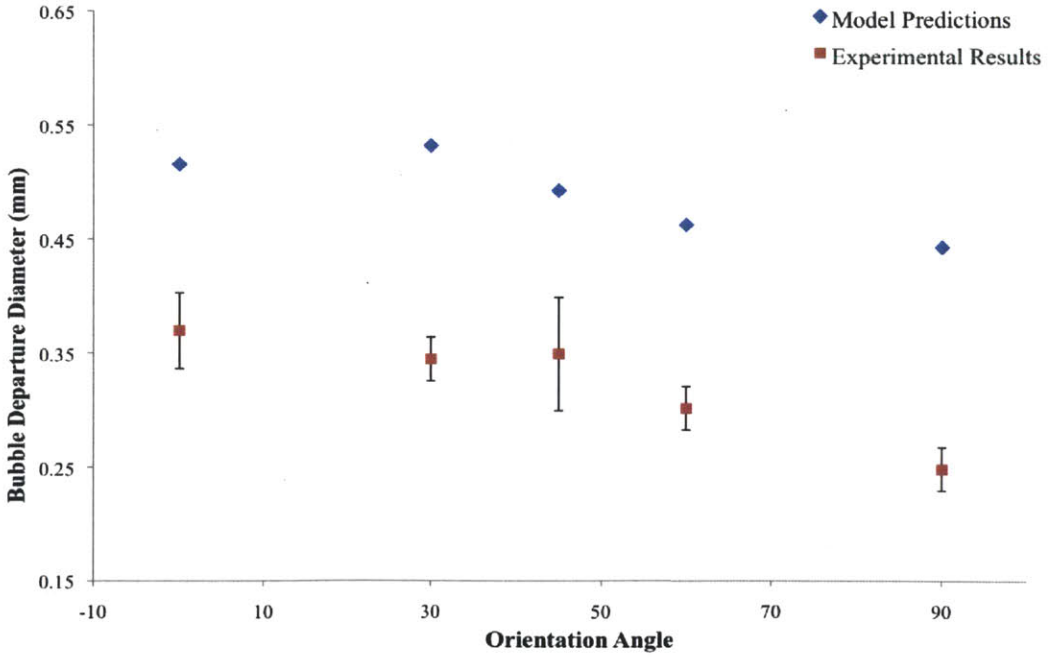

Figure 61: Comparison between Klausner's model predictions and experimental data for bubble departure diameter as a function of orientation angle; 10°C subcooling, 0.05 MW/m^2 heat flux, and 400 kg/m^{2}s mass flux, at atmospheric pressure.

Overall, as the amount of subcooling is decreased, bubble departure size tends to increase. The fact that this effect is not as dominant can be explained by an investigation of the thermal boundary layer near the wall. In most of the cases where bubble departure diameters did not seem to be affected by subcooling, the bubbles were relatively small, meaning they most likely grew and detached within the boundary layer before growing out far enough to be affected by the bulk subcooling beyond this layer.

The predictions from Klausner's model were then compared with experimental results for 10°C subcooling and a heat flux of 0.10 MW/m^2 at atmospheric pressure. Figures 62, 63, 64, and 65 show these results graphically for mass fluxes of 250, 300, 350, and 400 kg/m^{2}s, respectively.

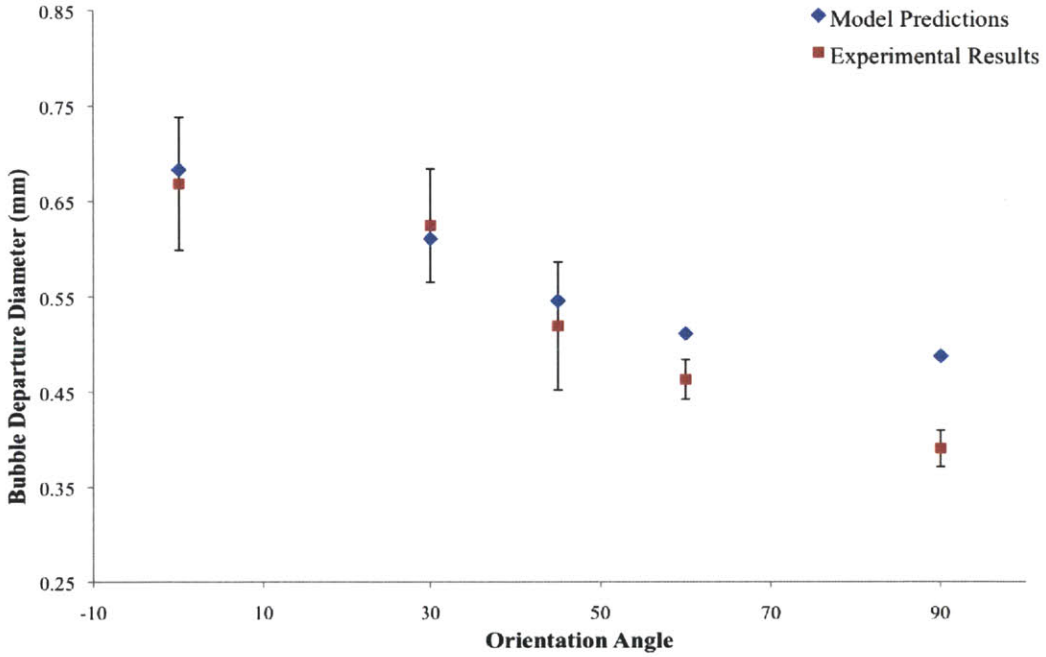

Figure 62: Comparison between Klausner's model predictions and experimental data for bubble departure diameter as a function of orientation angle; 10°C subcooling, 0.1 MW/m^2 heat flux, and 250 kg/m^{2}s mass flux, at atmospheric pressure.

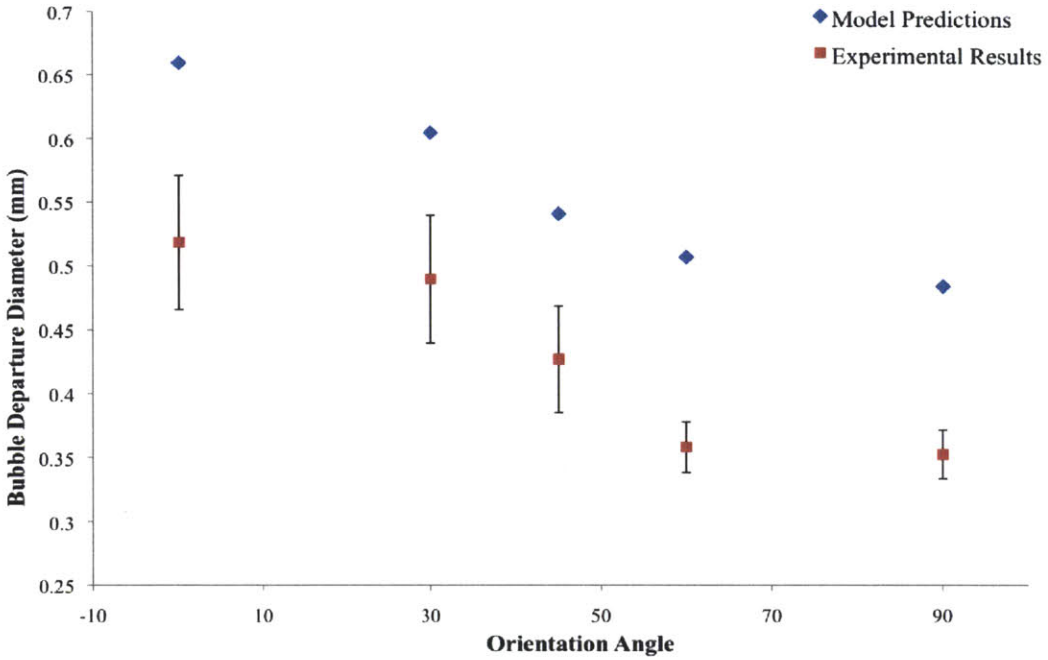

Figure 63: Comparison between Klausner's model predictions and experimental data for bubble departure diameter as a function of orientation angle; 10°C subcooling, 0.1 MW/m^2 heat flux, and 300 kg/m^{2}s mass flux, at atmospheric pressure.

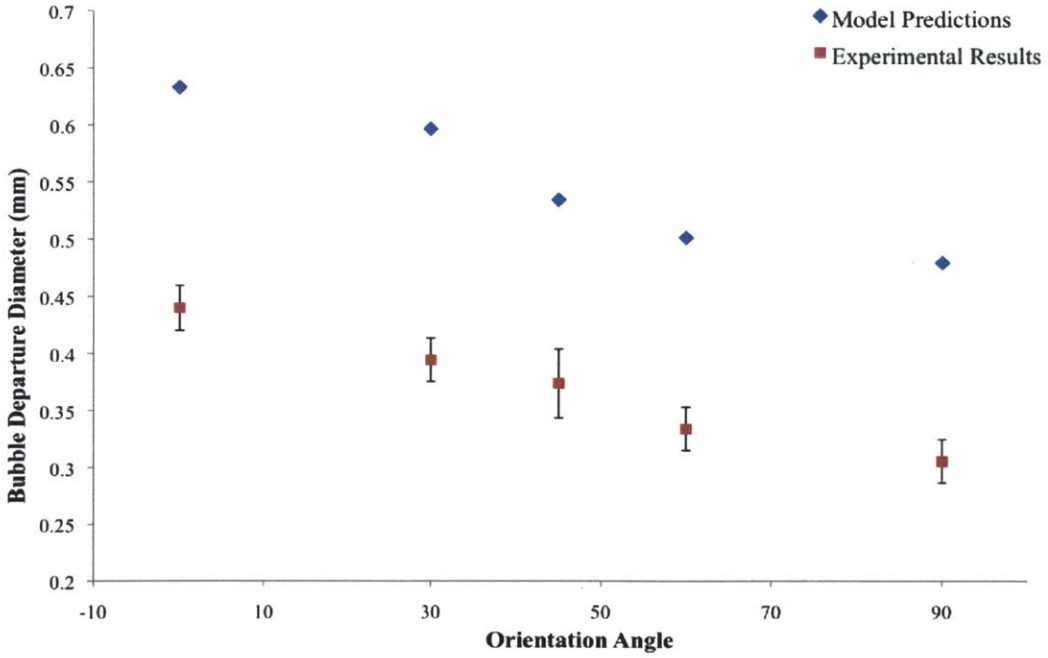

Figure 64: Comparison between Klausner's model predictions and experimental data for bubble departure diameter as a function of orientation angle; 10°C subcooling, 0.1 MW/m^2 heat flux, and 350 kg/m^{2}s mass flux, at atmospheric pressure.

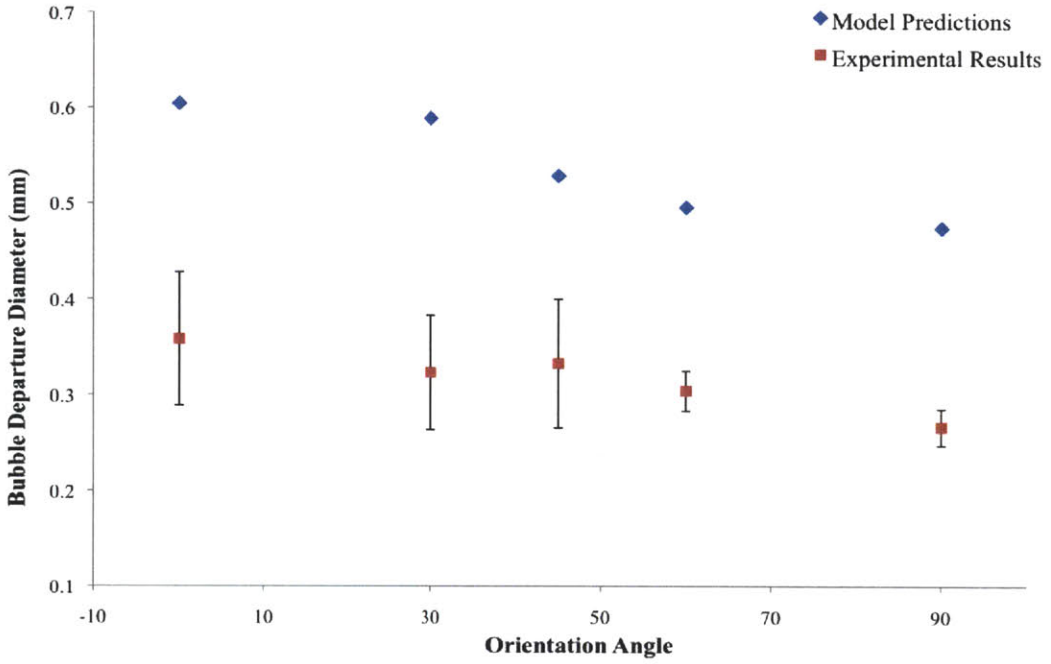

Figure 65: Comparison between Klausner's model predictions and experimental data for bubble departure diameter as a function of orientation angle; 10°C subcooling, 0.1 MW/m^2 heat flux, and 400 kg/m^{2}s mass flux, at atmospheric pressure.

Similar to the trends discussed previously for various combinations of heat flux and subcooling, Klausner's model seems to overpredict bubble departure diameter, and this margin increases for larger values of mass flux. One explanation for this is that his model did not account for condensation around a growing bubble, which could have a significant effect on bubble departure size, particularly in the context of flow boiling. Yun et al. introduced a bubble condensation term into the formulation for the unsteady drag force to account for this effect [20]. This will be discussed in more depth in the next section.

Finally, the results from the elevated pressure experiments will be compared to the predictions from Klausner's original model to determine the accuracy of this model when applied to different pressure environments. Figures 66, 67, 68, and 69 below show comparisons between the model's predictions and experimental results for a downward-facing horizontal (0°) heater with a mass flux of 400 kg/m^{2}s, with subcooling levels of 20°C and 10°C and heat fluxes of 0.05 MW/m^2 and 0.10 MW/m^2.

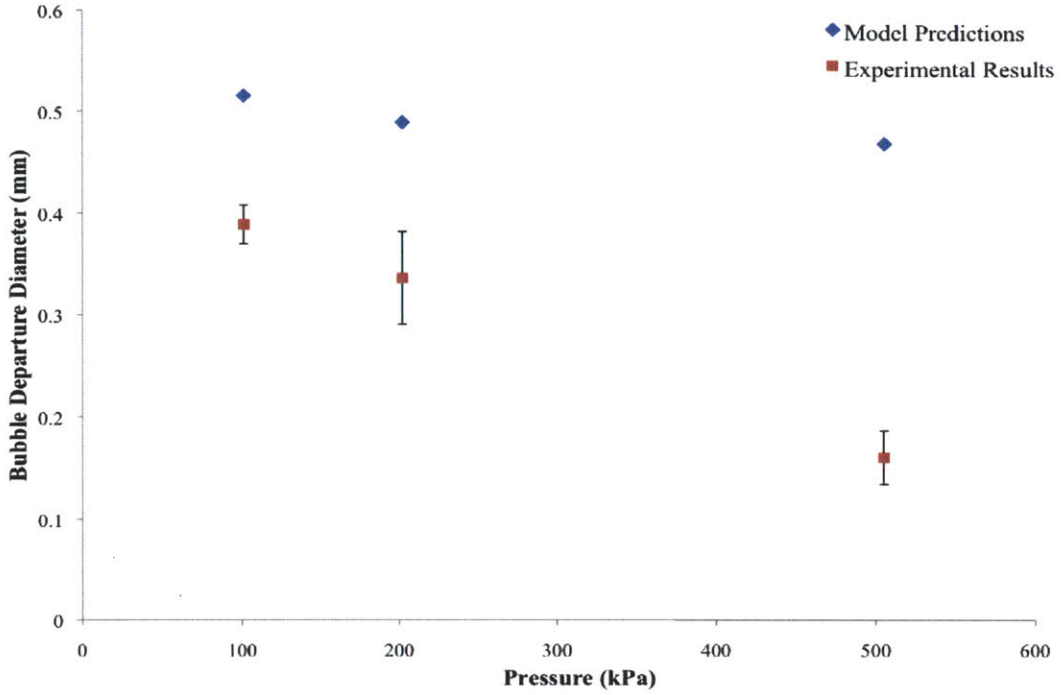

Figure 66: Comparison between Klausner's model predictions and experimental data as a function of pressure; 20°C subcooling, 0.05 MW/m^2 heat flux, and 400 kg/m^{2}s mass flux.

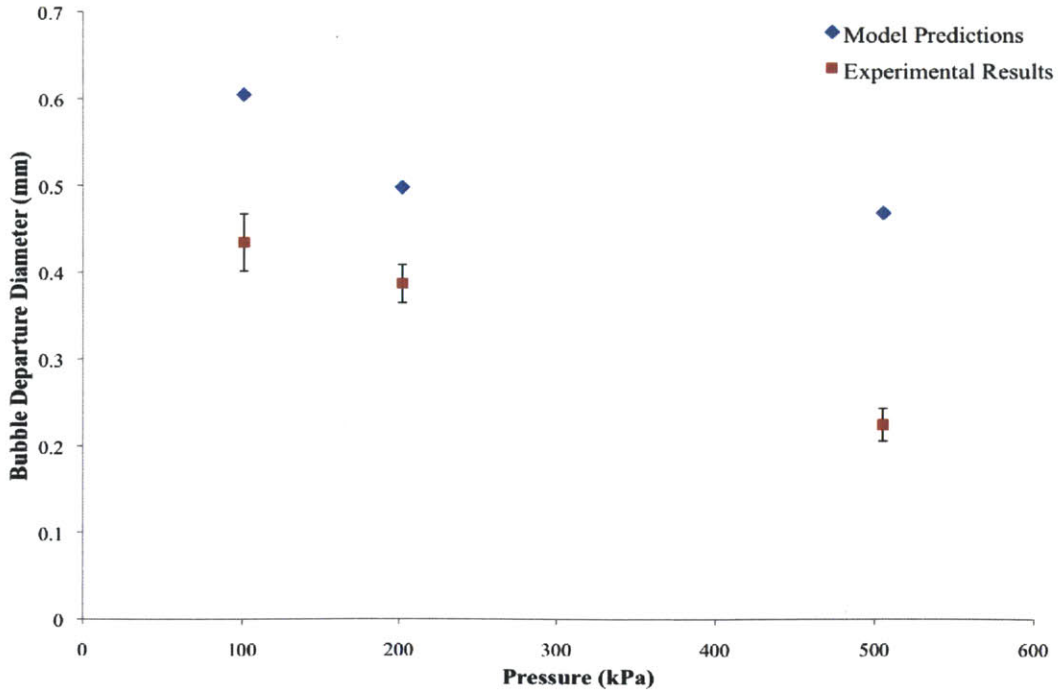

Figure 67: Comparison between Klausner's model predictions and experimental data as a function of pressure; 20°C subcooling, 0.10 MW/m^2 heat flux, and 400 kg/m^{2}s mass flux.

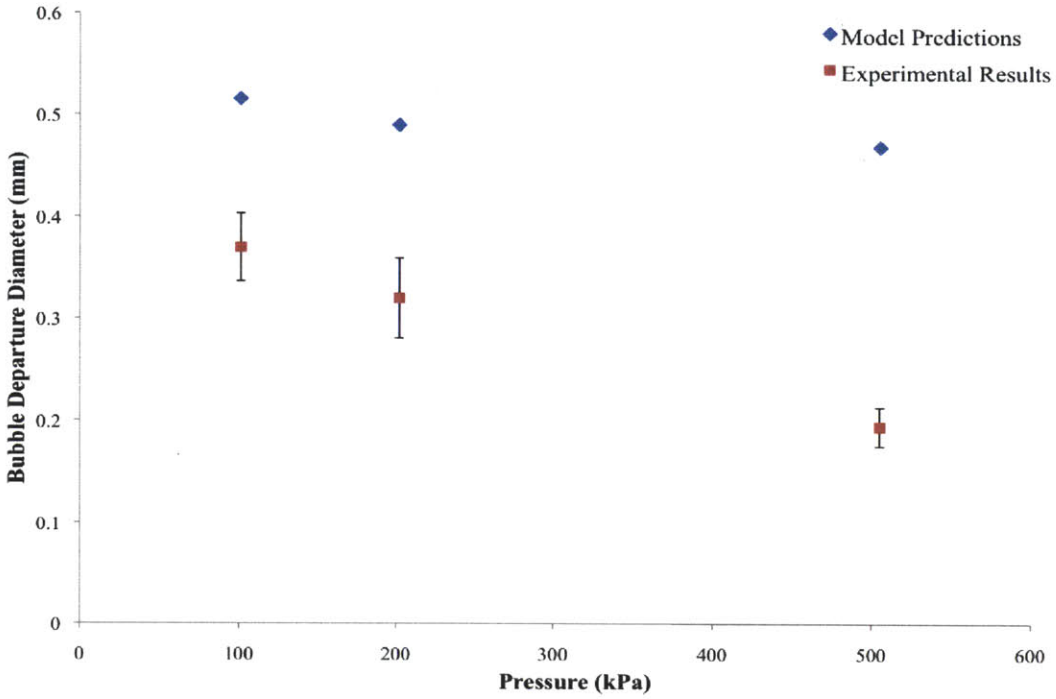

Figure 68: Comparison between Klausner's model predictions and experimental data as a function of pressure; 10°C subcooling, 0.05 MW/m^2 heat flux, and 400 kg/m^{2}s mass flux.

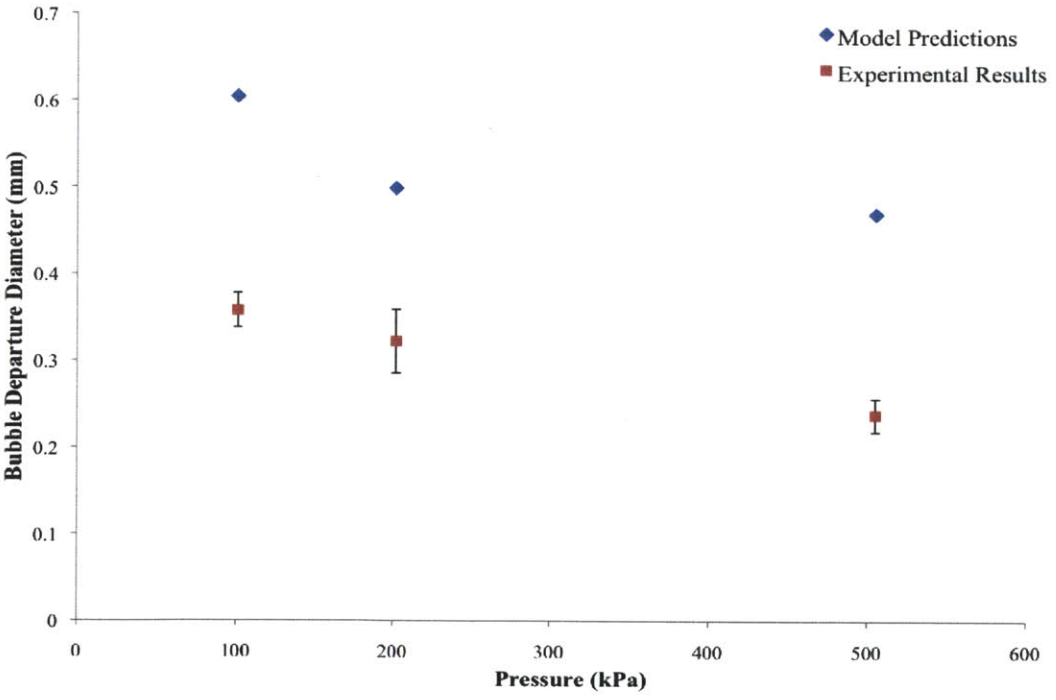

Figure 69: Comparison between Klausner's model predictions and experimental data as a function of pressure; 10°C subcooling, 0.10 MW/m^2 heat flux, and 400 kg/m^{2}s mass flux.

As was noticed for the rest of the experimental test matrix, Klausner's original bubble departure model also overpredicts bubble diameter in elevated pressure settings. This suggests that a potential improvement to the model could be to include a direct relationship with pressure, as opposed to pressure effects solely coming into effect via the bulk fluid properties (such as density, etc.).

The forces that are most sensitive to changes in pressure are the growth forces, the hydrodynamic pressure force, and the buoyancy force. The specific percent changes for each of these forces are presented in Table 20 below.

Table 20: Sensitivity analysis of pressure [kPa] on the forces in Klausner's model. The values presented for each force are the percentage increase for each change in pressure, for a mass flux of 400 kg/m^2s. Subcooling is given in °C and heat flux in MW/m^2.

ΔT_{sub}:	q":	Change in P:	F_{dux}	F_{duy}	F_b	F_h
20°	0.05	101 - 202	91.93%	91.93%	8.61%	23.72%
		202 - 505	96.29%	96.29%	14.55%	31.55%
	0.10	101 - 202	91.93%	91.93%	16.10%	23.72%
		202 - 505	96.29%	96.29%	15.07%	31.55%
10°	0.05	101 - 202	91.93%	91.93%	8.61%	19.87%
		202 - 505	96.30%	96.30%	14.55%	26.33%
	0.10	101 - 202	91.93%	91.93%	15.84%	19.87%
		202 - 505	96.30%	96.30%	15.33%	26.33%

An additional modification that should be made to Klausner's model to avoid overprediction of bubble departure diameter is to introduce a dependent relationship for the contact diameter, d_w, of the bubble as it departs. Klausner assumed a constant contact diameter of 0.09mm, which was adequate for the low pressure experimental conditions using refrigerant R113. However, the surface tension components in the force balance become significantly sensitive to changes in this parameter, and result in large effects in the overall force balance to determine the actual bubble departure

diameter sizes. Yun et al. [20] suggest the use of a constant fraction factor for the contact diameter, specifically, $d_w/d_b = 1/15$, where d_b is the bubble size. This would be used in an iterative manner to determine the sensitivity of bubble size on contact diameter.

Finally, many of the coefficients throughout the force balance equations were assigned arbitrarily by Klausner to fit the specific conditions of his experiment. Such parameters include the value of n in the quasi-steady drag force and the coefficients throughout the shear lift force, which are two of the most dominant forces in the model. The data from this experimental study can be utilized to adjust such coefficients resulting in a more rigorous model applicable to a more extensive range of flow conditions and parameters. Future work will be undertaken to develop such models. Several studies have worked to modify Klausner's original model, specifically, the most recent modification has been developed by Yun et al. [20]. The following section will apply this updated model to the experimental conditions of this study.

7.4 Comparison of Results with Latest Version of Klausner's Bubble Departure Model

As mentioned in Section 3, Klausner's model has recently been modified in order to be applicable to a wider range of flow conditions by Yun et al. [20]. Some of the primary improvements that were made by Yun included the addition of a bubble condensation term in the formulation of the unsteady drag force, and a relationship for the bubble contact diameter which depends on the actual departure size. These improvements were implemented into a modified Matlab code similar to the one for Klausner's original model in order to determine how the experimental data from this study match up with the most up-to-date version of the model. Comparisons between the experimental data, the predictions from Klausner's original model, and the predictions from Yun's modified version of Klausner's model are presented in the figures that follow.

Figures 70, 71, 72, and 73 show these comparisons for conditions of 20° subcooling, a heat flux of 0.1 MW/m^2, and mass fluxes of 250, 300, 350, and 400 kg/m^{2}s, respectively, all at atmospheric pressure (101 kPa).

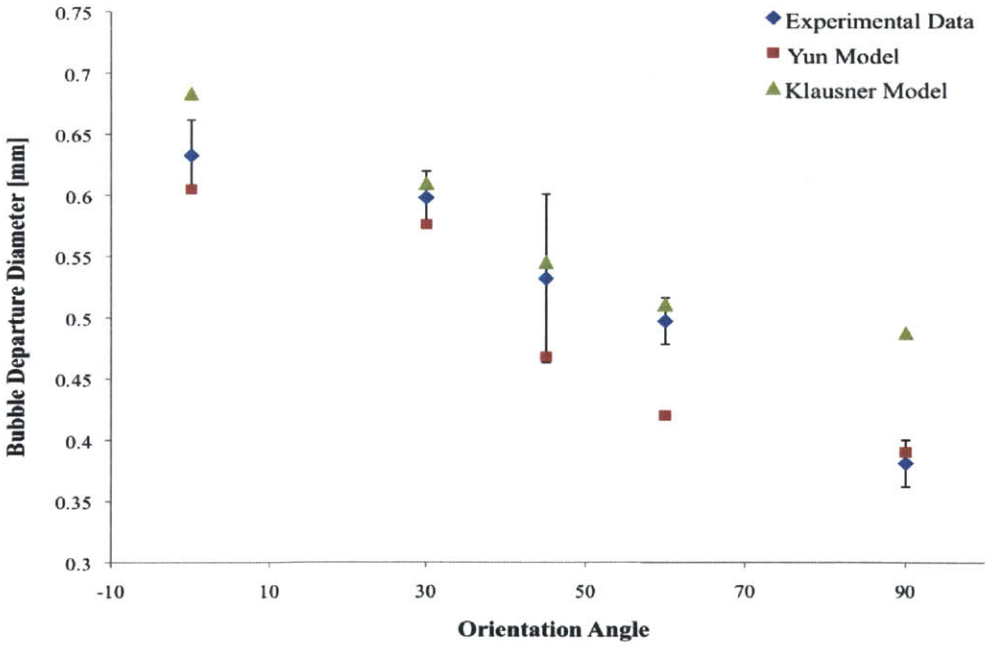

Figure 70: Comparison between Klausner's original model predictions, Yun's modified model, and experimental data for bubble departure diameter as a function of orientation angle; 20°C subcooling, 0.10 MW/m^2 heat flux, and 250 kg/m^{2}s mass flux, at atmospheric pressure.

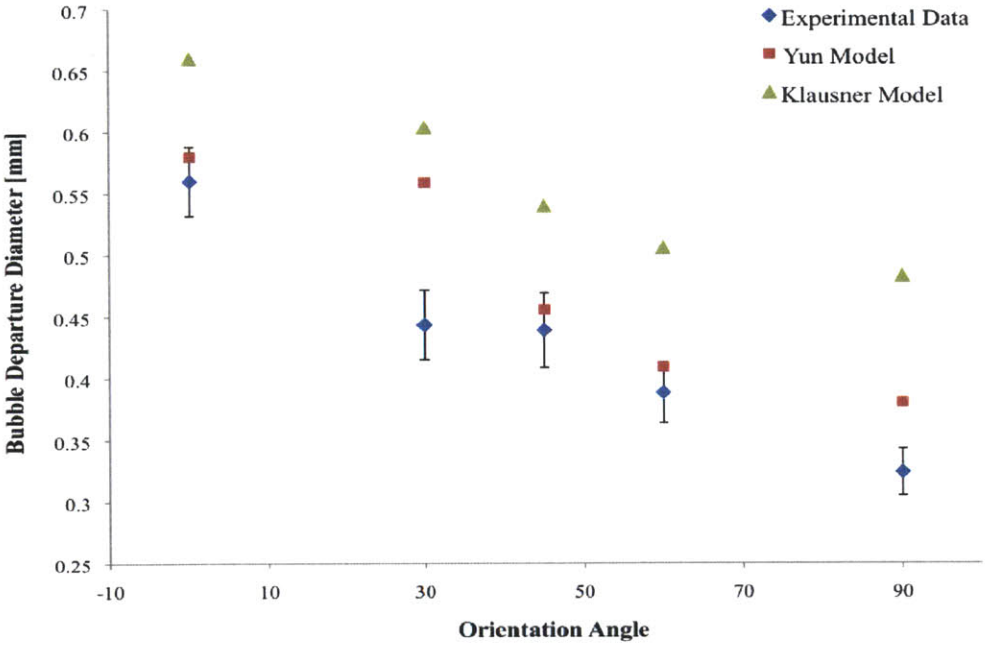

Figure 71: Comparison between Klausner's original model predictions, Yun's modified model, and experimental data for bubble departure diameter as a function of orientation angle; 20°C subcooling, 0.10 MW/m^2 heat flux, and 300 kg/m^{2}s mass flux, at atmospheric pressure.

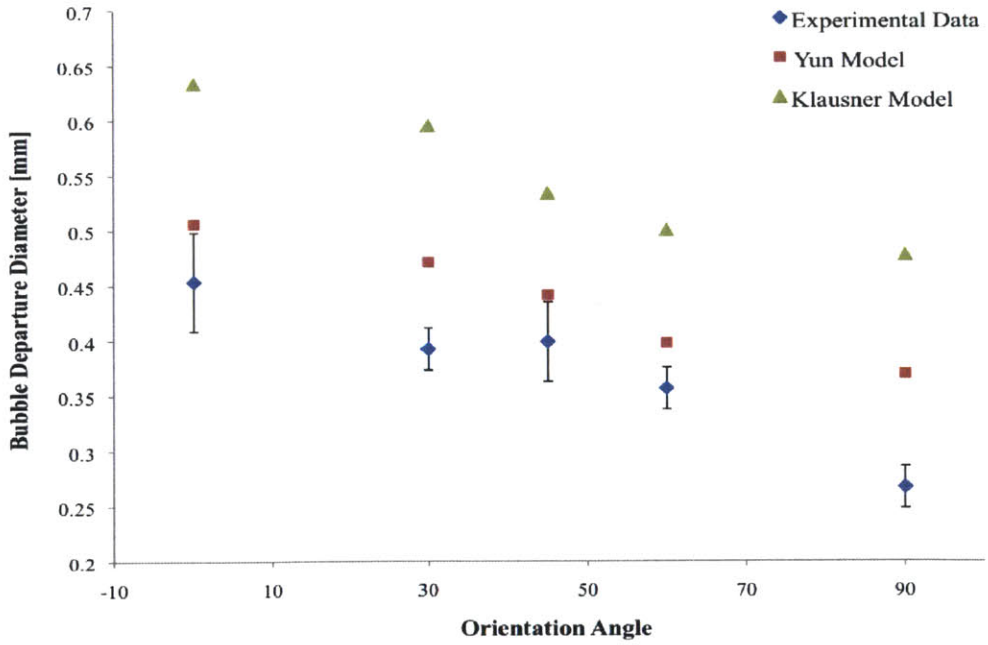

Figure 72: Comparison between Klausner's original model predictions, Yun's modified model, and experimental data for bubble departure diameter as a function of orientation angle; 20°C subcooling, 0.10 MW/m^2 heat flux, and 350 kg/m^{2}s mass flux, at atmospheric pressure.

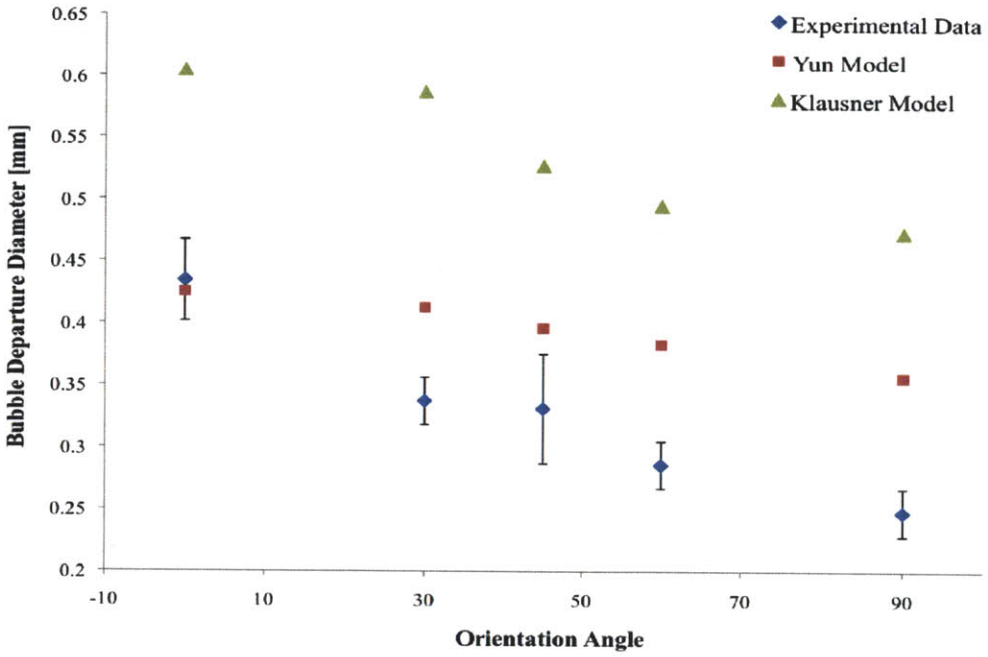

Figure 73: Comparison between Klausner's original model predictions, Yun's modified model, and experimental data for bubble departure diameter as a function of orientation angle; 20°C subcooling, 0.10 MW/m^2 heat flux, and 400 kg/m^{2}s mass flux, at atmospheric pressure.

It is clear from these figures that Yun's modifications to Klausner's original model bring the predictions closer to this study's experimental results, especially for lower values of mass flux. However, the model still overpredicts the data, as a whole. The specific errors in both models will be presented in the next section.

Figures 74, 75, 76, and 77 show similar comparisons between experimental data, Klausner's original model predictions, and Yun's modified model predictions for conditions of 20° subcooling, a decreased heat flux of 0.05 MW/m^2, and mass fluxes of 250, 300, 350, and 400 kg/m^{2}s, respectively.

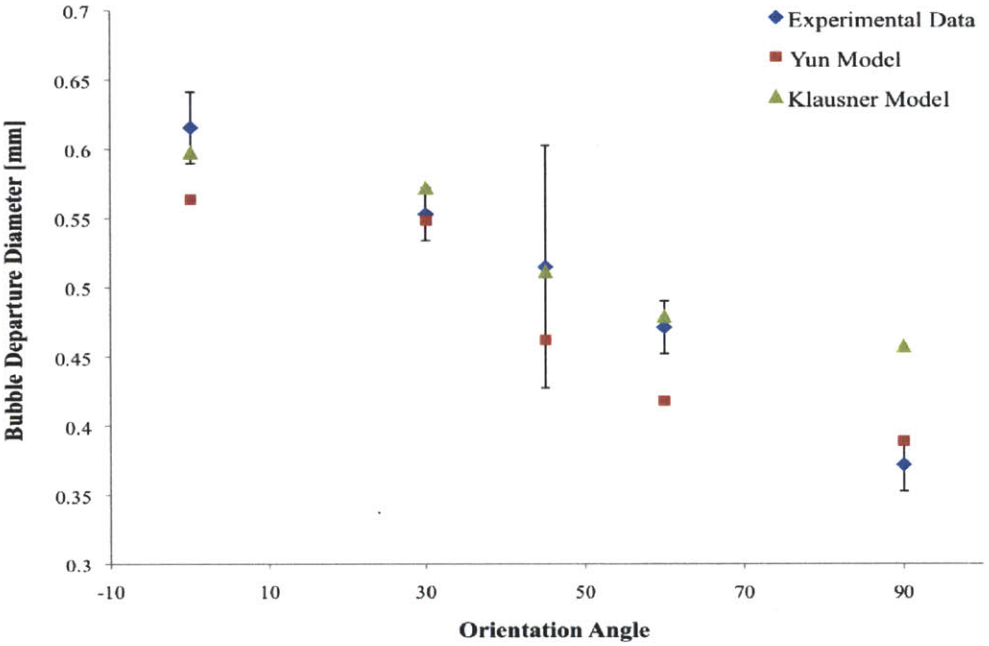

Figure 74: Comparison between Klausner's original model predictions, Yun's modified model, and experimental data for bubble departure diameter as a function of orientation angle; 20°C subcooling, 0.05 MW/m^2 heat flux, and 250 kg/m^{2}s mass flux, at atmospheric pressure.

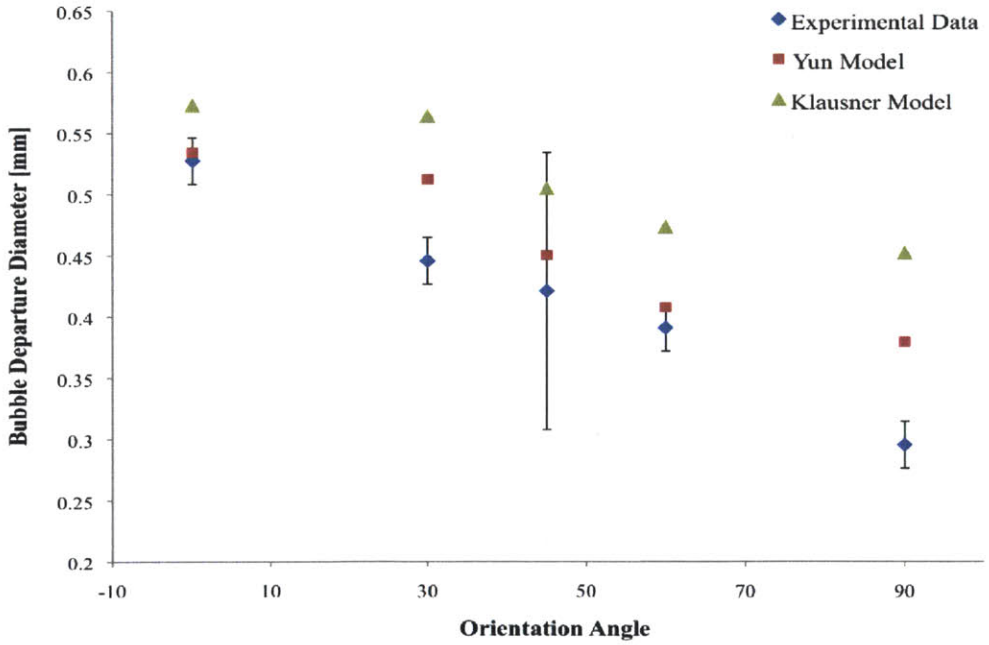

Figure 75: Comparison between Klausner's original model predictions, Yun's modified model, and experimental data for bubble departure diameter as a function of orientation angle; 20°C subcooling, 0.05 MW/m^2 heat flux, and 300 kg/m^{2}s mass flux, at atmospheric pressure.

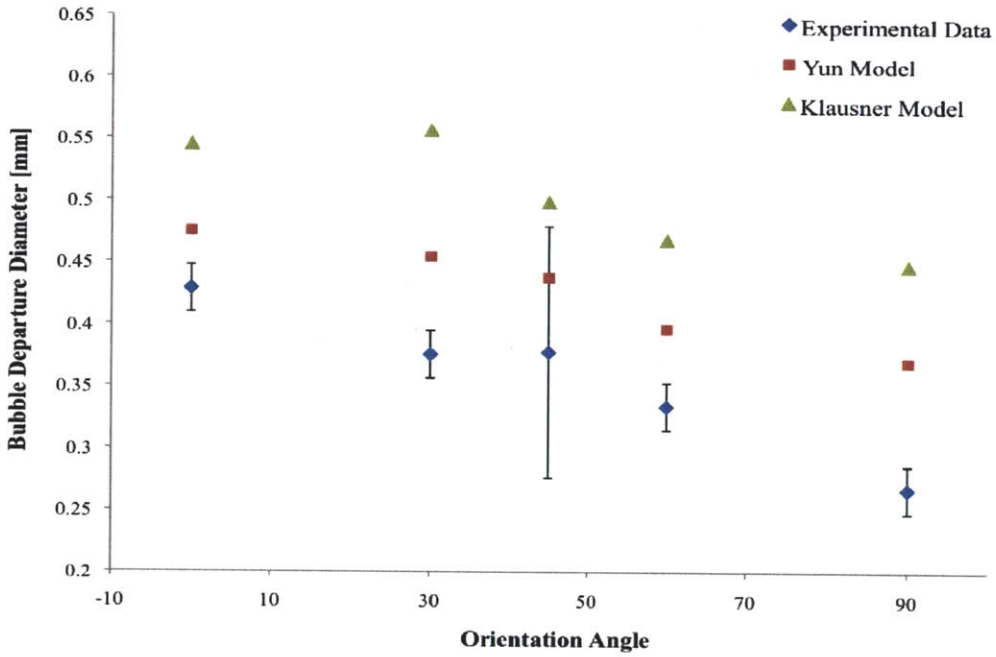

Figure 76: Comparison between Klausner's original model predictions, Yun's modified model, and experimental data for bubble departure diameter as a function of orientation angle; 20°C subcooling, 0.05 MW/m^2 heat flux, and 350 kg/m^{2}s mass flux, at atmospheric pressure.

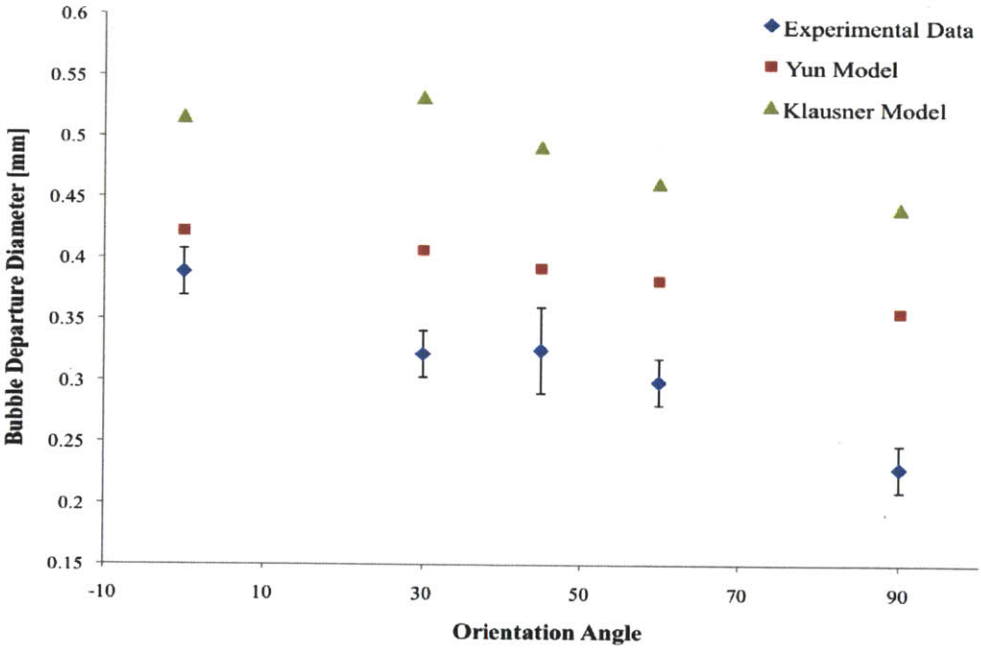

Figure 77: Comparison between Klausner's original model predictions, Yun's modified model, and experimental data for bubble departure diameter as a function of orientation angle; 20°C subcooling, 0.05 MW/m^2 heat flux, and 400 kg/m^{2}s mass flux, at atmospheric pressure.

Figures 78, 79, 80, and 81 show similar comparisons between experimental data, Klausner's original model predictions, and Yun's modified model predictions for conditions of 10° subcooling, a heat flux of 0.1 MW/m^2, and mass fluxes of 250, 300, 350, and 400 kg/m^{2}s, respectively.

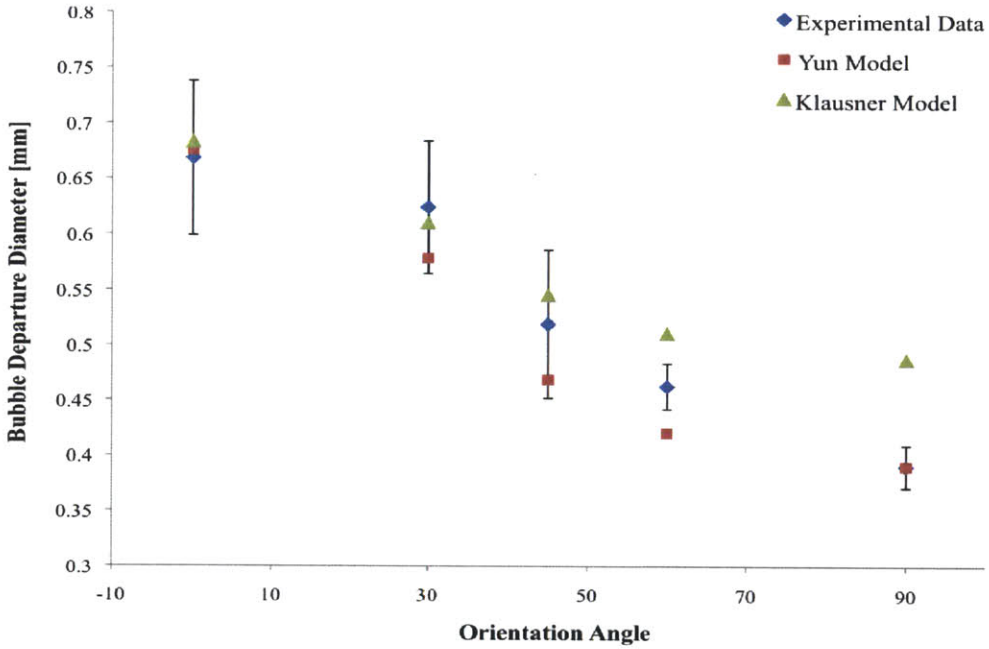

Figure 78: Comparison between Klausner's original model predictions, Yun's modified model, and experimental data for bubble departure diameter as a function of orientation angle; 10°C subcooling, 0.10 MW/m^2 heat flux, and 250 kg/m^{2}s mass flux, at atmospheric pressure.

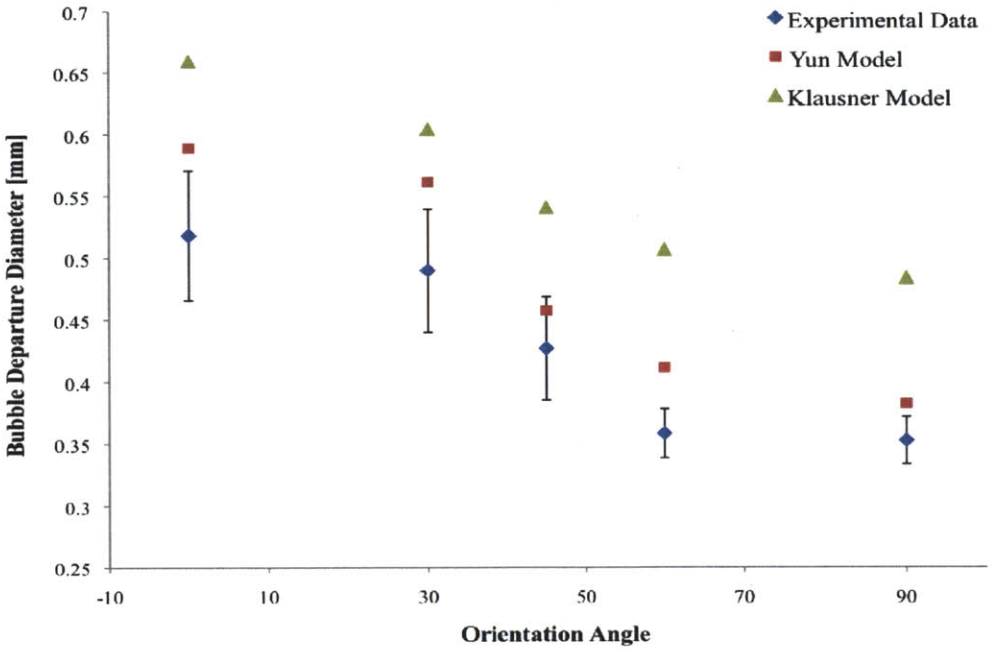

Figure 79: Comparison between Klausner's original model predictions, Yun's modified model, and experimental data for bubble departure diameter as a function of orientation angle; 10°C subcooling, 0.10 MW/m^2 heat flux, and 300 kg/m^{2}s mass flux, at atmospheric pressure.

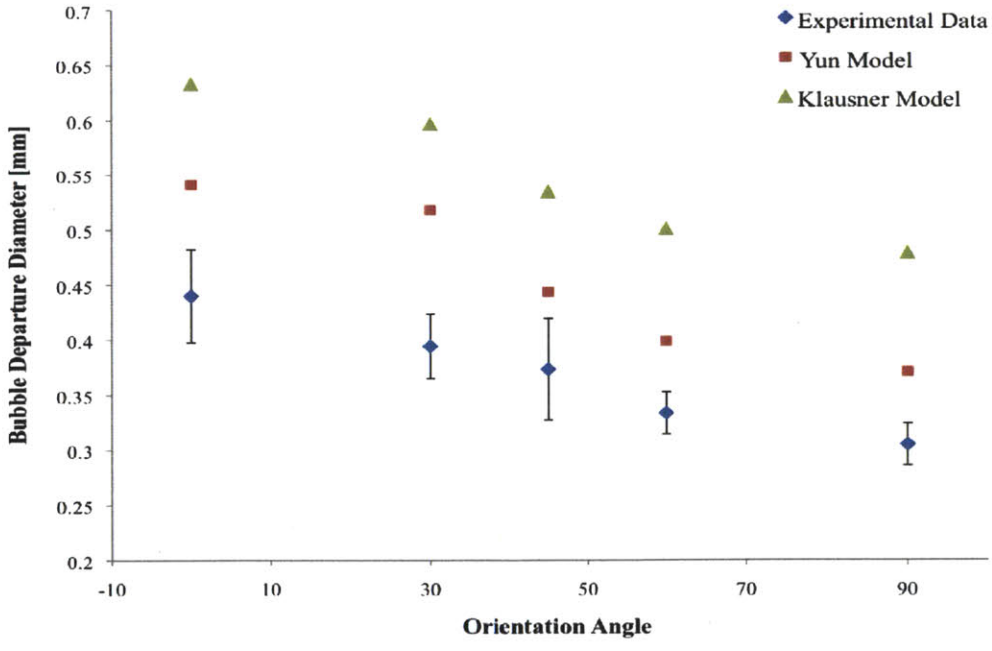

Figure 80: Comparison between Klausner's original model predictions, Yun's modified model, and experimental data for bubble departure diameter as a function of orientation angle; 10°C subcooling, 0.10 MW/m^2 heat flux, and 350 kg/m^{2}s mass flux, at atmospheric pressure.

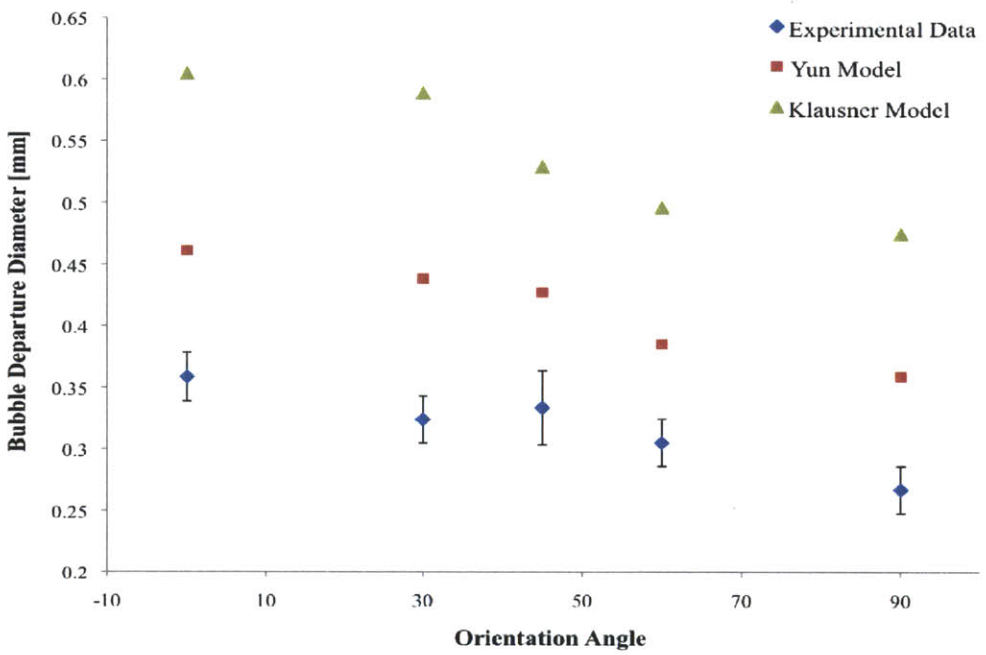

Figure 81: Comparison between Klausner's original model predictions, Yun's modified model, and experimental data for bubble departure diameter as a function of orientation angle; 10°C subcooling, 0.10 MW/m^2 heat flux, and 400 kg/m^{2}s mass flux, at atmospheric pressure.

Finally, Figures 82, 83, 84, and 85 show similar comparisons between experimental data, Klausner's original model predictions, and Yun's modified model predictions for conditions of 10° subcooling, a heat flux of 0.05 MW/m^2, and mass fluxes of 250, 300, 350, and 400 kg/m^{2}s, respectively.

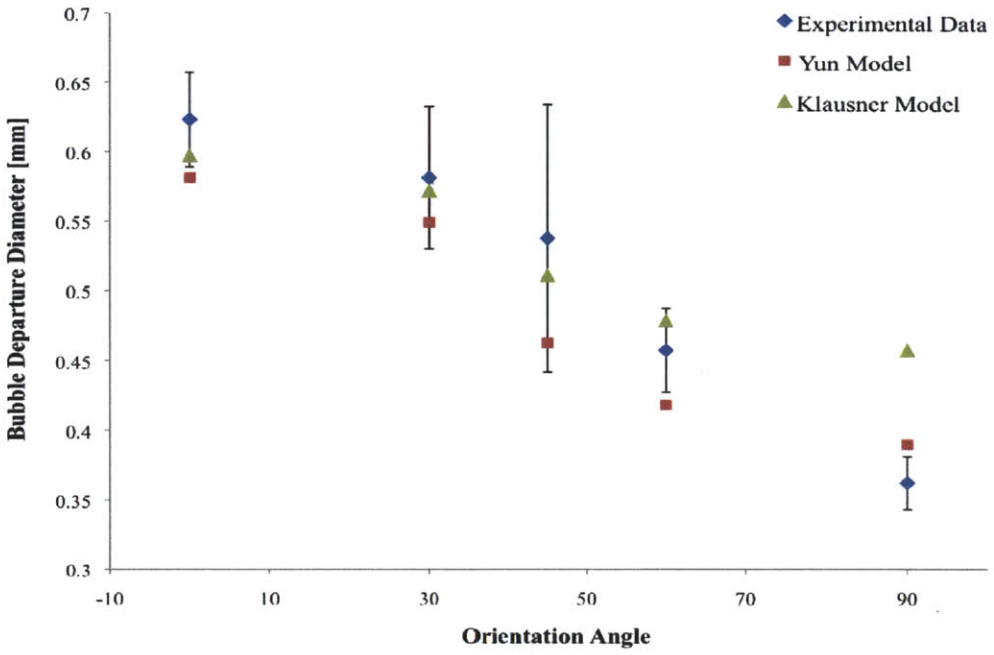

Figure 82: Comparison between Klausner's original model predictions, Yun's modified model, and experimental data for bubble departure diameter as a function of orientation angle; 10°C subcooling, 0.05 MW/m^2 heat flux, and 250 kg/m^{2}s mass flux, at atmospheric pressure.

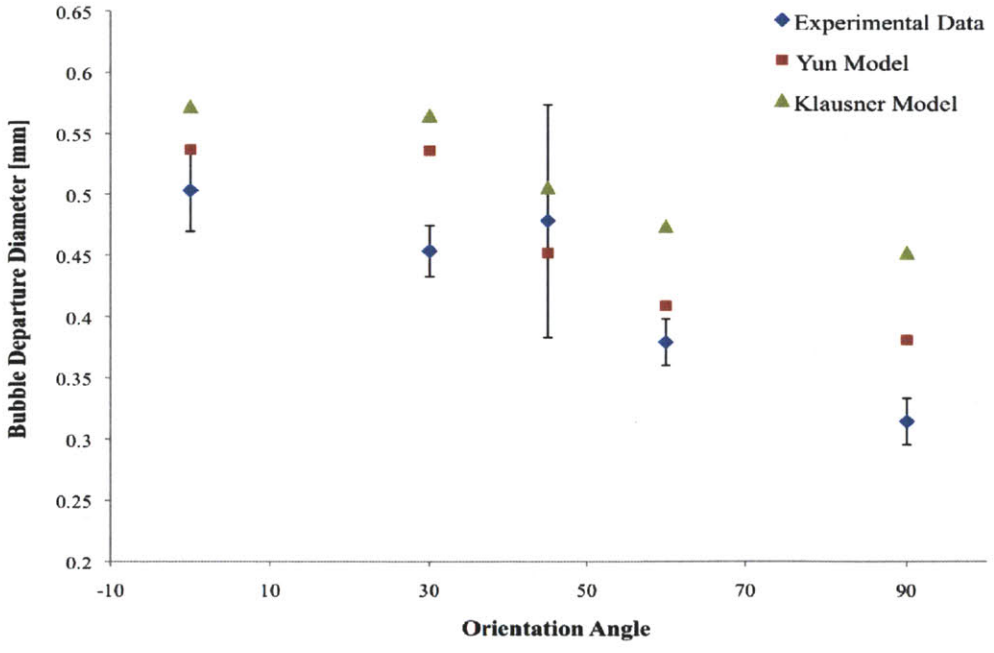

Figure 83: Comparison between Klausner's original model predictions, Yun's modified model, and experimental data for bubble departure diameter as a function of orientation angle; 10°C subcooling, 0.05 MW/m^2 heat flux, and 300 kg/m^{2}s mass flux, at atmospheric pressure.

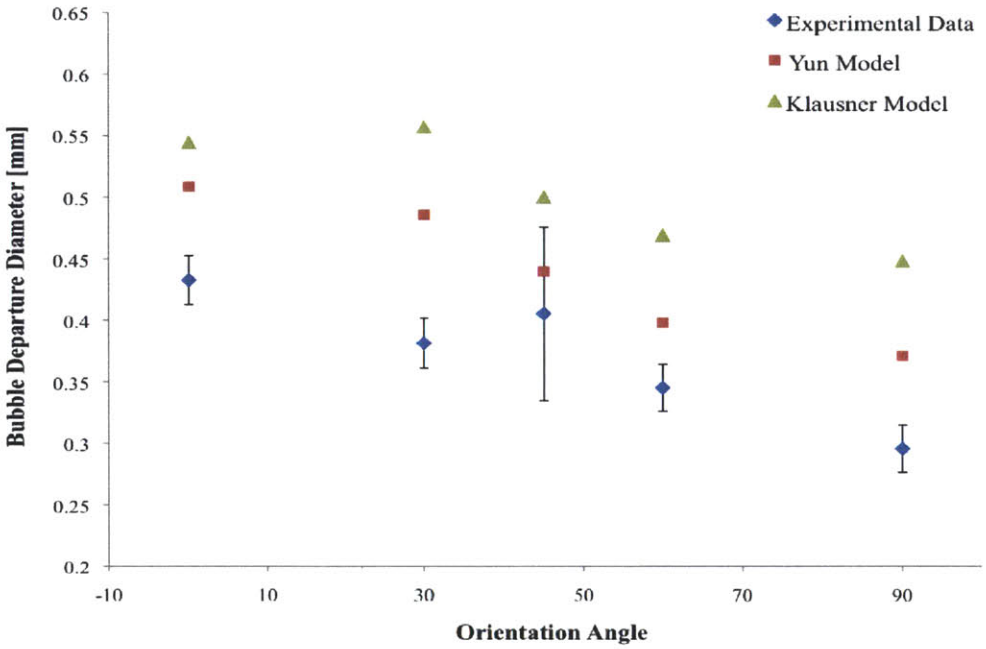

Figure 84: Comparison between Klausner's original model predictions, Yun's modified model, and experimental data for bubble departure diameter as a function of orientation angle; 10°C subcooling, 0.05 MW/m^2 heat flux, and 350 kg/m^{2}s mass flux, at atmospheric pressure.

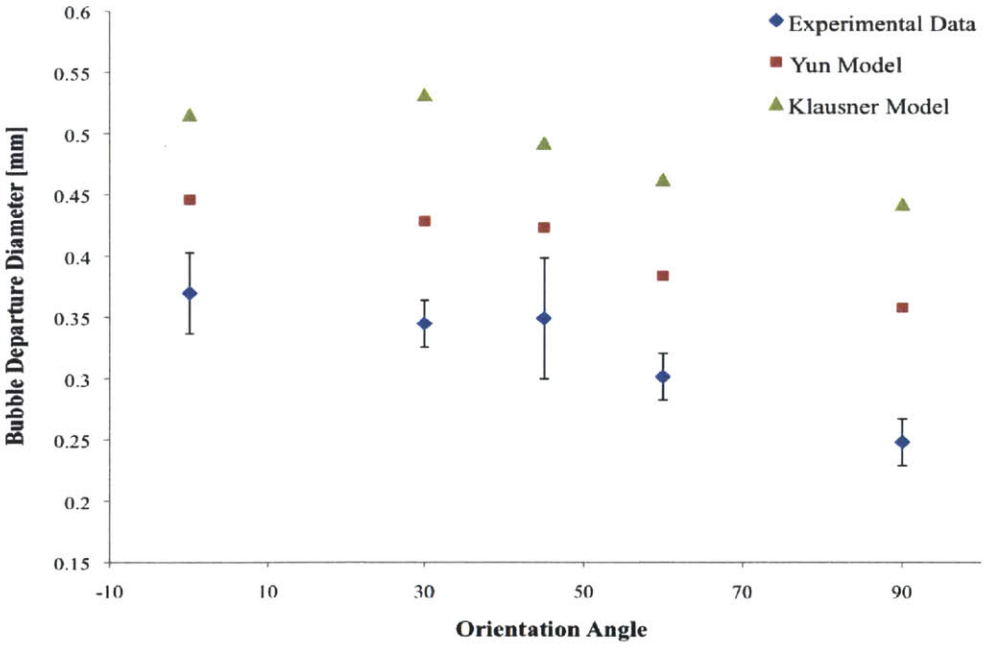

Figure 85: Comparison between Klausner's original model predictions, Yun's modified model, and experimental data for bubble departure diameter as a function of orientation angle; 10°C subcooling, 0.05 MW/m^2 heat flux, and 400 kg/m^{2}s mass flux, at atmospheric pressure.

These figures suggest that there is still room for improvement in both models in order to close the gap between model predictions and experimental results even further. Both Klausner's original model and Yun's modifications to this model correctly reproduce the experimentally observed trends, but systematically overpredict the data, in particular, for mass fluxes above 250 kg/m^2s. Specific quantification of errors will be discussed in Section 7.5.

7.5 Statistics, Errors in Models

It was shown in the previous section that both Klausner's original model and Yun's modifications to this model overpredict bubble departure diameter when compared to the experimental results in this study. The gap between the experimental data and Yun's modification is smaller, though, than the gap between the experimental data and Klausner's original model. Error distribution curves for the whole database are shown in Figure 86 below.

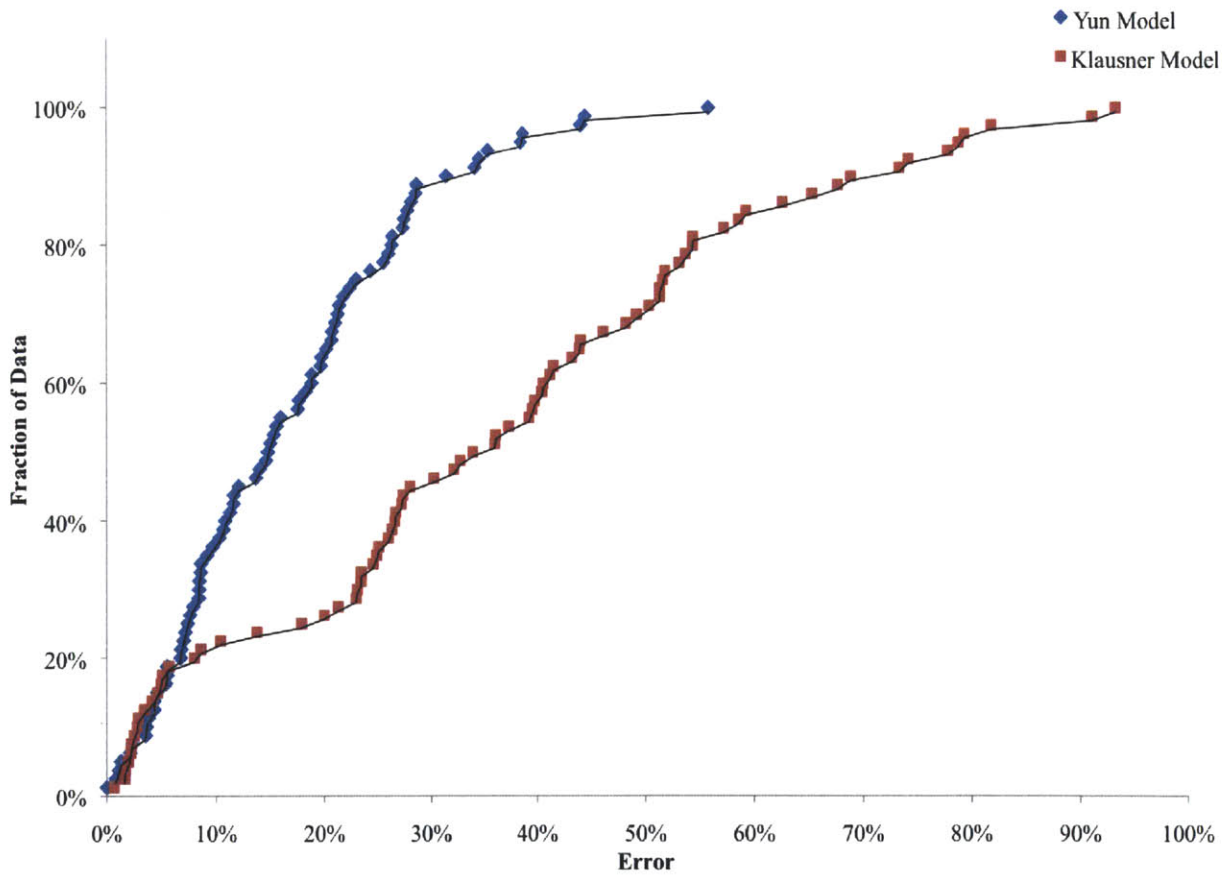

Figure 86: Cumulative error distribution curves for Klausner's original model and Yun's modifications to this model.

It is clear from this graph that Yun's model predicts the experimental data more accurately than Klausner's original model. Specifically, the average error and standard deviation calculated for Klausner's model is 35.68% ± 24.23%, while for Yun's revised model is 16.64% ± 11.60%. Note that such inaccuracies in the bubble departure diameter prediction would translate into very large

(50-100%) error in the bubble volume, if propagated in a mechanistic model of boiling heat transfer.

8 Conclusions

The effects of orientation angle, subcooling, heat flux, mass flux, and pressure on bubble growth and detachment in subcooled flow boiling were experimentally investigated and compared to predictions from Klausner's bubble departure model. The predicted and experimentally observed relationships between these parameters and bubble departure diameter are in good qualitative agreement. Specifically, bubble departure diameter increased with decreasing levels of subcooling, increasing heat flux, decreasing mass flux, and decreasing pressure. Further, it was determined that orientation angle does have a significant impact on bubble dynamics in flow boiling. Bubbles increased in size as orientation angle decreased. The largest bubbles detached off of a downward-facing horizontal (0°) surface, while the smallest bubbles detached off a vertical (90°) surface with upflow conditions.

This set of experimental data was compared to the predictions from existing bubble departure models and any significant differences were discussed. In particular, Klausner's original model was found to overestimate bubble departure diameter because of its assumptions related to contact diameter and the effect of condensation on a growing bubble in subcooled boiling. Yun's modification to this model predicted results that were closer to those from this experimental study, but there is still need for improvement. Overall, the general behaviors of bubbles that were observed from the results were consistent between the experimental findings and the trends that are captured in the models.

This work will be continued throughout the Summer of 2012 in order to improve upon the existing models to generate one which will be more appropriate for a wider range of flow conditions. In addition, future work should include an assessment of bubble departure frequency under these experimental conditions with both upward and downward-facing test sections.

References

[1] M. Kazimi, N. Todreas. *Nuclear Systems I: Thermal Hydraulics Fundamentals*, Taylor and Francis Group, LLC, 1990.

[2] J.G. Collier, J.R. Thome, *Convective boiling and condensation*, 3rd edition, Oxford University Press, 1996, p. 184.

[3] V. Prodanovic, D. Fraser, M. Salcudean. 2002. On the transition from partial to fully developed subcooled flow boiling, *International Journal of Heat and Mass Transfer*, Vol. 45, pp. 4727-4738.

[4] R. Situ, M. Ishii, T. Hibiki, J.Y. Tu, G.H. Yeoh, M. Mori. 2008. Bubble departure frequency in forced convective subcooled boiling flow, *International Journal of Heat and Mass Transfer*, Vol. 51, pp. 6268-6282.

[5] J.F. Klausner, R. Mei, D.M. Bernhard, Z. Zeng. 1993. Vapor bubble departure in forced convection boiling; *International Journal of Heat and Mass Transfer*, Vol. 36. No. 3. pp. 651-662, 1993.

[6] C. Gerardi, J. Buongiorno, L. Hu, T. McKrell, 2010. Study of bubble growth in water pool boiling through synchronized, infrared thermometry and high-speed video, *International Journal of Heat and Mass Transfer*, Vol. 53, 4185-4192.

[7] M. Ishii, T. Hibiki. 2006. *Thermo-fluid Dynamics of Two-phase Flow*, Springer.

[8] S. Lo. 2006. Progress in modeling boiling two-phase flows in boiling water reactor fuel assemblies, *Proc. of Workshop on Modeling and Measurements of Two-Phase Flows and Heat Transfer in Nuclear Fuel Assemblies*, October 10-11, KTH, Stockholm, Sweden.

[9] D. Bestion, D. Lucas, M. Boucker, H. Anglart, I. Tiselj, Y. Bartosiewicz. 2009. Some lessons learned from the use of Two-Phase CFD for Nuclear Reactor Thermalhydraulics, N13-P1139, *Proc. of NURETH-13.* Kanazawa, Japan, September 27-October 2.

[10] W.K. In, T.-H. Chun. 2009. CFD Analysis of a Nuclear Fuel Bundle Test for Void Distribution Benchmark, N13-P1259, *Proc. of NURETH-13*, Kanazawa, Japan, September 27-October 2.

[11] N. Kurul, M.Z. Podowski. 1990. Multidimensional effects in forced convection subcooled boiling, *Proc. 9th International Heat Transfer Conference*, Jerusalem, Israel. pp. 21-25.

[12] N. Kolev. 2002. How accurately can we predict nucleate boiling?, *Multiphase Flow Dynamics 2*, Springer.

[13] A. Sanna, C. Hutter, D.B.R. Kenning, T.G. Karayiannis, K. Sefiane, R.A. Nelson. 2009. Nucleate Pool Boiling Investigation on a Silicon Test Section with Micro-Fabricated Cavities, *ECI International Conference on Boiling Heat Transfer*, Florianopolis, Brazil, May 3-7.

[14] G.E. Thorncroft, J.F. Klausner, R. Mei. 1998. An experimental investigation of bubble growth and detachment in vertical upflow and downflow boiling, *International Journal of Heat and Mass Transfer*, Vol. 41, 3857-3871.

[15] E.L. Bibeau, M. Salcudean. 1994. A study of bubble ebullition in forced-convective subcooled nucleate boiling at low pressure, *International Journal of Heat and Mass Transfer*, Vol. 37, pp. 2245-2259.

[16] R. Situ, T. Hibiki, M. Ishii, M. Mori. 2005. Bubble lift-off size in forced convective subcooled boiling flow, *International Journal of Heat and Mass Transfer*, 48 (2005) 5536-5548.

[17] N. Basu, G.R. Warrier, V.K. Dhir. 2002. Onset of nucleate boiling and active nucleation site density during subcooled flow boiling, *J. Heat Transfer*, Vol. 124, pp. 717-728.

[18] D. Euh, B. Ozar, T. Hibiki, M. Ishii, C. Song, 2010. Characteristics of bubble departure frequency in a low-pressure subcooled boiling flow, *J. Nuc. Science and Tech.*, Vol. 47, No. 7, 608-617.

[19] G.H. Yeoh, J.Y. Tu. 2005. A unified model considering force balances for departing vapour bubbles and population balance in subcooled boiling flow, *Nuclear Engineering and Design* 235 (2005) 1251-1265.

[20] B.J. Yun, A. Splawski, S. Lo, C.-H. Song. 2010. Advanced Wall Boiling Model for the Subcooled Boiling Flow with CFD Code, *The Seventh Korea-Japan Symposium on Nuclear Thermal Hydraulics and Safety Chuncheon*, Korea, November 14-17.

[21] B.J. Yun, A. Splawski, S. Lo, C.-H. Song. 2012. Prediction of a subcooled boiling flow with advanced two-phase flow models, *Nuclear Engineering and Design.* In Press.

[22] W. Wu, P. Chen, B.G. Jones, T.A. Newell. 2008. A study of bubble detachment and the impact of heated surface structure in sub cooled nucleate boiling flows, *Nuclear Engineering and Design* 238(2008) 2693-2698

[23] C.A. Chen, W.R.Chang, K.W. Li, Y.M.Lie, T.F. Lin. 2009. Subcooled flow boiling heat transfer of R-407C and associated bubble characteristics in a narrow annular duct, *International Journal of Heat and Mass Transfer*, 53 (2009) 3147-4158.

[24] L.Z. Zeng, J.F. Klausner, D.M. Bernhard, R. Mei. 1993. A unified model for the prediction of bubble detachment diameters in boiling systems II. Flow boiling, *International Journal of Heat and Mass Transfer*, Vol. 36, No. 9, pp. 2271-2279, 1993.

[25] B. B. Mikic, W. M. Rohsenow, P. Griffith. 1970. On bubble growth rates, *International Journal of Heat and Mass Transfer*, Vol. 13. pp. 657-666.

[26] G.P. Celata, A. Mariani, 1999. CHF and post-CHF heat transfer, *Handbook of phase change, boiling and condensation.* Kandlikar, S.G. et al (Eds), NY: Taylor and Francis, pp. 443-493.

[27] S.G. Kandlikar. 2001. Critical heat flux in subcooled flow boiling an assessment of current understanding and future directions for research, *Multiphase Science and Technology*, Vol. 13, No. 3, pp. 207-232.

[28] N. Zuber. 1961. The dynamics of vapor bubbles in nonuniform temperature fields, *International Journal of Heat and Mass Transfer*, 2, 83-98.

[29] G. DeWitt. 2011. Investigation of downward facing critical heat flux with water-based nanofluids for in-vessel retention applications, Dissertation submitted for the degree of Doctor of Philosophy in Nuclear Science and Engineering, MIT.

[30] L.Z. Zeng, J.F. Klausner, D.M. Bernhard, R. Mei. 1993. A unified model for the prediction of bubble detachment diameters in boiling systems I. Pool boiling, *International Journal of Heat and Mass Transfer*, Vol. 36, No. 9, pp. 2261-2270.

[31] T. Hibiki, M. Ishii. 2009. Active Nucleation Site Density in Boiling Systems, *International Journal of Heat and Mass Transfer*, Vol. 46, pp. 2587-2601.

[32] R. Cole. 1960. A photographic study of pool boiling in the region of the critical heat flux, *AlChE J.* Vol. 6, 533-542.